MECHANICAL BEHAVIORS OF CRYSTALLINE-AMORPHOUS NANOLAMINATES

A Dissertation

by

ZHE FAN

Submitted to the Office of Graduate and Professional Studies of
Texas A&M University
in partial fulfillment of the requirements for the degree of

DOCTOR OF PHILOSOPHY

Chair of Committee,	Xinghang Zhang
Committee Members,	Hong Liang
	Karl “Ted” Hartwig
	Haiyan Wang
Head of Department,	Andreas A. Polycarpou

August 2017

Major Subject: Mechanical Engineering

ABSTRACT

Amorphous alloys (also referred to as metallic glasses) demonstrate superior mechanical strength, elastic limit and wear resistance. However, macroscopically the ductility of amorphous alloys is very limited, hindering their applications as structural materials. After plastic yielding, formation and rapid propagation of shear bands leads to shear localization and softening before catastrophic failure. By introduction of crystalline phases into amorphous matrix, metallic glass composites show improved ductility and plasticity. This thesis focuses on the deformation behaviors of metallic glass composites at nanoscale: crystalline/amorphous multilayered thin films. Systematic nanoindentation tests reveal the unusual size dependent strengthening mechanisms. Furthermore, tensile tests of crystalline/amorphous multilayers on polymer substrate demonstrate that ductile dimples can be achieved in metallic glass after fracture by optimizing size and interface. Nanoscratch tests show that instability of metallic glasses arising from shear band formation can be inhibited by the constraint of crystalline phases, and the friction behavior of crystalline/amorphous multilayers depends on layer thickness. In addition, via *in situ* micropillar compression technique, strategies to suppress shear instability of metallic glasses are demonstrated. This research provides valuable insight to enhance plasticity of metallic glasses through size and interface.

DEDICATION

This dissertation is dedicated to:

My grandparents

My brother

My parents

My lovely wife and soulmate, Wen

and to my angel, Airain

CONTRIBUTORS AND FUNDING SOURCES

First, I must thank my advisor, Dr. Xinghang Zhang for his support, guidance, and encouragement during the last five years. I thank my committee members, Drs. Hong Liang, Karl Hartwig, and Haiyan Wang, for challenging me to pursue great results in the pursuit of my degree. Additional thanks goes to Dr. Wang for usage of her laboratory facilities.

I greatly appreciate the staff in Department of Mechanical Engineering in Texas A&M University. They take good care of my study plan, travel reimbursement, course registration, and etc.

I want to thank my collaborators from the Wang group, Jie Jian, Liang Jiao, and Dr. Wang, Dr. Jian Wang from University of Nebraska-Lincoln, Raheleh and Dr. Bahr in Purdue University, for their directly contribution to this work. I want to thank former students in Zhang group, Drs. Nan Li, Youxing Chen, Kaiyuan Yu, Miao Song, Yue Liu, Steven Rios, and Daniel Bufford, for their support as I began my PhD study. I also want to thank my friends and coworkers, Jin Li, Sichuang Xue, Qiang Li, Jie Ding, Cuncai Fan, Ruizhe Su, Zhongxia Shang, Yifan Zhang, and Jaehun Cho, for contributions during meeting discussions, support when I meet troubles, and in general, their company through my PhD study. Finally, I want to thank my wife, Wen Zheng, for her unconditional love, encouragement, and care throughout the past 15 years.

I also acknowledge the financial support by NSF-CMMI without which this work cannot be done. My graduate study was supported by fellowship, teaching assistantship, and research assistantship from Texas A&M University. I also acknowledge the access to Microscopy Imaging Center at Texas A&M University for the use of microscope and other instruments.

TABLE OF CONTENTS

Page

ABSTRACT ii

DEDICATION iii

CONTRIBUTORS AND FUNDING SOURCES iv

TABLE OF CONTENTS vi

LIST OF FIGURES ix

LIST OF TABLES xvii

LIST OF EQUATIONS xviii

CHAPTER I INTRODUCTION 1

- I.1 Strengthening Mechanisms of Crystalline Materials 1
  - I.1.1 Hall-Petch strengthening 2
  - I.1.2 Interphase boundary strengthening 3
- I.2 Mechanical Properties of Metallic Glasses 6
  - I.2.1 Strength of metallic glasses and crystalline materials 7
  - I.2.2 Deformation mechanisms of metallic glasses 9
  - I.2.3 Deformation behaviors of metallic glasses 13
  - I.2.4 Fracture behaviors of metallic glasses 19
  - I.2.5 Shear softening of metallic glasses 24
  - I.2.6 Brief history of fabrication of metallic glasses 25
- I.3 Mechanical Properties of Thin Film Metallic Glass Composites 26
- I.4 Strain Rate Sensitivity of Crystalline Metals and Metallic Glasses 29
- I.5 Tribological Behaviors of Metallic Glasses and Metallic Glass composites 32
- I.6 Scope and Goals 35

CHAPTER II EXPERIMENTAL DETAILS 37

II.1 Magnetron Sputtering 37
II.2 Nanoindentation..38
II.3 Transmission Electron Microscopy 44
II.4 X-ray Diffraction 48

CHAPTER III UNUSUAL SIZE DEPENDENT STRENGTHENING MECHANISMS OF CU/AMORPHOUS CUNB MULTILAYERS 50

III.1 Overview 50
III.2 Introduction 51
III.3 Experimental 53
III.4 Results 55
  III.4.1 Microstructure..55
  III.4.2 Mechanical behaviors of Cu/a-CuNb multilayers..59
III.5 Discussions..61
  III.5.1 Evolution of microstructure with layer thickness 61
  III.5.2 “Weak” strengthening effect in Cu/a-CuNb multilayers 62
  III.5.3 MD simulation studies of plastic deformation in Cu/a-CuNb multilayers 69
III.6 Conclusions 73

CHAPTER IV TAILORING PLASTICITY OF METALLIC GLASSES VIA INTERFACES IN CU/AMORPHOUS CUNB LAMINATES 75

IV.1 Overview...75
IV.2 Introduction..76
IV.3 Experimental 78
IV.4 Results...79
  IV.4.1 Microstructure characterization 79
  IV.4.2 Fracture behaviors under tension tests..82
  IV.4.3 Fracture behaviors under micropillar compression tests 90
IV.5 Discussions..94
  IV.5.1 Tensile fracture behaviors of a-CuNb..94
  IV.5.2 Plasticity and fracture of multilayers under compression.............................96
  IV.5.3 Effect of interface and size on plasticity of metallic glasses 99

IV.6 Conclusions 100

CHAPTER V LAYER THICKNESS DEPENDENT STRAIN RATE SENSITIVITY OF CU/AMORPHOUS CUNB MULTILAYERS 101

V.1 Overview 101
V.2 Introduction 102
V.3 Experimental 104
V.4 Results and discussions 104
V.5 Conclusions 113

CHAPTER VI STUDY OF LAYER THICKNESS EFFECT ON FRICTION BEHAVIORS OF CU/AMORPHOUS-CUNB MULTILAYERS BY NANOSCRATCH TECHNIQUE 114

VI.1 Overview 114
VI.2 Introduction 115
VI.3 Experimental 117
VI.4 Results 118
  VI.4.1 Experimental design and microstructure characterization 118
  VI.4.2 Nanoscratch tests under constant load mode 121
  VI.4.3 Nanoscratch tests under ramping mode 123
  VI.4.4 Morphology of films after nanoscratch under high ramping load 126
VI.5 Discussions 129
  VI.5.1 Superior friction behaviors of a-CuNb films under constant load mode 129
  VI.5.2 Unstable friction behaviors of a-CuNb films under ramping load modes 130
  VI.5.3 Optimizing friction properties of Cu/a-CuNb multilayers by tailoring h 132
VI.6 Conclusions 134

CHAPTER VII SUMMARY 135

REFERENCES 137

LIST OF FIGURES

Page

Figure 1. Strengthening mechanisms that operate for crystalline metallic multilayers. (a) Dislocation pile-up against grain (interface) boundary which can also be referred to as Hall-Petch model, (b) Dislocation bowing referred as Orowan model, (c) Koehler model based on image stress, and (d) resistance to dislocation motion because of coherency stress [25]. 5

Figure 2. Comparison of elastic limit and Young's modulus among > 1500 conventional metals, alloys, metal-matrix composites with bulk metallic glasses (composites) [3]. 7

Figure 3. Shear transformation zone (STZ) model (a) and free volume model (b) [34]. 9

Figure 4. Schematic to illustrate atomic jumps due to thermal fluctuation resulting zero overall flow and due to external stress causing macroscopic flow [36]. 11

Figure 5. Deformation map of metallic glasses with respect to stress and temperature [41]. 14

Figure 6. Shear bands of amorphous PdSi alloy after bending. The bending axis is along vertical direction. Both primary and secondary shear bands can be identified [38]. 15

Figure 7. Fracture surfaces of ZrCu-based bulk metallic glass after compression (a) and tension tests (b). Compressive fracture surfaces are vein-like, but for tensile fracture surfaces, veins from radiated cores can be found [43]. 15

Figure 8. Super plastic behaviors of bulk metallic glasses under compression tests. (a) True stress-strain curves of tested samples. (b) Samples after compression tests. (d) Samples bent into different shapes. (d) Sample morphology under different levels of strains [56]. 17

Figure 9. Under micro-pillar compression, deformation mode change of PdSi by changing the diameter of pillars. From (a)-(d), the diameter of the pillars gradually decreases, and the deformation modes change accordingly [60]. 18

Figure 10. ZrTi-based metallic glass composites increase the ductility dramatically and fracture by necking. (a) Engineering stress strain curves of metallic

glass composites (DH1, 2, and 3) with monolithic BMG (Vitreloy1) (b) SEM images of BMGc after fracture show profuse shear bands around crystalline phase (c) BMGc fractures by necking while monolithic BMG fractures in a brittle fashion (d) [62]. 19

Figure 11. TEM images of Zr-based metallic glass under tension at various strain levels [68]. The necking areas in marked by the arrow. 20

Figure 12. Relationship between hardness, plastic strain and shear band density [69]. 22

Figure 13. The relationship between fracture toughness, characteristic length scale of fracture morphology, and dominant fracture mechanism [44]. 23

Figure 14. Cross-section (a) and Plan-view (b) TEM image of the Cu/a-CuZr nanolamiantes. (c) True stress strain curves comparison with other systems. (d) Gauge area after fracture [86]. 28

Figure 15. Suppression of shear band formation after rolling for Cu/a-PdSi multilayer. TEM image of Cu/a-PdSi before rolling (a) and after rolling (b) [93]....................29

Figure 16. Strain rate sensitivity of typical fcc (Ni) and bcc (Fe) metals as a function of grain size [95]. 31

Figure 17. Wear resistance improves as the increase of hardness for Cu-based MGs [113]. 34

Figure 18. Schematic illustrates the key parameters before and after unloading [115, 116]. 40

Figure 19. Typical load displacement during nanoindentation [115]. 42

Figure 20. Schematic to show the structure of electron source. 46

Figure 21. Schematic to illustrate Bragg’s law. 49

Figure 22. (a) The XRD profiles of Cu/a-CuNb multilayers (with individual layer thickness h=1-200nm) show Cu layers with (111) and (200) texture and amorphous humps from a-CuNb layers. (b) Peak deconvolution of the XRD profiles of Cu/a-CuNb 2.5 nm and 1 nm multilayers. A middle peak emerges with inter-planar spacing identical to the average of a-CuNb and Cu (111). 55

Figure 23. Cross-sectional TEM micrographs of Cu/a-CuNb multilayers with different individual layer thickness. (a) XTEM image of Cu/a-CuNb 50 nm multilayer shows alternating nanocrystalline Cu and featureless

amorphous CuNb layers with clear layer interfaces. (b) SAD pattern of the Cu/a-CuNb 50 nm multilayer shows semi-continuous Cu (111) and (200) diffraction dots and the diffuse halo ring from a-CuNb layer. (c-d) XTEM micrographs of the Cu/a-CuNb 10 nm and 100 nm multilayers with discrete layers and abrupt layer interfaces. 57

Figure 24. High resolution TEM (HRTEM) images of (a) Cu/a-CuNb 2.5 nm, (b) Cu/a-CuNb 10 nm, and (c-d) Cu/a-CuNb 50 nm multilayers. In the a-CuNb layers, extremely thin (several monolayer thick) semi-crystalline layers are observed as indicated by the arrows. 58

Figure 25. Comparison of indentation hardness of Cu/Nb [11], Cu/a-CuZr [75], and Cu/a-CuNb multilayers. A linear fit for Cu/a-CuNb was made when h=200-50nm, shown as the dashed line. The indentation hardnesses of the single layer Cu, Nb, a-CuZr, and a-CuNb films are also shown. The peak hardness of Cu/a-CuZr approaches that of the a-CuZr; whereas the peak hardness of Cu/a-CuNb is much lower than that of the a-CuNb. 59

Figure 26. Evolution of indentation hardness (H_{IT}) of Cu/a-CuNb multilayers as a function of $h^{-1/2}$, where h is the individual layer thickness. A linear fit was made when h=200-50nm shown as the dashed line. The hardness for the single layer a-CuNb and Cu films were added as references. $H_{barrier}$ was converted by the interface barrier strength which was calculated by Hall-Petch slope. H_{rom} is the average of $H_{a\text{-}CuNb}$ and H_{Cu}, while $Hrommod$ is the average of $Ha - CuNbML$ and H_{Cu}........................64

Figure 27. Load-displacement curves and images of surface morphology of indents after nanoindentation of single layer a-CuNb and Cu/a-CuNb 20 nm multilayers. (a1) and (b1) show the load-displacement curves of a-CuNb and Cu/a-CuNb 20nm multilayers respectively. Discrete pop-in events in the a-CuNb are indicated by arrows. (a2-b2) The SPM images of the indent morphology after indentation for a-CuNb (a2) and Cu/a-CuNb 20 nm multilayers (b2). (a3-b3) Comparisons of the 3D SPM images show prominent step-like pile-ups and shear bands (indicated by arrow) for the single layer a-CuNb (a3), as compared to the homogeneous deformation for the Cu/a-CuNb 20 nm multilayers. 66

Figure 28. A schematic to illustrate the deformation mechanism in the Cu/a-CuNb multilayers. (a) Single layer a-CuNb deforms by shear banding. (b) In Cu/a-CuNb multilayers (h<50), deformation is dominated by dislocation pile-ups in Cu layers and the formation of STZs in a-CuNb layers. In the beginning, dislocations in Cu layer accommodate the plasticity; then through the crystalline/amorphous interface plasticity is transferred into a-CuNb layer in the form of shear events (motion of

STZs); later, dislocations motion in the adjacent Cu is triggered by the shear events in a-CuNb through another crystalline/amorphous interface. 68

Figure 29. Atomic structures of Cu 5 nm / a-CuNb 2.5 nm multilayers, showing (a) initial structure before deformation, and (b) the deformed multilayers containing glide dislocations in Cu layers under uniaxial compression at a strain of 6.5%. Atoms are colored according their centro-symmetry parameter. Cu atoms are in blue and Nb atoms are in orange. 70

Figure 30. Atomic structures around one a-CuNb layer in Cu 5 nm/a-CuNb 2.5 nm multilayers, showing (a) undeformed structure and (b) the structure after uniaxial compressive strain of 8.0%. The black dotted lines indicate the original interfaces. The red dotted lines indicate the interfaces after 8% compressive strain. The local shears of atomic clusters across the a-CuNb layer are denoted by three ellipses. Atoms are colored according to their excess energy. 73

Figure 31. Experimental design and microstructure of the films. (a) A schematic showing the architecture of all the films. (a1) Single layer 1 μm and 2 μm a-CuNb films were deposited as references; (a2) Cu/a-CuNb multilayers with 1μm thick Cu; (a3) Cu/a-CuNb multilayers with 100 nm thick Cu layers. (b) An optical micrograph of Cu film on Kapton substrates before and after tensile test. (c) XRD profile shows the amorphous hump of single layer a-CuNb film. (d) An SEM image shows the microstructure of trilayer Cu1μm/a-CuNb2μm/Cu1μm. (e) A cross-section TEM image demonstrates the microstructure of 5 layer film: Cu100nm/(a-CuNb300nmCu100nm)×2. 81

Figure 32. Engineering stress-strain curves of Cu/a-CuNb multilayers deposited on Kapton substrates. The stress-strain curve of single layer a-CuNb (1μm) was added as a reference. 83

Figure 33. SEM micrographs comparing tensile fracture surfaces of single layer 1μm (a) and 2μm (b) a-CuNb films. (a1) An SEM image shows a representative smooth crack of 1μm thick a-CuNb. (a2) Higher magnification SEM image reveals the featureless fracture surface and shear bands. (b1) An SEM image shows the smooth fracture surface of 2μm thick a-CuNb. (b2) Higher magnification SEM image from the dashed box in (b1) reveals high-density shear bands. 84

Figure 34. Comparison of fracture surfaces between multilayers in which 1μm thick Cu layer was introduced. (a1) An SEM image shows a typical crack of bilayer Cu1μm/a-CuNb1μm film. Curved crack path was

frequently observed. (a2) The higher magnification SEM image shows that both Cu and a-CuNb layers have columnar-like fracture surface, and Cu has a smaller columnar feature size. (b1) A representative SEM image shows a crack in the trilayer Cu1μm/a-CuNb2μm/Cu1μm and the crack frequently changes its path during propagation in a direction perpendicularly to the tensile direction. (b2) Higher magnification SEM image shows the coexistence of featureless and columnar-like surface for the trilayer system. (b3) An SEM image shows a region of the same specimen in which the fracture surface of a-CuNb layer is filled with dimples and river patterns. (b4) Higher magnification SEM image shows the nanoscale dimples in a-CuNb layer along its 2 μm thickness direction. 87

Figure 35. Comparison of fracture behaviors between multilayers in which 100 nm thick Cu layer was introduced. (a1) An SEM image shows the fracture surface of Cu100nm/a-CuNb1μm/Cu100nm film. (a2) High magnification SEM image of the dashed box in (a1) shows the featureless fracture surface of a-CuNb layer. Delamination between the top Cu and a-CuNb layers happened and a gap between them was observed. (b1) An SEM image shows the fracture surface in the tested Cu100nm/(a-CuNb300nmCu100nm)×2 film, different fracture surface for the upper and lower a-CuNb layers was seen. (b2) High magnification SEM image of the dashed box in (b1) shows that for the lower a-CuNb layer, the fracture surface contains river patterns or dimples, but the upper a-CuNb layer has a relatively smooth fracture surface. The middle Cu layer is filled with voids.. 89

Figure 36. (a) True stress-strain curve of a single layer 2 μm a-CuNb film under compression obtained during *in situ* micropillar compression test in a scanning electron microscope. Four shear bands were identified during *in situ* compression test and correlated well with the pop-in events (marked as number from 1-4) on the stress-strain curve. (b) Magnified stress-strain curve shows the serrations associated with formation of shear bands. (c-h) SEM images (obtained from *in situ* tests) corresponding to point c-h in stress-strain curve were shown in (c-h) accordingly. Prominent shear bands were identified. 91

Figure 37. *In situ* micropillar compression studies on Cu1μm/a-CuNb2μm/Cu1μm trilayer. (a) Engineering stress-strain curve of the trilayer. The stress-strain curve can be divided into four stages: I - dominant deformation of the upper Cu layer; II – hardening due to increasing elastic deformation of a-CuNb layer; III – plastic deformation of the lower Cu layer; IV - shear band formations of the a-CuNb layer. (b) Magnified stress-strain curve of regime IV clearly shows the serrations caused by shear bands formations. (c-h) *In situ* SEM images corresponding to

point c-h on the stress-strain curve. Prominent plastic deformation of the upper Cu layer is observed in (d). Plastic deformation of the lower Cu layer is observed in (f). Shear bands form in a-CuNb in (h). Obvious transition of dominant deformation at various stages can be identified.........93

Figure 38. Cross-section TEM micrographs of (a) Cu/a-CuNb 50 nm and (b) Cu/a-CuNb 100 nm multilayers show featureless amorphous layers and Cu layers with columnar grains. SAD patterns (insets) show amorphous halo from a-CuNb, and (111) and (200) diffraction dots from Cu layers. (c-d) Statistics of grain size distributions show that the average grain size for Cu/a-CuNb 50 nm and 100 nm is ~ 47 nm and 94 nm, respectively...105

Figure 39. Flow chart illustrates the differences between conventional method and modified method to calculate indentation hardness. In the conventional method, *P*, *h*, and *S* are measured. In contrast, the modified method only measure *P* and *S*, but calculate *A* and *h*. Hardness vs. indentation depth of single layer a-CuNb at strain rates of 0.01, 0.05, and 0.2 s^{-1} was shown in (a), (b), and (c) respectively. The modified method (red) and conventional method (blue) demonstrate similar results at high strain rate, but the modified method show consistent and converged data at low strain rate. 107

Figure 40. (a) With the increase of strain rate, the hardness of Cu/a-CuNb 5 nm, 20 nm, and 50 nm multilayers shows little increase. (b) With the increase of strain rate, the hardness of Cu/a-CuNb 100 nm and 150 nm multilayers increases monotonically. Data of single layer a-CuNb and Cu were also added as references...108

Figure 41. (a) Strain rate sensitivity (*m*) as a function of individual layer thickness (*h*) of Cu/a-CuNb multilayers. *m* of a-CuNb, Cu, and their average value were added as dotted lines. When $h < 50$ nm, *m* of Cu/a-CuNb multilayers decreases with decreasing *h*. When $h > 100$ nm, Cu/a-CuNb multilayers has apparent strain rate sensitivity value similar to single layer Cu film. The modeled curve (dashed line) is calculated from Equ. 33. (b) The activation volume of Cu/a-CuNb multilayers as a function of *h*. Activation volume for single layer Cu films is $11b^3$, which is shown as the dashed line. (c) A schematic shows the different deformation mechanisms at different *h*. When *h* is very small (<50 nm), dislocation activities are limited and crystalline and amorphous layers can co-deform; when *h* is relatively large (>100 nm), deformation is dominated by dislocation activities, and crystalline layers accommodate more strain than amorphous layers. 109

Figure 42. Schematic showing the nanoscratch experiments under three different modes. Under constant load mode, load is not changed during nanoscratching; under low ramping load and high ramping load, load (scratch depth) is increasing during nanoscracthing. High ramping load was achieved with larger indenter tip, deeper depth, longer scratch length, and faster scratch speed. 119

Figure 43. TEM images Cu/a-CuNb 2.5 nm (a) and Cu/a-CuNb 50nm (b) multilayers. Alternating crystalline Cu and featureless a-CuNb layers can be observed. 120

Figure 44. Nanoscratch tests under constant load mode. Normal displacement-time curves were shown for a-CuNb (a1), Cu/a-CuNb 2.5 nm (a2), Cu/a-CuNb 20 nm (a3), and Cu/a-CuNb 50 nm (a4). Various loads were employed to achieve similar normal displacements for different samples. Coefficient of friction-time curves were shown for a-CuNb (b1), Cu/a-CuNb 2.5 nm (b2), Cu/a-CuNb 20 nm (b3), and Cu/a-CuNb 50 nm (b4). 122

Figure 45. Coefficient of friction as a function of normal displacement under constant load mode. A guided dashed line is added for single layer a-CuNb film. Data of Cu/a-CuNb multilayers fall in the elliptical. 123

Figure 46. Nanoscratch results of all the films under low ramping mode. Coefficient of friction vs. normal load under low ramping load (up to 2 mN) is shown for a-CuNb (a), Cu/a-CuNb 2.5 nm (b), Cu/a-CuNb 20 nm (c), and Cu/a-CuNb 50nm (d). Normal displacement (scratch depth) (e) and elastic recovery rate (f) vs. scratch length of all the film are compared. Elastic recovery rate is the ratio of recovered displacement over total displacement. 125

Figure 47. Coefficient of friction vs. normal load under high ramping load (up to 25 mN with a scratch length of 250 μm) is shown for a-CuNb (a), Cu/a-CuNb 2.5 nm (b), Cu/a-CuNb 20 nm (c), and Cu/a-CuNb 50nm (d). 126

Figure 48. SEM images of a-CuNb (a), Cu (b), Cu/a-CuNb_100 nm (c), Cu/a-CuNb 2.5 nm (d), and Cu/a-CuNb_20 nm (e) after high ramping load scratch. Obvious debris has been observed for all the films except Cu/a-CuNb 20nm. 127

Figure 49. High resolution SEM images of a-CuNb (a), Cu/a-CuNb 50 nm (b), and Cu/a-CuNb 20 nm (c) after high ramping load scratch. Grooves, debris, pile-ups, and shear bands are frequently observed in a-CuNb film (a1-a3). No shear bands were formed in Cu/a-CuNb 50 nm multilayers, but debris, grooves, smeared pile-ups, and microcracks do exist (b1-b3).

No shear bands, grooves or smeared pile-ups are found in Cu/a-CuNb 20 nm multilayer (c1-c3). 128

Figure 50. (a) Comparison of the average COF of multilayers under low (open hexagon) and high (solid filled squares) ramping load. COF of single layer Cu and a-CuNb films were also added as references. (b) Stress evolution of Cu/a-CuNb multilayers with respect to individual layer thickness under tension and indentation. 133

LIST OF TABLES

Page

Table 1. Measured modulus of single layer and multilayer thin films.............................60

Table 2. Comparison of hardness of several Cu-based multilayer films..........................63

Table 3. Summary of Hardness, modulus and coefficient of friction for single layer and multilayer films..120

LIST OF EQUATIONS

Page

Equation 1 $\sigma y = \sigma o + kd0.5$ 2

Equation 2 $F = n\tau b$ 2

Equation 3 $\sigma y \propto \ lnh/h$ 4

Equation 4 $\tau ideal = \mu b2\pi a$ 7

Equation 5 $d\varepsilon dt = 2cfkf\varepsilon 0v0\Omega \sinh(\varepsilon 0v0\ \sigma 2kT)$ 10

Equation 6 $cf = e - \gamma v * vf$ 10

Equation 7 $\Delta G = \tau\Omega$ 11

Equation 8 $\Delta Fo=\mu(T)\gamma o2\Omega o7-5v30(1-v)+2\beta 2(1+v)9(1-v)+\tau o2\gamma o\mu(T)$ 12

Equation 9 $\Delta Ge = 2\mu(1+v)(V * -V)23(1-v)V$ 24

Equation 10 $\tau\Omega = 2\mu(1+v)(V * -Vm)23(1-v)Vm$ 24

Equation 11 $m = \partial ln\sigma\partial ln\varepsilon$ 29

Equation 12 $m = 3kT\sigma v *$ 30

Equation 13 $v *= b\xi l *$ 30

Equation 14 $\mu COF = FlateralFnormal$ 32

Equation 15 $dVdx = KPH$ 32

Equation 16 $\sigma y = HV/0.3$ 39

Equation 17 $H = PmaxA$ 39

Equation 18 $h = hc + hs$ 41

Equation 19 $hs = \epsilon PmaxS$ 41

Equation 20 $hc = h - \epsilon PmaxS$ 41

Equation 21 $S = dPdh$ 42

Equation 22 $Eeff = S\pi 2\beta A$ 42

Equation 23 $1Eeff = 1 - v2E + 1 - vi2Ei$ 43

Equation 24 $A = C0hc2 + C1hc1 + C2hc1/2 + C3hc1/4 + \cdots$ 43

Equation 25 $A = C0hc2$ 43

Equation 26 $2dsin\theta = n\lambda$ 48

Equation 27 $k = (\tau * \mu b\pi(1 - v))0.5$ 60

Equation 28 $m = kT\xi b \cdot 1\chi\alpha\mu b\rho d + \beta d$ 110

Equation 29 $1m = \partial ln\varepsilon\partial ln\sigma$ (or $m = \partial ln\sigma\partial ln\varepsilon$) 110

Equation 30 $\varepsilon = 12(\varepsilon a + \varepsilon c)$ 110

Equation 31 $\varepsilon = 12(\varepsilon a + \varepsilon c)$ 111

Equation 32 $1m = \partial ln\varepsilon\partial ln\sigma = \partial\varepsilon\varepsilon\partial ln\sigma = 1\varepsilon a + \varepsilon c \cdot \partial\varepsilon a\partial ln\sigma + \partial\varepsilon c\partial ln\sigma = 1(\varepsilon a + \varepsilon c) \cdot \varepsilon ama + \varepsilon cmc$ 111

Equation 33 $1m = \Delta La\Delta La + \Delta Lc \cdot 1ma + \Delta Lc\Delta La + \Delta Lc \cdot 1mc$ 111

Equation 34 $\sigma = P\pi(R2 - h2)$ 131

CHAPTER I

INTRODUCTION

Ever since the fabrication of the first amorphous metallic alloy Au-Si on 1960, researches on amorphous metallic alloys, or the so-called metallic glasses (MGs) have become an active research subject. Amorphous alloys have some extraordinary mechanical properties such as yield strength, elastic strain, and wear resistance compared with their crystalline counterparts [1-6]. However, the drawback for MGs comes from the poor ductility because of the formation and rapid extension of shear bands. Prior studies have shown that by adding crystalline phases into amorphous matrix the ductility can be improved [7, 8]. In this section, the mechanical properties of MGs and mechanisms for enhancement of plasticity and fracture resistance of MGs are discussed.

I.1 Strengthening Mechanisms of Crystalline Materials

Before the fabrication of MGs, conventional metals and alloys were used in every aspect of daily life and industry over centuries. Strengthening mechanisms of crystals are extensively studied. Crystalline materials with superior strength show strong resistance to plastic flow, which is usually accommodated by dislocation motions. Dislocations, a critical type of defect in crystals, play a vital role in strengthening metals. Designing desirable microstructure to obstruct the motions of dislocation enhances resistance to plastic flow and in turn strengthens the materials. The strength of crystals can be expressed by yield strength and ultimate tensile strength. Yield strength is reached when plastic deformation occurs (deviation from elastic deformation) and is measured by 0.2% offset strain in stress-strain curves practically. Ultimate tensile strength is the point after which the materials start necking.

I.1.1 Hall-Petch strengthening

In the early 1950s, an empirical relationship between the yield strength and grain size was discovered by Hall and Petch (namely the Hall-Petch relationship) [9, 10],

$$\text{Equation 1} \qquad \sigma_y = \sigma_o + kd^{0.5},$$

where σ_y is the yield strength, σ_o is the friction stress or the resistance of lattice to dislocation motion, k is the strengthening coefficient (Hall-Petch slope), and d is the grain size. For different materials, k varies. In the Hall-Petch strengthening mechanism grain boundary plays an important role, often referred to as grain boundary strengthening. Grain boundaries are barriers to resist dislocation movements. When n dislocations (either existing dislocations or emitted from a dislocation source) pile up against a grain boundary, for materials to deform macroscopically, stress should be large enough for dislocations to emit from grain boundaries or trigger the dislocation motion in the neighboring grain. The force applied on the grain boundary can be calculated by Peach-Koehler equation,

$$\text{Equation 2} \qquad F = n\tau b,$$

where F is the force on the grain boundary, τ is the applied shear stress on dislocations, and b is the Burgers vector. The larger the grain size, the more dislocations forming the pile-ups. As dislocation pile-up generates back stress on the leading dislocation (near the grain boundary), thus, a smaller stress is needed for the leading dislocation to transmit across the grain boundary (or for the materials to yield).

Consequently, the finer the grain size, the larger the yield stress due to limited number of dislocations that are piling up against grain boundary. $d^{-0.5}$ quantifies the contribution from grain size reduction to strengthen crystals. Similarly, other types of boundaries such as twin boundaries can also serve as barriers to dislocation motions and thus enhance the strength of materials.

Based on the Hall-Petch strengthening mechanism, various methods, such as severe plastic deformation and thermal treatment, have been applied to refine grain size in order to strengthen materials.

I.1.2 Interphase boundary strengthening

Like grain boundaries, phase boundaries can also serve as obstacles to resist the plastic flow of materials. Due to the lattice discontinuity, dislocations cannot directly glide through phase boundaries. In particular, constructing multilayers can accurately design interphase boundary and effectively strengthen materials. Multilayer thin films cannot only serve as strong coatings, but also can be used as functional films. Modeling and experimental studies on the mechanical properties of crystalline/crystalline multilayers have explored that the hardness can be dramatically increased by decreasing the layer thickness. The strengthening has been mainly ascribed to the change in deformation mechanisms of crystalline multilayers, which is related to layer thickness and interface structures. And dislocation models were proposed to explain the mechanical behaviors of crystalline multilayer films [11-17]. The effects of different types of interfaces on deformation mechanisms of crystalline multilayers have been studied [18-23]. There are some possible strengthening mechanisms for crystalline metallic multilayers, which can be summarized in Fig. 1. Hall-Petch model works well when the individual layer thickness (h) is greater than tens of nanometers. In this strengthening mechanism, the hardness (flow stress) is proportional to $h^{-1/2}$. Here layer thickness serves as the critical dimension to curtail the number of dislocations in the pile-ups against phase boundary. When the h decreases to tens of nm, confined layer slip (CLS) model based on Orowan bowing seems to be more appropriate, and a modified CLS model has also been developed in consideration of the interface stress and dislocation interactions [11]. For the Orowan model and CLS, the relationship between yield strength and layer thickness is,

Equation 3 $\sigma_y \propto (lnh)/h.$

When h decreases further to several nanometers, Koehler stress could dominate the strength of multilayers. Koehler stress comes from the image force due to the different elastic moduli between adjacent phases [24]. When dislocations transmit from a soft phase to a phase with higher modulus, a repulsive stress arises. The larger the modulus difference, the greater the resistance. Coherency stress can also be generated if a lattice mismatch between two phases is present.

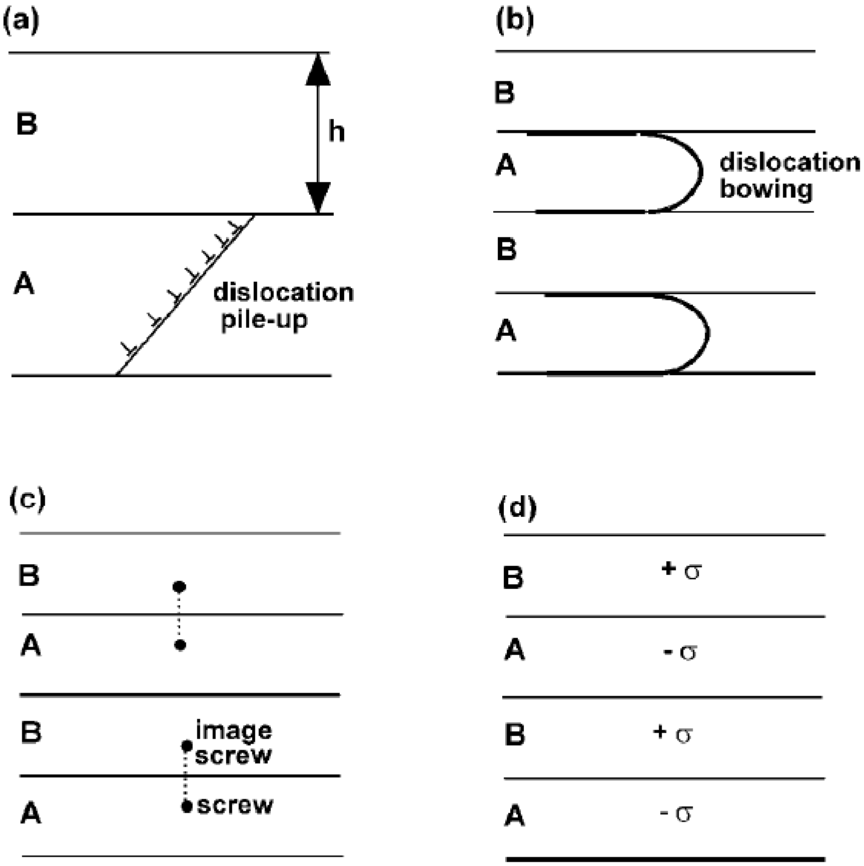

Figure 1. Strengthening mechanisms that operate for crystalline metallic multilayers. (a) Dislocation pile-up against grain (interface) boundary which can also be referred to as Hall-Petch model, (b) Dislocation bowing referred as Orowan model, (c) Koehler model based on image stress, and (d) resistance to dislocation motion because of coherency stress [25]. Reprinted from A. Misra, H. Krug. Deformation behavior of nanostructured metallic multilayers, Adv. Eng. Mater. 3 (2001) 217-222, with permission from John Wiley and Sons.

Besides the above mentioned grain boundary and interphase strengthening, other strategies such as work hardening and solid solution strengthening, can also effectively obstruct the dislocation movement in crystal, and consequently strengthen the crystalline metals.

I.2 Mechanical Properties of Metallic Glasses

The mechanical properties of MGs are extraordinary in terms of yield strength, large elastic strain and elastic energy storage which can be summarized and shown in the Fig. 2 [3]. The strength of MGs approaches theoretical strength and is much greater than their crystalline counterparts. These outstanding mechanical properties enable the wide applications of MGs, including sporting goods such as golf clubs, tennis rackets, and baseball bats; gears for micromotors with high precision; and valve springs for automobile [26, 27]. Nonetheless, the structural applications for MGs were hindered because of their poor ductility and catastrophic failure associated with rapid extension of shear bands. Due to the ultrahigh strength and limited ductility, research on MGs focuses on enhancement of plasticity and ductility instead of strengthening. In drastic contrast to crystalline materials, atoms in MGs are disordered without crystalline lattice. Therefore, dislocation based deformation mechanisms for crystals are not applicable for MGs.

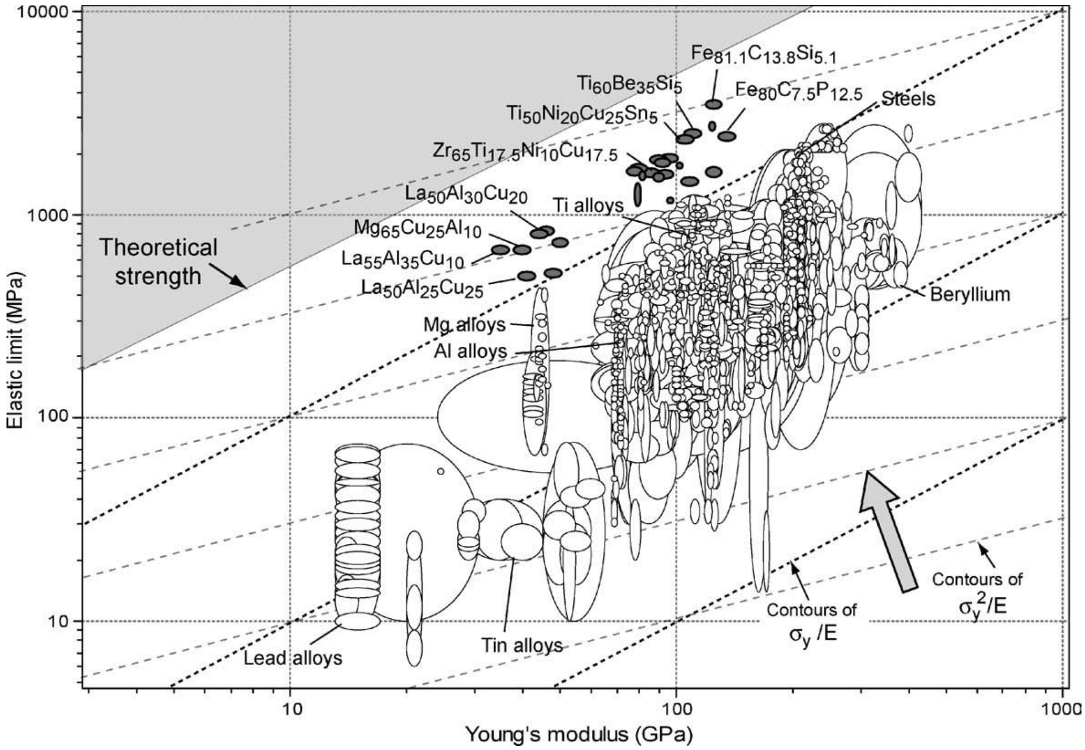

Figure 2. Comparison of elastic limit and Young’s modulus among > 1500 conventional metals, alloys, metal-matrix composites with bulk metallic glasses (composites) [3]. Reprinted from M.F. Ashby, A.L. Greer. Metallic glasses as structural materials, Scr. Mater. 54 (2006) 321-326, with permission from Elsevier.

I.2.1 Strength of metallic glasses and crystalline materials

Based on Frenkel’s theory [28], the ideal strength of a material is achieved when no defects are present. For crystalline materials, the ideal strength can be derived by considering the movement of atoms from an entire plane with respect the atoms in the plane below. The ideal strength can then be expressed as,

$$\text{Equation 4} \qquad \tau_{ideal} = \frac{\mu b}{2\pi a},$$

where τ_{ideal} is the ideal strength of crystal, a is the interplanar spacing, and b is the interatomic spacing. The above equation renders the ideal strength of crystals on the order of $\frac{1}{10}$ of the shear modulus (μ). However, due to the presence of grains, orientation difference, various kinds of defects such as dislocations, the ideal strength of crystals is hard to achieve. By reducing the sample dimension to a very small scale, the strength of defect-free crystals can approach the ideal strength, such as the strength of whiskers [29]. Metallic glasses are isotropic and free of defects, therefore, the ideal strength of them should be on the order of 0.1 μ. However, the measured shear strength of metallic glasses is 0.026 μ, usually 3-4 times smaller than the theoretical value [30, 31]. It is worth mentioning that the ideal (theoretical) strength discussed here is only related to the chemical bonding between the atoms, and does not concern the possible “flow defects” in free volume and shear transformation zones (STZ) model as described in the deformation mechanisms of metallic glasses. From nanoindentation tests using a spherical indenter, Bei et al. [32] obtained the shear stress to trigger pop-in events as large as 0.1 μ and correlate this stress to the theoretical stress. However, the ideal strength derived from nanoindentation experiments remains under debate, since Packard and Schuh deem that stress required to generate shear band under indentation technique should exceed along a certain path not the local regions [33]. From the perspective of energetics, Johnson and Samwer [30] estimate the yield strength to be ~ 0.0267 μ, where 0.0267 is a value deemed to be the macroscopic shear yield strain of metallic glasses from macroscopic measurements. However, they also point out that the maximum shear strain (of STZ) should be much larger than 0.0267. However, due to the random distribution of atoms in metallic glasses, local inhomogeneity is very likely to exist. Yielding of metallic glasses can be considered as the shearing events of certain amount of triggered STZs and cause the macroscopic plastic flow.

I.2.2 Deformation mechanisms of metallic glasses

Due to the lack of dislocations, MGs accommodate shear strain (plastic deformation) by local rearrangement of atoms. Two models, free volume model by Spaepen and shear transformation zones (STZ model) by Argon are typically applied to explain the deformation mechanism at atomistic level [34-36]. The underlying difference is that atomic movements are achieved through either discrete atomic jumps to areas with free volume in the free volume model or through inelastic shear distortion of a few to ~ 100 atoms in the STZ model, as shown in Fig. 3. Plasticity of MGs are typically accommodated by shear bands or STZs [34, 37-39].

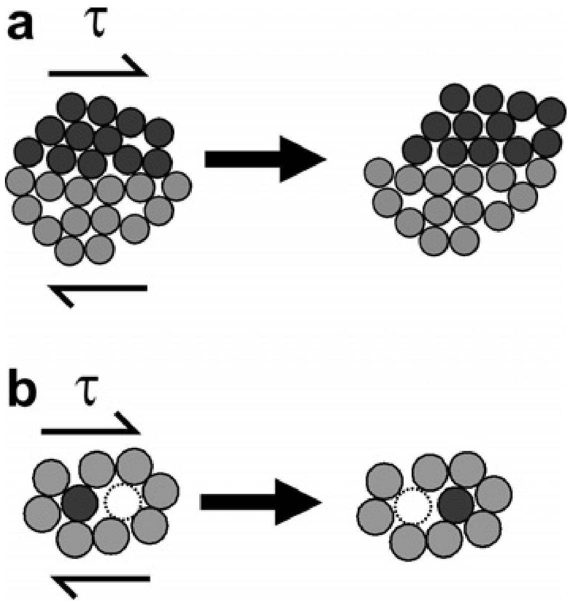

Figure 3. Shear transformation zone (STZ) model (a) and free volume model (b) [34]. Reprinted from C.A. Schuh, T.C. Hufnagel, U. Ramamurty. Mechanical behavior of amorphous alloys, Acta Mater. 55 (2007) 4067-4109, with permission from Elsevier.

Free volume model

Free volume model was first proposed by Turnbull and Cohen [40] to explain glass transition for all glasses as a whole. Spaepen applied this model to construct constitutive equation for MGs as [36, 41],

$$\text{Equation 5} \quad \frac{d\varepsilon}{dt} = 2c_f k_f \frac{\varepsilon_0 v_0}{\Omega} \sinh(\frac{\varepsilon_0 v_0\, \sigma}{2kT}),$$

where $\frac{d\varepsilon}{dt}$ is the strain rate, v_0 is the volume of these defects with free volume, ε_0 is the experienced strain, c_f is defect concentration, k_f is rate constant depending on temperature, Ω is the atomic volume, and k is the Boltzmann's constant, and T is the temperature. The "flow defects", comparable to dislocations in crystals, contain excess free volume and accommodate shear strain by redistribution of free volume through atomic jumps. c_f (flow defect concentration) can be expressed as [36, 41],

$$\text{Equation 6} \quad c_f = e^{\frac{-\gamma v^*}{v_f}},$$

where γ is a geometrical overlap factor from 0.5 to 1, v_f is the average free volume per atom, and v^* is the critical free volume value for atomic jump to happen. Based on equation (5) and (6), for MGs with more free volume, flow defect density is higher and the yield strength is lower. In order for macroscopic deformation to occur, a certain number of atomic jumps is required. For a single event of atomic jump to happen, a hole large enough to host the incoming atom should exist and certain amount of activation energy (ΔG_m) should be provided [36]. Under external stress, atomic jumps are favored in the direction of load (not equal amount of jumps between forward and backward), the resultant overall atomic jumps accommodate the macroscopic plastic flow, as shown in Fig. 4. ΔG is the work done by external stress after jump and equals to,

Equation 7 $\Delta G = \tau \Omega,$

where τ is the shear stress. Therefore, for a forward atomic jump to occur, the activation energy is reduced to $\Delta G_m - \frac{\Delta G}{2}$ and for the converse case, backward jump, the activation energy becomes $\Delta G_m + \frac{\Delta G}{2}$. With the existence of external stress, unbalanced atomic jumps result in irreversible plastic deformation.

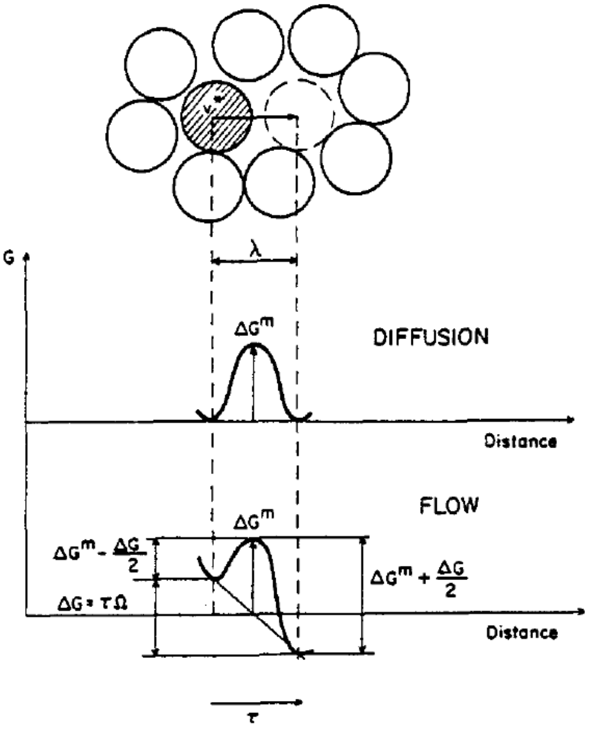

Figure 4. Schematic to illustrate atomic jumps due to thermal fluctuation resulting zero overall flow and due to external stress causing macroscopic flow [36]. Reprinted from F. Spaepen. A microscopic mechanism for steady state inhomogeneous flow in metallic glasses, Acta Metall. 25 (1977) 407-415, with permission from Elsevier.

Shear transformation zones model

STZ model from Argon [35] states that shear deformation of MGs is accommodated by spontaneous and cooperative movement of a cluster of randomly close packed atoms. As shown in Fig. 3a, the upper black atomic clusters move to the right with respect to the lower gray atoms resulting in shear displacement. STZs cannot be predetermined by observing the microstructural of MGs, instead the occurrence of STZs in certain sites in MGs depends on local atomic arrangements [34]. STZs are deemed to operate and accommodate strain in that local region which is confined by the glass matrix. These sites are usually associated with excess free volume. The free energy for activation calculated by Argon [35] is,

$$\text{Equation 8} \qquad \Delta F_o = \mu(T)\gamma_o^2\Omega_o\left[\frac{7-5v}{30(1-v)} + \frac{2\beta^2(1+v)}{9(1-v)} + \frac{\tau_o}{2\gamma_o\mu(T)}\right],$$

where ΔF_o is the activation energy, $\mu(T)$ is the shear modulus (depending on temperature), γ_o is the strain accommodated by an STZ (~0.1), Ω_o the size of the STZs (usually spanning from a few to ~100 atoms), v is the Poisson's ratio, β is the ration of dilatation to shear strain, and τ_o is the athermal shear stress for STZ operation. The free energy of STZ is on the order of 1-5 eV which is also at the higher end of activation energy in free volume model [34]. Li et al. [42] incorporate free volume as a state variable to study the structure and deformation behaviors of MGs.

Despite the differences between these two models, similarities such as two state systems, thermally activated and dilatational processes, are shared by them. In addition, two other models, cooperative shearing model and dislocation based models are also presented to investigate the deformation mechanisms of MGs [5, 34].

I.2.3 Deformation behaviors of metallic glasses

The plastic deformation modes of metallic glasses can be homogeneous plastic flow and inhomogeneous flow through shear banding [34]. For inhomogeneous flow, high stress is required and the process is strain rate insensitive. As shown in Fig. 5, homogeneous plastic flow usually takes place at lower stress and higher temperature, but at room temperature MGs usually deform by shear banding and fracture in a brittle manner with little sign of strain hardening [41]. The width of shear bands is typically 10-20 nm according to experimental and simulation studies [37]. Local softening inside the shear bands occurs for inhomogeneous flow. In contrast, crystalline materials deform plastically by dislocation movement. Strain hardening is typical for crystalline metals because of the multiplication and migration of dislocations and the formation of dislocation entanglement. Also cracks in crystalline materials can be stalled by grain boundaries compared with the lack of crack propagation barriers in MGs [34].

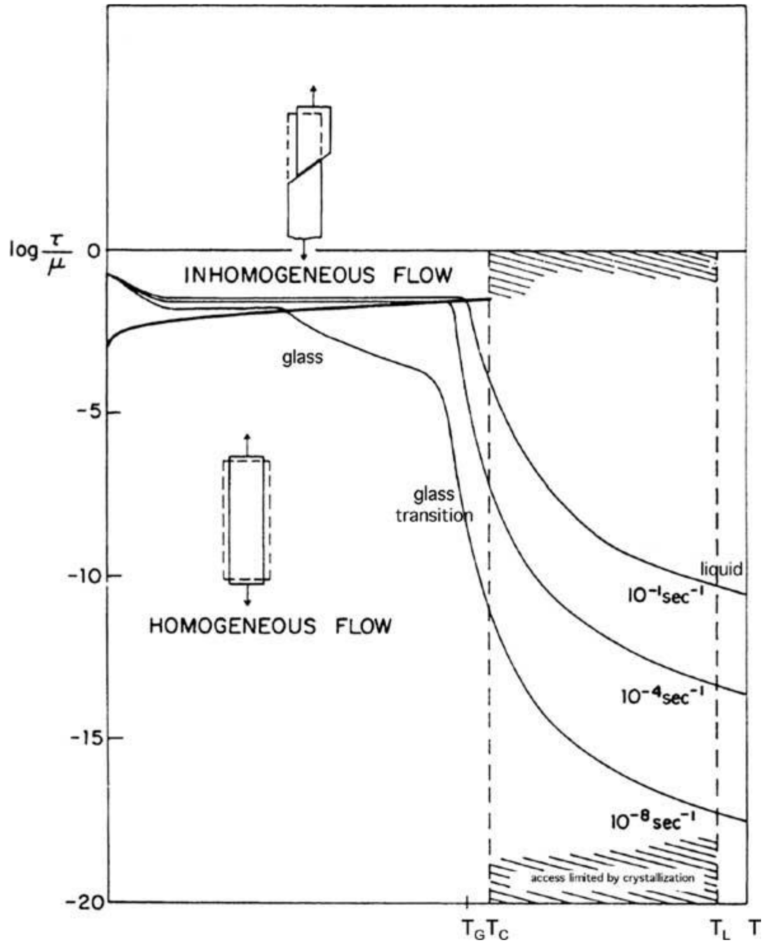

Figure 5. Deformation map of metallic glasses with respect to stress and temperature [41]. Reprinted from F. Spaepen. Homogeneous flow of metallic glasses: A free volume perspective, Scr. Mater. 54 (2006) 363-367, with permission from Elsevier.

For MGs, typical shear bands can be demonstrated in SEM images as shown in Fig. 6. Shear banding (shear localization) is a result of shear softening which is believed to be the consequence of free volume increase or structural order change in shear band. In addition, it should be mentioned that the fractural behaviors of MGs are different under compressive and tensile testing and normal stress is believed to play a role in the fracture process [43]. A comparison of fracture surface under compressive and tensile tests is shown in Figure 7.

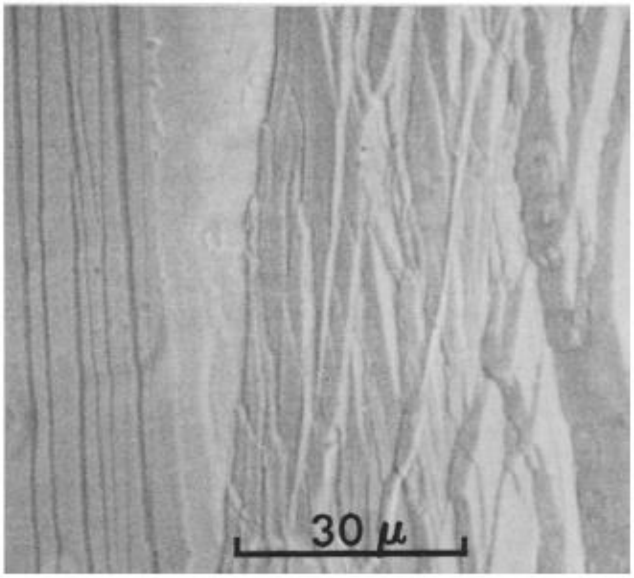

Figure 6. Shear bands of amorphous PdSi alloy after bending. The bending axis is along vertical direction. Both primary and secondary shear bands can be identified [38]. Reprinted from H. Leamy, T. Wang, H. Chen. Plastic flow and fracture of metallic glass, Metall. Trans. 3 (1972) 699-708, with permission from Springer.

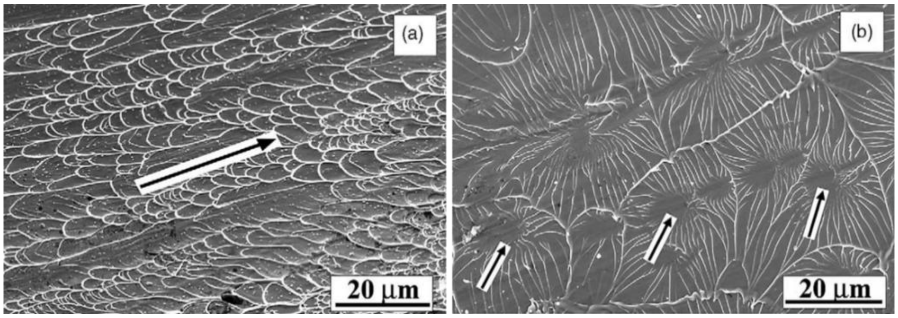

Figure 7. Fracture surfaces of ZrCu-based bulk metallic glass after compression (a) and tension tests (b). Compressive fracture surfaces are vein-like, but for tensile fracture surfaces, veins from radiated cores can be found [43]. Reprinted from Z.F. Zhang, J. Eckert, L. Schultz. Difference in compressive and tensile fracture mechanisms of Zr59Cu20Al10Ni8Ti3 bulk metallic glass, Acta Mater. 51 (2003) 1167-1179, with permissioin from Elsevier.

Since the formation and fast propagation of shear bands leads to the brittle fracture of MGs, how to generate profuse shear bands and obstruct the propagations of shear bands are crucial to enhance the ductility. Following this idea, various methods have been attempted to improve the ductility of MGs and can be classified into two categories.

Intrinsically, better ductility/toughness can be achieved by optimizing composition and structure (coordination) of MGs [44, 45]. Fabricating MGs with a larger Poisson's ratio usually can lead to good ductility since the ratio of shear modulus (μ) to the bulk modulus (B) is accounted for ductility [46, 47]. Bendable bulk metallic glasses (BMGs), $Zr_{50}Cu_{30}Al_{10}Ni_{10}$ as thick as 3 mm, have been fabricated and can be bent as much as to ~13.7 % with a thin bilayer film on top which can induce high density and more homogeneous shear bands [48]. Besides, Conner et al. [49] found out that fracture bending strains decrease with an increase in thickness of MGs. BMG foams can be more ductile and lighter compared with conventional BMGs [50]. Not only capable of tailoring the ductility, other mechanical behaviors can also be altered by changing processing conditions, composition, thermal history, and sample dimension. Previous studies show that by adjusting the processing conditions such as cooling rate and annealing, the mechanical behaviors of MGs with the same composition can be greatly changed [51-53]. It has been shown that the free volume of MGs plays an important role in the mechanical properties of MG [35, 36, 41, 54]. Besides, the structural inhomogeneity can also lead to the change of mechanical properties [55]. By selecting appropriate composition of MGs, Liu et al. [56] found out that the plasticity of MGs can also be improved through nucleating multiple fine shear bands during mechanical deformation in lieu of rapid growth of shear bands, shown in Fig. 8. It has also been shown that the addition of impurities also has effect on the mechanical properties of MGs [57]. Furthermore, it was reported that high pressure torsion can change the microstructures and thus mechanical properties of MGs [58, 59].

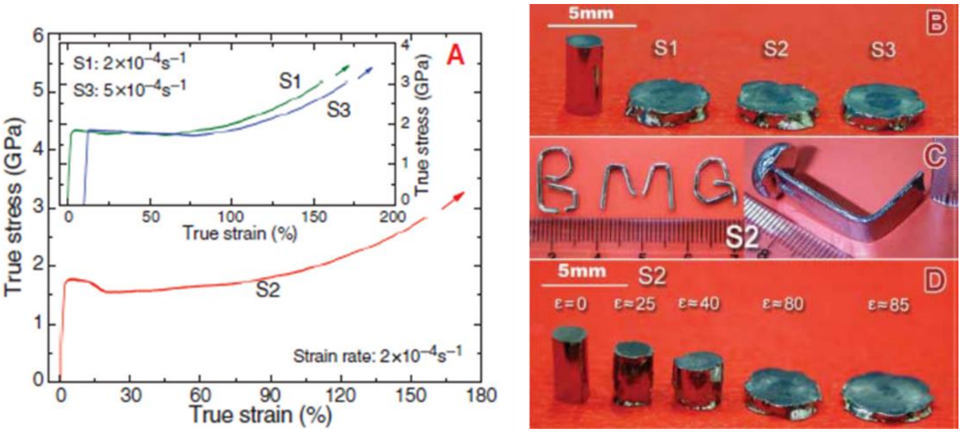

Figure 8. Super plastic behaviors of bulk metallic glasses under compression tests. (a) True stress-strain curves of tested samples. (b) Samples after compression tests. (d) Samples bent into different shapes. (d) Sample morphology under different levels of strains [56]. Reprinted from Y.H. Liu, G. Wang, R.J. Wang, M.X. Pan, W.H. Wang. Super plastic bulk metallic glasses at room temperature, Science 315 (2007) 1385-1388, with permission from The American Association for the Advancement of Science.

Besides, the deformation behaviors of MGs appear to be size dependent, which is also a subject of interest in this study. Volkert et al. [60] showed that under uniaxial compression, the deformation mode of amorphous PdSi pillars becomes homogenous with a diameter of 400 nm or less in comparison to the shear band formation in pillars with larger diameters, as shown in Fig. 9. In addition, Jang et al. [61] showed that the fracture mode for Zr-based MGs at nanoscale dimension can change from brittle fracture to ductile necking. Volkert et al. [60] found out the critical stress σ for shear band formation in amorphous alloys can be expressed as $\sigma = \sqrt{2^{3/2}\Gamma E/h}$: where Γ is the energy per unit area of shear band, E is the Young's modulus, and h is the height of the column (thickness of the film). This equation shows that the critical stress for shear band formation increases with the decrease of film thickness at a rate of $h^{-1/2}$. According to this formula, it takes much larger stress to nucleate shear bands for MGs at nanometer scale, therefore, a formation of shear band was substituted by homogeneous deformation.

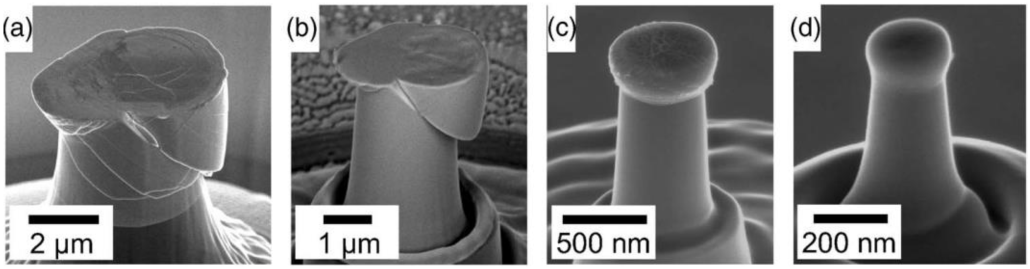

Figure 9. Under micro-pillar compression, deformation mode change of PdSi by changing the diameter of pillars. From (a)-(d), the diameter of the pillars gradually decreases, and the deformation modes change accordingly [60]. Reprinted from C. Volkert, A. Donohue, F. Spaepen. Effect of sample size on deformation in amorphous metals, J. Appl. Phys. 103 (2008) 83539-83539, with permission from AIP Publishing LLC.

Extrinsically, second phases can also enhance the ductility/toughness of MGs [7, 8]. Hofmann et al. [62] showed that ZrTi-based bulk metallic glass composites (BMGc) can have extraordinary tensile ductility (more than 10%) without the expense of their high strength because the ductile crystalline phases can initiate local shear banding and impede the shear band propagation, shown in Fig. 10. The strategy of using ductile crystalline phases to improve ductility of metallic glass matrix has also been applied to Zr-, Mg-, and Ti-based metallic glass composites (MGc) [63-67]. The added and plastically deformed "soft" phases become sites that promote more shear bands, which would then be stalled by the “hard” surrounding regions that require larger stress to be deformed [62]. The impact of crystalline phases in amorphous alloys on plasticity was also studied.

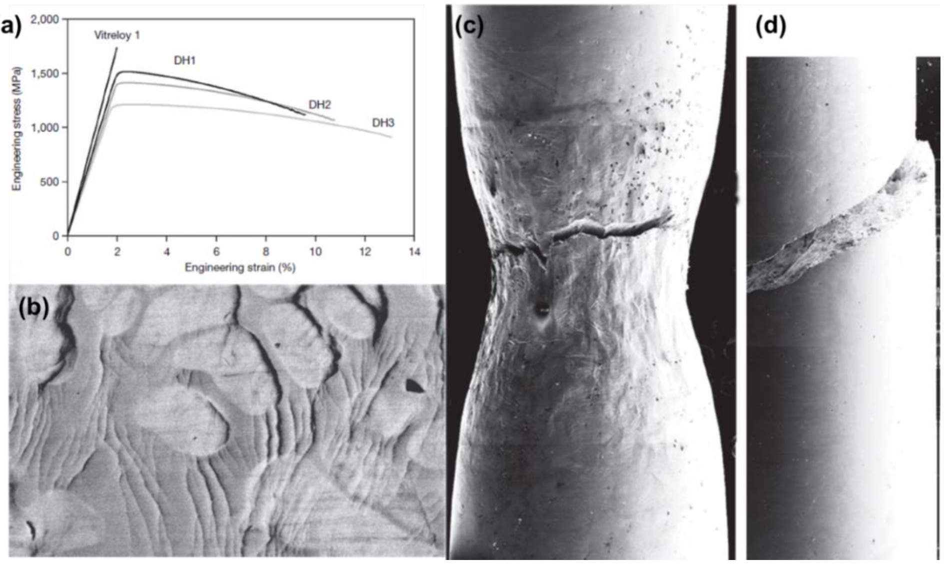

Figure 10. ZrTi-based metallic glass composites increase the ductility dramatically and fracture by necking. (a) Engineering stress strain curves of metallic glass composites (DH1, 2, and 3) with monolithic BMG (Vitreloy1) (b) SEM images of BMGc after fracture show profuse shear bands around crystalline phase (c) BMGc fractures by necking while monolithic BMG fractures in a brittle fashion (d) [62]. Reprinted from D.C. Hofmann, J.-Y. Suh, A. Wiest, G. Duan, M.-L. Lind, M.D. Demetriou, W.L. Johnson. Designing metallic glass matrix composites with high toughness and tensile ductility, Nature 451 (2008) 1085-1089, with permission from Nature Publishing Group.

I.2.4 Fracture behaviors of metallic glasses

Materials can either fracture in a brittle or ductile manner. Brittle fracture usually occurs in ceramics, and oxide glasses. Before fracture, almost no plastic deformation is accommodated. Ductile fracture usually happens in crystalline metals and alloys, such as steels. Prior to ductile fracture, substantial plastic deformation occurs, and during ductile fracture, a considerable amount of energy is dissipated. Deformation of metallic glasses is accommodated by the limited number of shear bands. Before and during fracture, a certain amount of energy is dissipated. But the crack propagation is usually catastrophic without too much resistance. The fracture behaviors of metallic glasses depend on various loading conditions, such as loading direction, rate, temperature and pressure. The overall fracture behaviors could result from the combination of three crack modes: opening, shear, or out-of-plane shear. The fracture modes of metallic glasses can be divided into four categories: shear fracture, cleavage, fragmentation, and ductile necking mode [44].

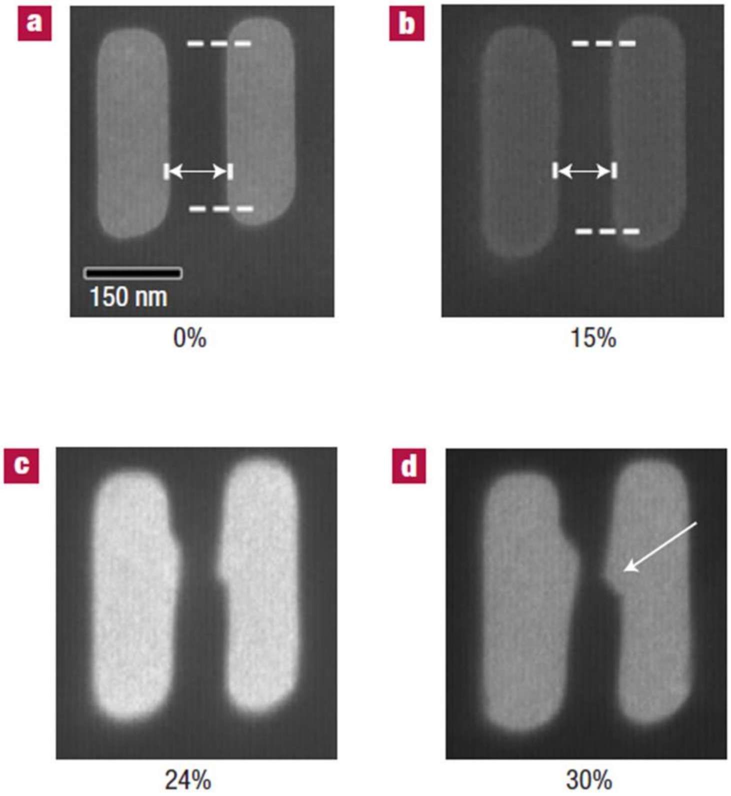

Figure 11. TEM images of Zr-based metallic glass under tension at various strain levels [68]. The necking areas in marked by the arrow. Reprinted from H. Guo, P. Yan, Y. Wang, J. Tan, Z. Zhang, M. Sui, E. Ma. Tensile ductility and necking of metallic glass, Nat. Mater. 6 (2007) 735-739, with permission from Nature Publishing Group.

In shear fracture mode, fracture happens in a shear plane inclined to loading direction, usually applicable for relatively ductile metallic glasses, such as Zr-, Cu- and Ti-based systems. The angle between the shear plane and loading direction is not necessarily 45°, the plane with maximum resolved shear stress. Shear crack mode (Mode II) applies to this mode. Besides, the angle also depends on whether the sample is under tension and under compression. This indicates the effect of normal stress or pressure on metallic glasses, different from crystalline materials. One major shear band normally propagates on the shear plane and leaves a fracture surface with vein patterns. In cleavage mode, fracture occurs in the plane perpendicular to loading direction, dominated by opening mode (mode I) and applicable for brittle metallic glasses, such Mg- and Fe-based systems. Different to the featureless fracture surface of crystalline materials under cleavage mode due to atomic bond breaking, fracture surface of metallic glasses contains certain roughness. In fragmentation mode, metallic glasses will fracture into small particles or pieces. Compared with cleavage mode, the fracture happens not in one plane but different sites for fragmentation mode. In ductile fracture mode, metallic glasses experience stable deformation and form necking before fracture. However, necking behaviors for metallic glasses only occur when the dimension of sample is reduced under several hundred nanometers or smaller. As shown in Fig. 11, Guo et al. [68] showed that under tension, Zr-based metallic glasses with a thickness of ~100 nm experience substantial deformation and forms necking before final rupture, while remains fully amorphous. Jang and Greer [61] also showed ductile necking fracture for Zr-based metallic glass nanopillar. These results suggest that metallic glasses are not inherently brittle. In fact, inside the shear bands the accommodated strain can be very large. The reason why metallic glasses are brittle at macroscopic level lies in that deformation is localized in the shear bands with other parts of the materials undeformed.

Although shear bands lead to shear softening of metallic glasses, abundant shear bands formation can enhance the plasticity and encourage the ductile fracture of metallic glasses. Bei et al. [69] showed that shear band density is directly related with plastic strain and hardness, as shown in Fig. 12. Interaction and multiplication of shear bands before final rupture can greatly enhance the fracture behaviors.

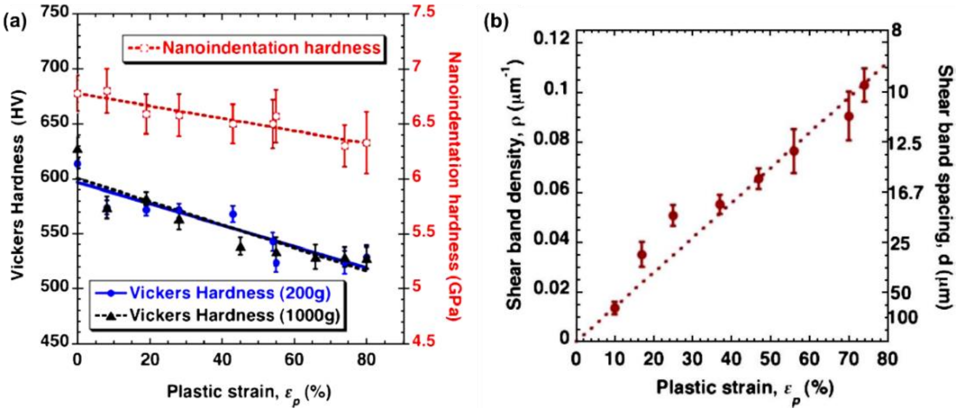

Figure 12. Relationship between hardness, plastic strain and shear band density [69]. Reprinted from H. Bei, S. Xie, E.P. George. Softening caused by profuse shear banding in a bulk metallic glass, Phys. Rev. Lett. 96 (2006) 105503, with permission from American Physical Society.

In addition, Xi et al. [70] show that correlation between fracture toughness and plastic zone size: a larger size of plastic zone leads to a larger fracture toughness. Sun and Wang et al. [44] compiled a diagram correlating the fracture toughness of materials and characteristic size on fracture surface, as shown in Fig. 13. Fracture surface filled with dimples indicates the most desired fracture toughness, then the vein-like pattern, nano-periodical stripes, and then the featureless zones. By directly measuring the feature sizes on fracture surface, the fracture behaviors of metallic glasses can be evaluated. As can be seen that, the fracture toughness of metallic glasses lies between ductile crystalline metals and alloys and the brittle oxide glasses. Studies and strategies to enhancement the fracture behaviors of metallic glasses such creating inhomogeneity and adding second phases, will not only benefit metallic glasses, but also be beneficial for metals and ceramics.

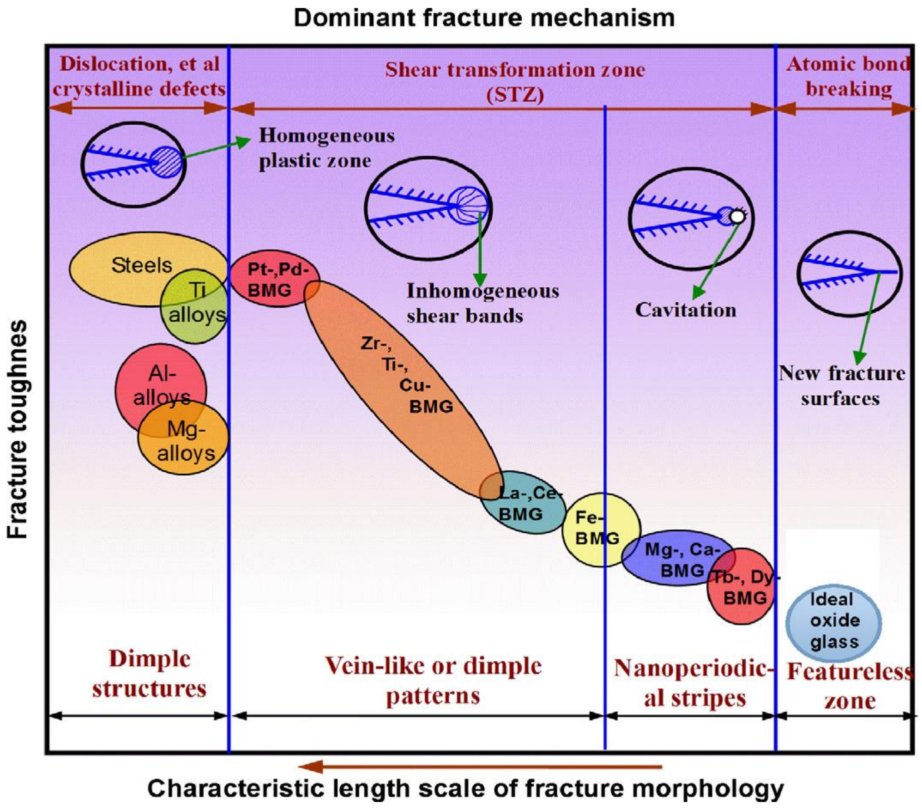

Figure 13. The relationship between fracture toughness, characteristic length scale of fracture morphology, and dominant fracture mechanism [44]. Reprinted from B.A. Sun, W.H. Wang. The fracture of bulk metallic glasses, Prog. Mater Sci. 74 (2015) 211-307, with permission from Elsevier.

I.2.5 Shear softening of metallic glasses

In the inhomogeneous flow region, upon deformation of metallic glasses, shear localization happens in shear bands associated with local structure change [36]. This structural change leads to the increase of free volume and lowering of viscosity. Polk and Turnbull [71] pointed out that the structure change results from the imbalance of two competing processes. The process which increases free volume comes from shear-induced disordering, and the process which decreases the free volume comes from diffusion controlled reordering.

At very large stress, atoms can be squeezed into a hole which contains smaller volume. The required energy to push the atom into a neighboring hole can be estimated by the elastic distortion energy which can be expressed as,

$$\text{Equation 9} \qquad \Delta G^{e} = \frac{2\mu(1+v)(V^{*}-V)^{2}}{3(1-v)V},$$

where ΔG^{e} is the elastic distortion energy, V^{*} is the volume before shear, V is the decreased volume after shear. However, as mentioned in the previous section, the decrease of free energy is $\tau\Omega$. Therefore, the critical volume for the atom to be squeezed into can be obtained by equaling two energies,

$$\text{Equation 10} \qquad \tau\Omega = \frac{2\mu(1+v)(V^{*}-V^{m})^{2}}{3(1-v)V^{m}},$$

where V^{m} is the critical hole size. The total created free volume then can be calculated by multiplying number of potential sites for the jumps, amount of free volume created by one atomic jump, and net result of forward and backward jumps.

In crystals, a vacancy (type of point defect) is very stable and is hard to annihilate, since the disappearance of a vacancy will disrupt the crystalline translational symmetry. However, in metallic glasses, the hole or "vacancy" can be annihilated after multiple diffusional jumps, because essentially amorphous systems lack of the long or medium range order. The total amount of free volume annihilated can be calculated by the jump frequency and free volume decrease associated with per atomic jump, which is stress irrelevant. At very low stress, shear-induced structural disorder is very limited. However, when the stress is sufficiently high, the free volume will increase and the viscosity will decrease. As a consequence, deformation of metallic glasses is only accommodated by the localized shear bands, and during subsequent deformation, structure disorder (dilatation) is promoted, leading to further softening of metallic glasses. Shear softening greatly impedes the applications of metallic glasses as structural materials. Therefore, how to delocalize shear deformation remains a main problem for the metallic glass community to solve.

I.2.6 Brief history of fabrication of metallic glasses

The first reported metallic alloys, $Au_{75}Si_{25}$, is fabricated by Klement et al [72] in 1960. In the early stage of fabrication of metallic glasses, very high cooling rate, as high as 10^6 K/s is required to ensure the formation of amorphous phase. The very high cooling rate prevents the atoms from reaching their equilibrium state or forming crystals. Instead, non-equilibrium state as in the form of amorphous structure is achieved with high cooling rate. The requirement of very high cooling rate limits the shape of metallic glasses into thin foils, ribbons, or wires, the geometry of which promotes cooling. Besides, the thickness of metallic glasses is limited to below 100 microns. The very popular fabrication method of amorphous alloys is melt spinning, along with mechanical alloy, physical vapor deposition, and ion irradiation. With the advancement of metallic glass fabrication, the required cooling rate can be low as several K/s. The reduced requirement for cooling rate leads to the fabrication of bulk metallic glass the smallest dimension of which should be larger than 1 millimeter. The term, glass formation ability (GFA), is introduced to describe the ability to form metallic glasses. Several parameters, such as atomic radius difference, number of elements, and heat of mixing, greatly affect the GFA [73]. By tailoring the element and composition, the GFA can be greatly enhance and thus the size of metallic glasses. Many metallic glasses become commercialized, such as the Vitreloy (ZrTi-based BMG) [62]. Thin film metallic glasses (TFMG) can be fabricated by physical vapor deposition such as sputtering. And the composition of TFMG can be tailored over a wide range and does not necessarily needs multiple elements due the very high cooling rate from vapor state to solid state. TFMG also has wide applications, such as microactuators, micogears, or nano-electromechanical systems. The study to improve the overall properties of TFMGs can promote their application in the related areas, and provides great insight in enhancing the properties of BMGs. Fabrication thin film metallic glass composites or constructing crystalline/amorphous multilayers is proved to be one effective method to circumvent the brittleness of metallic glass and improve the deformability.

I.3 Mechanical Properties of Thin Film Metallic Glass Composites

To significantly enhance the plasticity of crystalline/amorphous composites, it is essential to control the dimension and volume fraction of each phase, and systematically investigate the influence of interphase interfaces on tailoring the plasticity of these composites. Consequently thin film metallic glass composites (TFMGc) consisting of alternating amorphous/crystalline layers have been investigated recently. It is well known that the mechanical properties of crystalline metallic materials are closely related to the nucleation and propagation of dislocations, whereas MGs typically deform through shear bands or shear transformation zones (STZ) [34, 37-39]. Modeling and experimental studies on the mechanical properties of crystalline/crystalline multilayers have explored that the hardness can be dramatically increased by decreasing the layer thickness. This has been mainly ascribed to the change in deformation mechanisms of crystalline multilayers, which are related to layer thickness, interface structures and properties, and etc. And dislocation models were proposed to explain the mechanical behaviors of crystalline multilayer films [11-17]. Also the effects of different types of interfaces on deformation mechanisms of crystalline multilayers have been studied [18-23]. There are some possible strengthening mechanisms for crystalline metallic multilayers, which were summarized in Fig. 1.

Comparing with the extensive studies on mechanical behaviors of crystalline multilayer thin films, the studies on mechanical behavior of crystalline/amorphous multilayer films are limited [74-82]. Previous studies show that when the thickness of amorphous layers is sufficiently thin, certain crystalline layers can accommodate plasticity and counteract the shear deformation of amorphous alloys (or constrain the formation and propagation of shear bands), and increases the ductility of the crystalline/amorphous composites [83-85]. Wang et al. [86] showed that the Cu 35 nm/amorphous CuZr 5 nm multilayer films may achieve tensile ductility of ~14% with little work hardening, shown in Fig. 14.

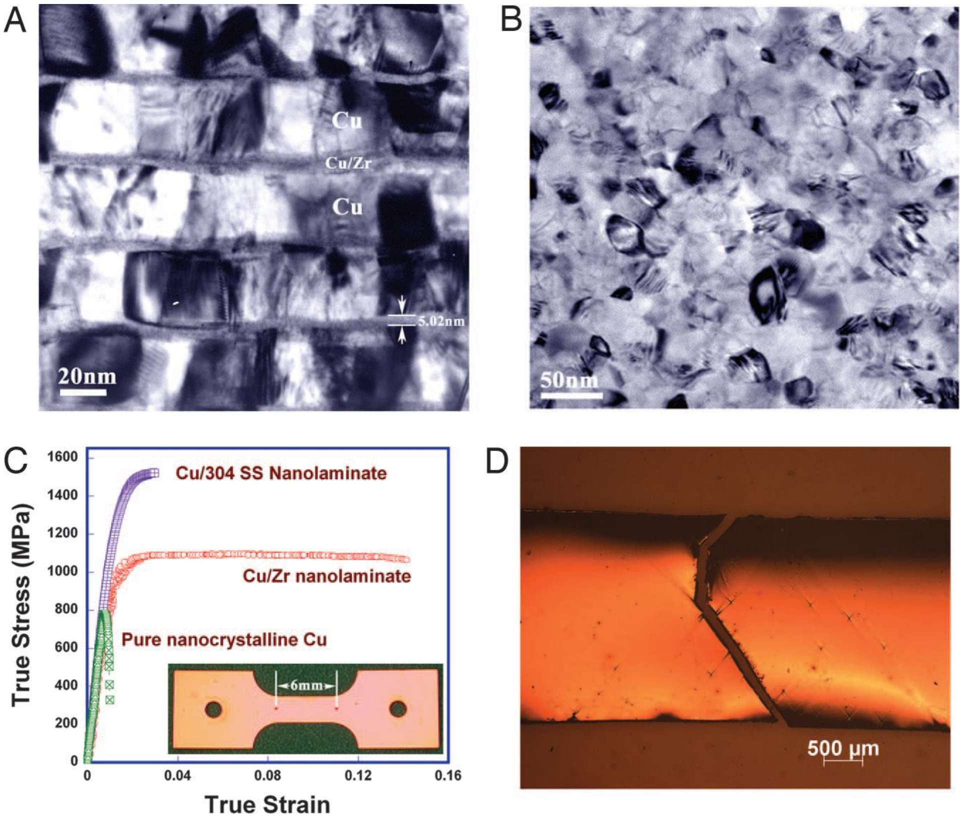

Figure 14. Cross-section (a) and Plan-view (b) TEM image of the Cu/a-CuZr nanolamiantes. (c) True stress strain curves comparison with other systems. (d) Gauge area after fracture [86]. Reprinted from Y. Wang, J. Li, A.V. Hamza, T.W. Barbee. Ductile crystalline–amorphous nanolaminates, Proc. Natl. Acad. Sci. 104 (2007) 11155-11160, with permission from National Academy of Sciences.

Some of the prior studies also suggest a transition of plastic deformation modes from pronounced shear banding to homogeneous co-deformation of the crystalline/amorphous multilayer composites as layer thickness changes [87-90]. Kim et al. [91] showed that Cu 16nm/amorphous CuZr 112 nm nanolaminates have higher strength and tensile ductility compared with pure amorphous CuZr because of deformation change. Guo et al. showed [92] that during nanoindentation and micropillar compression, by tailoring the layer thickness, the deformation mode of amorphous CuZr/Cu nanolaminates can be changed from shear banding to co-deformation of layers. As shown in Fig. 15, Donohue et al. [93] reported that during rolling of Cu 90nm/amorphous PdSi 10 nm multilayers, the shear instability of the amorphous layers is suppressed and the amorphous PdSi co-deform with the crystalline layers.

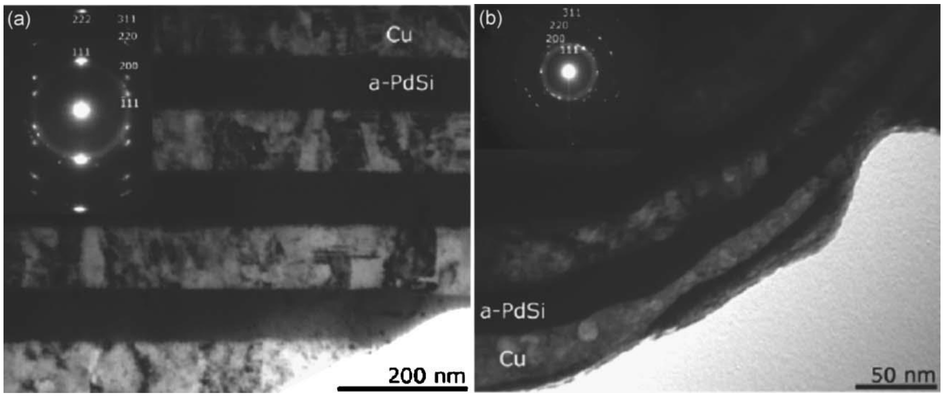

Figure 15. Suppression of shear band formation after rolling for Cu/a-PdSi multilayer. TEM image of Cu/a-PdSi before rolling (a) and after rolling (b) [93]. Reprinted from A. Donohue, F. Spaepen, R. Hoagland, A. Misra. Suppression of the shear band instability during plastic flow of nanometer-scale confined metallic glasses, Appl. Phys. Lett. 91 (2007) 241905, with permission from AIP Publishing LLC.

I.4 Strain Rate Sensitivity of Crystalline Metals and Metallic Glasses

Strain rate sensitivity (SRS, m) is an important parameter to evaluate the deformation behaviors of materials. It reflects the effect of thermal activation on deformation of materials. In specific, it measures the flow stress sensitivity to strain rate and can be expressed as,

Equation 11 $$m = \frac{\partial ln\sigma}{\partial ln\dot{\varepsilon}},$$

where σ is the applied stress and $\dot{\varepsilon}$ is the strain rate. A positive m value means a larger stress at higher strain rate. For crystalline materials, SRS is closely related with dislocations activity. m can also be related to another important parameter, activation volume (v^*), in following equation,

$$\text{Equation 12} \qquad m = \frac{\sqrt{3}kT}{\sigma v^*},$$

where k is the Boltzmann constant and T is the absolute temperature. Equation 12 shows that a smaller v^* leads to a larger m. v^* can be physically described in terms of dislocation motions as [94, 95],

$$\text{Equation 13} \qquad v^* = b\xi l^*,$$

where b is the Burgers vector of dislocation, ξ is the distance travelled by the glide dislocation during one activation event, and l^* is the segment length of dislocation in the thermal activation event. Apparently, a higher dislocation density results in a smaller activation volume (v^*).

For face-centered cubic (fcc) metals with relatively large grain size (*d*) , SRS increases with dislocation density; for fcc metals with nanograins or ultra-fine grains, SRS increases with decreasing grain size [95, 96]. On the contrary, for body-centered cubic (bcc) metals with nanograins or ultra-fine grains, SRS decreases with decreasing grain size, since the deformation mechanisms between fcc and bcc metals are different, and activation volume for bcc metals can be considered as a constant if *d* is below 1μm [95]. A comparison of effect of grain size on SRS is shown in Fig. 16.

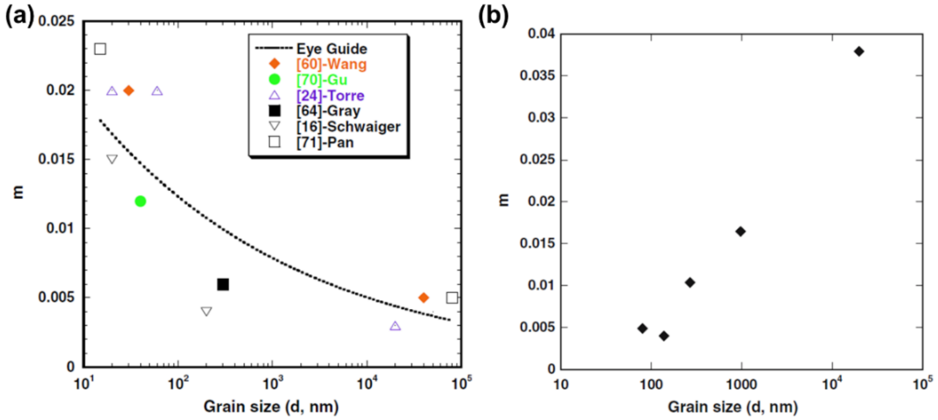

Figure 16. Strain rate sensitivity of typical fcc (Ni) and bcc (Fe) metals as a function of grain size [95]. Reprinted from Q. Wei. Strain rate effects in the ultrafine grain and nanocrystalline regimes—influence on some constitutive responses, J. Mater. Sci. 42 (2007) 1709-1727, with permission from Springer.

With the absence of dislocations, MGs are usually considered to be strain rate insensitive. Changing the strain rate/loading rates, the deformation behaviors can be greatly altered as manifested by the serrated flows during deformation: obvious serrated flows indicating inhomogeneous deformation at low strain rate and indistinct serrated flows indicating homogenous deformation at high strain rate [97-100]. These studies show that despite the effect of strain rate on serrated flows, strain rate has little effect on yield strength or hardness of MGs. However, both positive [101-103] and negative SRS [104, 105] have been reported for MGs. Positive SRS is claimed to be related with the decreased density of shear bands and inhomogeneous microstructure [101]. Negative SRS for MGs could result from nanocrystallization during deformation (deformation-induced devitrification), leading to local increase of temperature [106, 107]. High strain rate may lead to inefficient conduction of heat due to deformation-induced devitrification, resulting in a local decrease of viscosity and consequently lower hardness. SRS of MGc with a combination of amorphous and crystalline phases, however, is rarely studied, especially at the nanoscale [106].

I.5 Tribological Behaviors of Metallic Glasses and Metallic Glass composites

Tribology studies the interacting surface in relative motion [108]. Tribology exists essentially in every aspect of our daily life and industry. Both friction and wear are involved in the process of tribology. Friction is the force generated during the relative motion between two surfaces. Coefficient of friction (COF) states the relationship between normal force and lateral force and can be expressed as,

$$\text{Equation 14} \qquad \mu_{COF} = {}^{F_{lateral}}\!/_{F_{normal}},$$

where μ_{COF} is the coefficient of friction, $F_{lateral}$ is the lateral force, and F_{normal} is the normal force. Upon the relative motion between two surfaces, heat is generated because of friction. A smaller COF indicates better tribological behaviors, since less heat is generated during the process and the kinetic energy is more efficiently used.

Wear describes the graduate loss of mass or volume of materials associated with production of wear debris. Wear can cause a considerable amount of materials loss among the production/manufacturing in industry. By adding adequate lubrication and surface modification by surface engineering, wear behaviors can be greatly improved. Classical Archard equation shows the relationship between wear rate and materials properties [108, 109],

$$\text{Equation 15} \qquad \frac{dV}{dx} = \frac{KP}{H},$$

where dV is the volume loss during distant dx, K is dimensionless wear coefficient, P is the normal load, and H is the hardness of materials. According to this equation, the larger the hardness, the smaller the wear rate. During sliding wear, a thin tribo layer (as called Beilby layer) can be formed. If the tribolayer is hard enough, the wear scar can be smooth with less fluctuations for the COF. And this Beilby layer is usually amorphous [110].

In the absence of dislocations and grain boundaries, metallic glasses can be fabricated with superior surface flatness, and decrease of the surface asperities can alleviate the wear and energy loss by friction [26]. Outstanding yield strength and wear resistance along with superior surface condition make metallic glasses suitable engineering materials in tribological applications [1, 3, 6, 111]. As stated by Archard equation, various MGs demonstrate enhanced wear behaviors with the increase of hardness [112, 113], as shown in Fig. 17. However, hardness alone cannot describes the tribological process, since factors such as surface asperity, adhesion, heat, fracture behaviors, and deformation mechanisms greatly affect tribological behaviors. In fact, different testing techniques, temperature, and tip properties renders very different wear or friction coefficients for the same materials. For crystalline materials, sliding wear can cause severe plastic deformation of materials with very large plastic strain, and the microstructure right under the sliding surface could have reduced grain size, dislocations walls, obvious grain rotations compared with the microstructure further away [108]. For metallic glasses, sliding wear can trigger crystallization of amorphous phase [114].

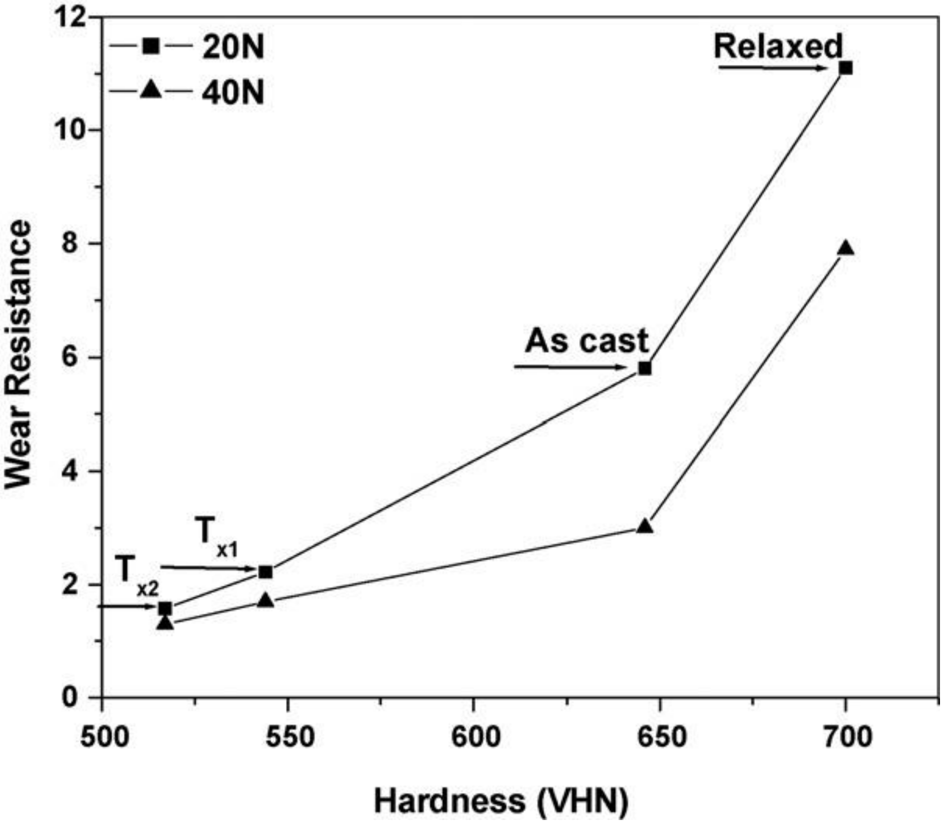

Figure 17. Wear resistance improves as the increase of hardness for Cu-based MGs [113]. Reprinted from J. Bhatt, S. Kumar, C. Dong, B. Murty. Tribological behaviour of Cu 60 Zr 30 Ti 10 bulk metallic glass, Mater. Sci. Eng., A 458 (2007) 290-294, with permission from Elsevier.

With the trend of miniaturization of devices, such as microelectromechanical systesms (MEMS), micromotors, and nanosensors, the tribology at the nanoscale becomes increasingly important. For instance, ultrathin coatings as thin tens of nanometers are used in devices of semiconducting industry, friction and wear behaviors plays a vital role in the performances of devices. Besides, thanks to techniques such as scanning probe microscope (SPM) and nanoscratch technique, *in situ* relationship between friction (morphology) and time (depth) can be obtained which greatly helps to underlying the wear mechanisms at nanoscale.

I.6 Scope and Goals

The scope of this thesis covers the mechanical properties of crystalline/amorphous nanolaminates. The amorphous phase chosen for this study is amorphous CuNb system. Unlike the commonly studied amorphous CuZr and PdSi systems, Cu and Nb atoms have a positive heat of mixing. This difference could lead to the different deformation behaviors. Mechanical behaviors of crystalline/amorphous nanolaminates discussed in this thesis include: strengthening mechanisms, fracture behaviors, friction response, and strain rate sensitivity.

Also, we show that size and architecture of nanolaminates have clear effect on mechanical behaviors. The mechanisms underlying the size effect have been intensively studied and how to optimize the mechanical properties *via* tailoring size is proposed. For example, by controlling the dimension of layer thickness, fracture surface of metallic glasses can form ductile dimples instead of featureless surface; strain rate sensitivity of crystalline/amorphous multilayers is layer thickness dependent (to the best of our knowledge, our study may be the first to report on the layer thickness dependent strain rate sensitivity of crystalline/amorphous multilayers). Overall, this thesis provides abundant experiments results on mechanical properties of crystalline/amorphous nanolaminates. Systematic studies on various aspects of mechanical properties provide deep insight on how materials properties are related and are beneficial for the design of crystalline/amorphous multilayers with designed performance, which promote their wide applications in flexible electronics, microelectromechanical system, and coating industry.

CHAPTER II

EXPERIMENTAL DETAILS

II.1 Magnetron Sputtering

Magnetron sputtering is one of the popular techniques among physical vapor deposition (PVD) to fabricate metallic thin films. In PVD, materials are vaporized first and consolidated on the substrate as the form of thin film. Another popular thin film deposition method, chemical vapor deposition (CVD), involves chemical reaction instead of solely physical process. Methods such as heating or sputtering can vaporize atoms in gaseous state. Sputtering process involves the generation of plasma, bombardment of plasma onto the target, emitting of target atoms, and condensation of target atoms on the substrate. The plasmas usually consists of inert gaseous which prevents the reaction between plasma and target atoms. Magnetron sputtering utilizes magnets to confine the position and shape of the plasma, as a result, deposition rate can be improved. Cu/a-CuNb multilayers will be deposited on Si substrates by direct current (DC) magnetron sputtering at room temperature. Deposited films by magnetron sputtering has the similar composition as the target materials. By choosing a compound target or depositing several target materials at the same time (co-sputter), films can be deposited with various elements, and co-sputter allows the adjustment of composition of films. Compared with thermal evaporation, deposited atoms have much larger kinetic energy by magnetron sputtering, and the deposited films have better adhesion with the substrate and a higher density. During the condensation of atoms, cooling rate is very high. Deposition rate can be tailored by parameters such as deposition angle, power, distance between target and substrate, and substrate bias. Sputter deposition is widely used in semiconducting, hard disk, and coating industry.

Deposition in this study utilizes magnetron sputtering system in Zhang Group. Direct Current (DC) power is chosen as the power supply. Both 3 inch sputter guns and targets are used. The chamber was evacuated by and in the order of mechanical pump, turbomolecular pump and cryopumps to a base pressure lower than 1×10^{-7} Torr, and 1-3 $\times$ 10^{-3} Torr Ar was used during deposition. In this case, argon atoms form plasma. Amorphous layer, a-CuNb, were deposited by co-sputtering with a composition of Cu 50 at.% and Nb 50 at.% ($Cu_{50}Nb_{50}$). General deposition rate for Cu, Nb, and CuNb is 0.29 nm/s, 0.38 nm/s, and 0.39 nm/s respectively. The associated power for the deposition rate is 400 W for Cu deposition, 300 W for Nb deposition, and 300W for Nb and 111W Cu for co-deposition. Thin films deposited on silicon substrates are used for hardness measurement, microstructure characterization, and etc. The thin films were also deposited on polyimide (Dupont^{TM} Kapton, type HN film) to study their tensile behaviors. Kaptons used in this study were pre-cut into dog bone shapes, and the thickness of Kapton is 25.4 μm. The dimension for the dog bone samples is 7 mm×26 mm, and the gauge area is 3 mm × 8 mm. Magnetron sputter system employed gives very high cooling rate for the amorphous CuNb system over a wide range of composition.

II.2 Nanoindentation

Indentation test differs tensile and compression tests in several ways. Tensile and compression tests reveal the mechanical properties of the whole tested specimen and have specific requirements during the specimen preparation. Indentation test measures the mechanical properties of a small part of the specimen. Hence, the tested specimen can have very small size and be easy to prepare. During indentation, an indenter tip with known properties (usually very hard) is pressed into the tested materials. The most important mechanical properties obtained from indentation are hardness and modulus. Hardness measured how resistant of materials upon plastic deformation under compression. Vickers, Rockwell, or Brinell hardness can be obtained by different testing techniques. The yield strength from tensile and compression tests usually can be estimated from hardness through an empirical relationship. For example, the relationship of Vicker's hardness and tensile yield strength can be expressed as,

Equation 16 $$\sigma_y = HV/0.3,$$

where HV is the Vicker's hardness. Because of the ease of specimen preparation and efficient testing process, indentation test is widely used in the field of science, engineering, and industry.

Nanoindentation investigate the mechanical properties of materials with a very small volume which renders more useful information in many real applications. Such applications include measurement of coatings, devices or materials at nanoscale, mechanical properties at a certain depth or position of the specimen. Traditional indentation technique at micro scale or larger obtain hardness from the following equation,

Equation 17 $$H = P_{max}/A,$$

where P_{max} is the applied maximum load and A is the residual contact area. Nanoindentation tests the specimen at nanoscale with a precise and well defined indenter tip which can be as small as several hundred nanometers. The drawback back then is how to measure the residual contact area which is very hard to observe under optical microscope and is very time-consuming to measure by scanning electron microscopy or atomic force microscope. The problem later was overcome by indenting with an indenter tip with known geometry. Then the area (A) at certain depth can be calculated by the indentation depth (h). However, the determination of the real area can be tricky since deformation of specimen is both plastic and elastic and the real contact depth is also hard to obtain. To date, most nanoindention techniques uses the Oliver-Pharr method [115, 116], which accurately gives the materials properties such as hardness and modulus. The detailed information during the loading process and after unloading can be illustrated in the following Fig. 18.

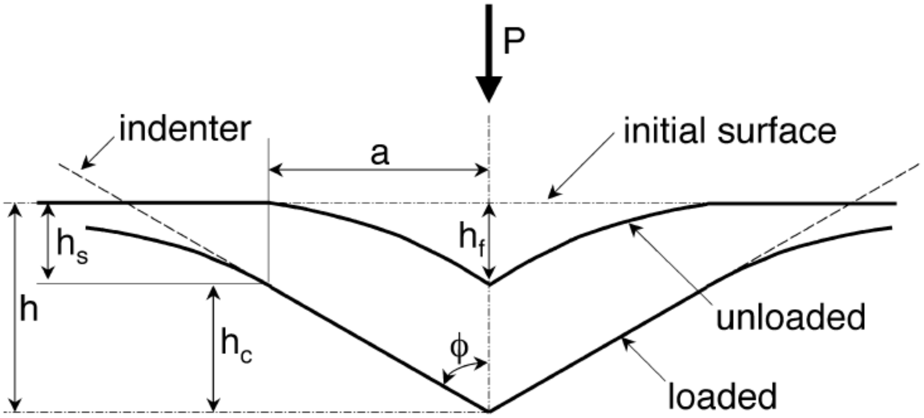

Figure 18. Schematic illustrates the key parameters before and after unloading [116]. Reprinted from W.C. Oliver, G.M. Pharr. An improved technique for determining hardness and elastic modulus using load and displacement sensing indentation experiments, Journal of materials research 7 (1992) 1564-1583, with permission from Cambridge University Press.

As shown in the schematic, the total indentation depth h is the sum of h_c, contact depth, and h_s, the sink-in depth, of the surface around the indenter,

Equation 18 $$h = h_c + h_s.$$

The radius of the contact area is a. The final depth of the residual indent, h_f , is the plastic deformation that can be recovered after unloading. $\emptyset$ Is the angle of the indenter tip. Different indenter geometry has different angle. For a conical indenter, this angle is 70.3°. If the sink-in can be estimated by [116]:

Equation 19 $$h_s = \frac{\epsilon P_{max}}{S},$$

where ϵ is a constant related with indenter geometry, P_{max} is the maximum load, and S is the stiffness of materials. And ϵ is 0.72, 0.75, and 1 for conical, paraboloid, and flat tip, respectively. Therefore the real contact depth can be expressed as,

Equation 20 $$h_c = h - \frac{\epsilon P_{max}}{S}.$$

Based on the obtained contact depth, the contact area then can be calculated by using area function of the tip. Thus the hardness is obtained through Equation 17 .It should be noted that this method omits the influence of surface pile-up which will change the contact area. But if pile-up is not significant during indentation, the method generally provides very accurate hardness value.

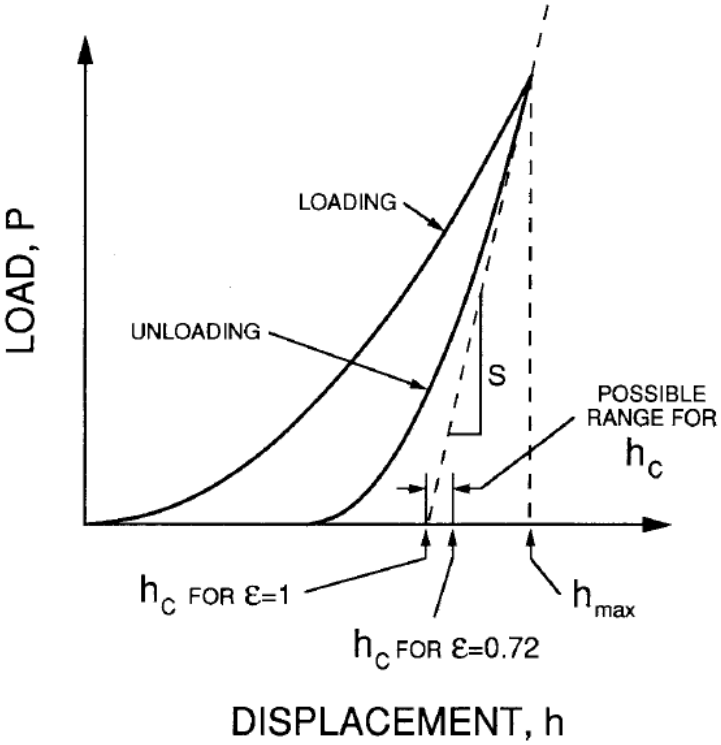

Figure 19. Typical load displacement during nanoindentation [115]. Reprinted from W.C. Oliver, G.M. Pharr. Measurement of hardness and elastic modulus by instrumented indentation: Advances in understanding and refinements to methodology, J. Mater. Res. 19 (2004) 3-20, with permission from Cambridge University Press.

Stiffness of tested materials can be obtained from the unloading portion from the unloading part of load-displacement curve using,

Equation 21 $$S = \frac{dP}{dh}.$$

Once stiffness and contact area is acquired, the effective modulus, E_{eff}, can be derived from,

Equation 22 $$E_{eff} = \frac{S\sqrt{\pi}}{2\beta\sqrt{A}},$$

where β is a dimensionless parameter which is usually taken as 1. It should be mentioned that this effective modulus, or so called measured modulus results from the modulus from both the moduli of tested materials and indenter tip. The relationship between them can be expressed as,

Equation 23 $$\frac{1}{E_{eff}} = \frac{1-v^2}{E} + \frac{1-v_i^2}{E_i},$$

where E and v (E_i and v_i) is the modulus and Poisson ratio of the tested materials, respectively. However, the widely used tips for nanoindentation is made from diamond which has much larger modulus compared with common tested materials, so E_{eff} is comparable to E.

One key process to obtain accurate hardness and modulus from nanoindentation is to have the accurate area function. Theoretically, the contact area can be approximated from contact depth by,

Equation 24 $$A = C_0 h_c^2 + C_1 h_c^1 + C_2 h_c^{1/2} + C_3 h_c^{1/4} + \cdots.$$

Parameters before the contact depth depends on the tip geometry. As can be told from the equation, at larger contact depth, contributions from the later terms have smaller values. Therefore, a good estimate of contact area can be obtained for large contact depth indentation by using the simplified version,

Equation 25 $$A = C_0 h_c^2.$$

And for a Berkovich tip, C_0 is 24.5. However, during shallow nanoindentations where the contact depth is very small, the contribution from the latter terms become non-negligible. A careful calibration of the area function through measuring the materials with known hardness and modulus at various depths is required to obtain reliable data. Besides, in practical applications, the indenter tip can be wore out or experience slight geometry change. Thus, routine calibration of indenter tip is necessary for accurately measuring the data.

Hardness of films was measured by instrumented nanoindentation techniques in this study. Both Fischerscope HM 2000XYp (Fischer Technology, Sofia, Bulgaria) and Hysitron TI 950 TriboIndenter (Hysitron, Inc. Minneapolis, MN) were employed and uses Oliver-Pharr method. In order to avoid the hardness error from inhomogeneity of films, at least 12 good indentations were performed at various locations in the films in order to obtain reliable hardness and modulus data. Besides, Hysitron TI950 TriboIndenter is also used to acquire scanning probe microscopy images before and after indentation and perform strain rate sensitivity study. In addition, Hysitron PI87 PicoIndenter (Hysitron, Inc. Minneapolis, MN) is utilized to perform *in situ* micropillar compression tests.

II.3 Transmission Electron Microscopy

Transmission electron microscopy (TEM) is one microscopy technique which acquires an image by transmission of generated electrons through a tested specimen. TEM was developed by Max Knoll and Ernst Ruska in 1931, and Ruska won the Nobel Prize in physics for his development of TEM. Electron beam interacts with atoms and then transmits through the specimen. Since TEM requires transmission of electrons, specimen for TEM characterization needs to be very thin, usually thinner than ~ 100 nm. Due to the high energy of the electron beam and corresponded smaller wavelength, TEM is able to resolve features at very fine scale. Advanced TEM can have a resolution of several angstroms or less, enough to resolve a single column of atoms. The advantages of TEM make it a critical analysis technique in the field of physical, chemical and biological science.

TEM system generally consists of several components: electron source, lenses and aperture, specimen holder, and imaging system and runs in high vacuum environment. Among many other reasons for requirement of high vacuum, to increase the free mean path of electrons and generation of high voltage in electron sources are the main reasons. The vacuum needs to be 10^{-7} to 10^{-9} Pa or better for an electron gun to operate without generation of electric arc. Poor vacuum can cause serious problems such as damage of electron gun, contamination of specimen, and bad resolution.

Electron source generates electrons usually by heating the filament on the negative electrode. The generated electrons are then accelerated by a positive electrode (anode). As shown in the following Fig. 20. Materials such as Tungsten and LaB6 are usually chosen for filament.

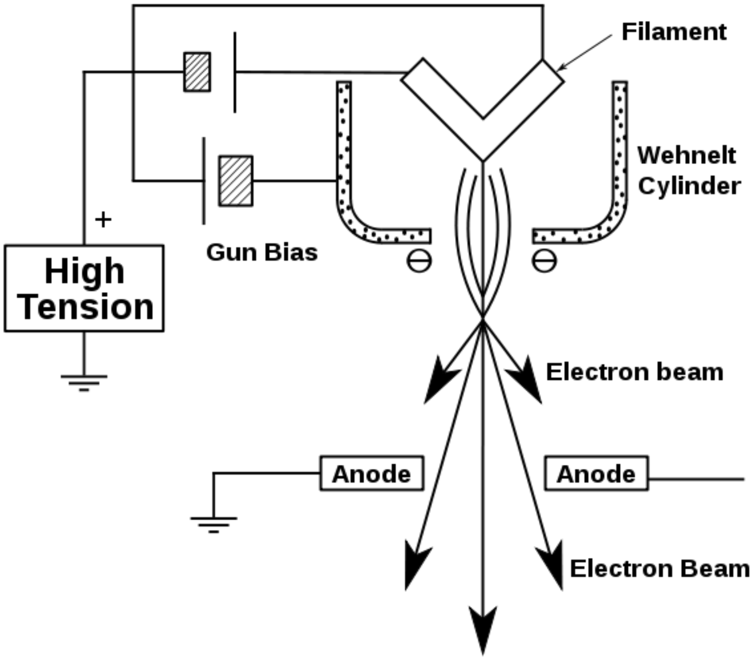

Figure 20. Schematic to show the structure of electron source.

Electron lens are used to focus electrons both electrostatically and magnetically. Not well focused beam can cause apparent astigmatism which deteriorates the results. Therefore, lens must be well aligned and symmetrical. Apertures are metal plates which blocks scattered electrons causing aberrations. A series of lens and apertures are used in TEM to achieve coherent beam and for various applications. Then the coherent and desired electron beam interacts with and transmits through the specimen in the sample holder. Since the sample holder will be in the TEM column with high vacuum physically, it requires airlocks to prevent the vacuum loss during insertion and removal process. Besides, TEM sample holder should holder the specimen and move its position inside TEM. There are various TEM holders for applications such as *in situ* heating, *in situ* nanoindentation, and cryo applications. The transmitted electrons are focused by objective lens to form an image. Objective apertures can also be used to block the transmitted electrons with high angle.

Various imaging modes are available in TEM. Bright field (BF) imaging is the most common one. The image contrast comes from the unscattered electrons, which pass through the specimen without interaction with specimen. Since specimen areas with larger thickness or higher atomic numbers will scatter more electrons, these regions will appear dark in formed image. In selected area diffraction (SAD) imaging, magnetic lens need to be adjusted so that the back focal plane is placed on the imaging apparatus, and parallel electrons transmit through thin area of specimen and are elastically scattered after interaction with specimen. Based on Bragg's law, electrons interacted with atoms of the same atomic spacing are scattered by the same angle. Therefore, generated SAD pattern can show crystalline orientation, atomic arrangements and etc. Typical single crystalline materials have a pattern of discrete dots, nanocrystalline materials have connected dotted line or circles, and amorphous alloys have diffused rings in SAD mode. In dark field (DF) imaging, objective aperture can be used to select a certain diffraction dot and the unscattered electrons which cause this diffraction dot are excluded. DF image can be used to identify the defect type in crystals or to observe crystals in amorphous matrix. In electron energy loss spectroscopy (EELs), electrons are scattered with energy loss in an inelastic manner.

TEM can also be worked as scanning electron microscope (STEM) in which electron beam is focused in a small spot and scanned across the whole sample to form an image. The beam then can be collected by using detectors. In STEM mode, higher atomic numbers lead to brighter image contrast. The information of non-transmitted electrons can be obtained by using annular dark field (ADF) detector. And high angle annular dark field (HAADF) imaging can resolve features with atomic resolution. STEM mode can also be equipped with energy dispersive X-ray (EDX) spectroscopy to perform chemical analysis.

TEM studies were performed by different microscopes at Texas A&M Microscopy and Imaging Center. The JEOL 2010 microscope was used to perform conventional TEM imaging and *in situ* heating experiments. This microscope has a working voltage of 200kV and is equipped with a LaB_6 filament. For high resolution TEM (HR) imaging and chemical analysis, FEI Tecnai G2 F20 ST is employed. HADDF-STEM can be achieved in this microscope for chemical composition analysis.

II.4 X-ray Diffraction

X-ray diffraction (XRD) is a technique that is commonly used to study crystalline orientation, film texture, and atomic structure without damaging specimen. Especially for sputter-deposited thin films, smooth surface allows direct investigation of film orientation without sample preparation. When X-ray interacts with atoms, X-ray can be elastically scattered through the electrons of atoms. The scattered X-ray (electromagnetic radiated waves) would cancel each other in many directions, but could form diffraction pattern in certain directions when they conforms to the Bragg’s law, as shown in Fig. 21. The Bragg’s law describes the angle in which the interaction between waves does not cancel each other but leads to maximum intensity, and can be expressed as,

Equation 26 $2dsin\theta = n\lambda,$

where θ is the incident angle, d is the spacing between two crystal planes, λ is wavelength of the X-ray, and n is an integer.

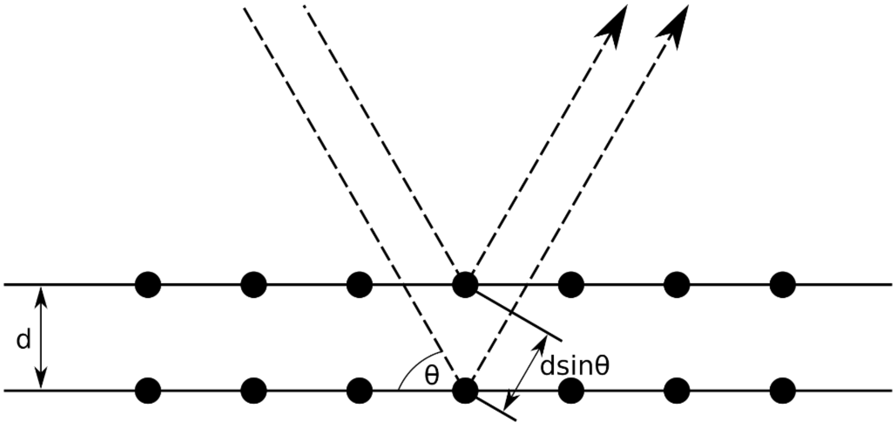

Figure 21. Schematic to illustrate Bragg's law.

For crystalline materials, XRD results show a sharp peak with very high intensity. And according to the crystalline structure, different planar spacing will leads to different angle in XRD results. Due to the lack of crystalline symmetry, amorphous alloys do not have a specific angle corresponding a specific crystalline orientation. Instead, a broad peak ranging over dozens of degrees would appear in XRD results. XRD can be used to identify if crystals exist in amorphous matrix or the alloys is fully amorphous.

In this study, XRD experiments were performed using a diffractometer (Empyrean 2, PANalytical, Almelo, NL). The instrument is operated using Cu Ka radiation which has a wave length of 1.5418 angstrom. For most of the cases, conventional 2θ scan results were acquired.

CHAPTER III

UNUSUAL SIZE DEPENDENT STRENGTHENING MECHANISMS OF CU/AMORPHOUS CUNB MULTILAYERS[*]

III.1 Overview

Nanostructured crystalline/amorphous metallic multilayers have been increasingly studied due to their high strength and potential enhancement of plasticity in amorphous metals. Here we report on mechanical behaviors of Cu/amorphous CuNb multilayers that were prepared by magnetron sputtering with equal individual layer thickness (h) varying from 1 to 200 nm. A medium-range-order amorphous CuNb layer formed between Cu and amorphous CuNb layers. This intermediate layer facilitates transmission of plasticity from Cu to amorphous layers by preventing the smear of dislocation core on the interface. The maximum hardness of Cu/amorphous CuNb multilayers is achieved when $h \leq 50$ nm, and is much lower than the hardness of single-layer amorphous CuNb films. Molecular dynamics simulations show that, comparing with single-layer amorphous CuNb, the pile-up of dislocations in Cu layers lowered the stress for the activation of shear transformation zones in amorphous CuNb layers in multilayers.

---

[*] This chapter is reprinted with permission from “Unusual size dependent strengthening mechanisms of Cu/amorphous CuNb multilayers” by Z. Fan, S. Xue, J. Wang, K.Y. Yu, H. Wang, and X. Zhang, *Acta Materialia*, Volume 120, pp 327-336, Copyright 2016 by Elsevier.

III.2 Introduction

Amorphous metallic alloys, or the so-called metallic glasses (MGs), show extraordinary yield strength, elastic strain, and wear resistance [1-6]. But their poor ductility and catastrophic failure associated with the formation and rapid extension of shear bands hinder their structural applications. Intrinsically, better ductility/toughness can be achieved by optimizing composition and structure (coordination) of MGs [44, 45]. Mechanical behaviors of BMGs can be altered by processing conditions and thermal history [51-53], free volume [35, 36, 41, 54], composition and structural inhomogeneity [55-59]. In addition, the deformation behaviors of MGs appear to be size dependent [117-119], which is also a subject of interest in this study. Homogeneous deformation (under uniaxial compression) has been observed [60] in amorphous PdSi pillars with diameters of 400 nm or less, in comparison to the shear band formation in pillars with larger diameters. Similarly the variation of deformation mode was also reported during tension tests of amorphous pillars [61]. Extrinsically, second phases can also enhance the ductility/toughness of MGs [7, 8, 120]. Previous studies showed [62] that ZrTi-based bulk metallic glass composites (BMGcs) may have extraordinary tensile ductility (more than 10%) without loss of their high strength because the plastically deformed “soft” phases become sites that promote more shear bands, which would then be stalled by the “hard” surrounding regions that require larger stress to be deformed. The strategy of using ductile crystalline phases to improve ductility of metallic glass matrix has also been applied to Zr-, Mg-, and Ti-based MGc [63-67].

To significantly enhance plasticity of crystalline/amorphous (C/A) composites, it is essential to control the dimension and volume fraction of each phase, and investigate the influence of interphase interfaces on plasticity of these composites. Thus thin film metallic glass composites (TFMGc) consisting of alternating C/A layers have been investigated recently. It is well known that mechanical properties of crystalline metallic materials are tied with nucleation and propagation of dislocations, whereas MGs typically deform through shear bands or shear transformation zones (STZ) [34, 37-39, 121]. The mechanical strength of C/C (crystalline/crystalline) multilayers can be tailored by varying individual layer thickness and types of layer interfaces (e.g. coherent vs. incoherent) [18-23, 122], and the strengthening mechanisms in these multilayers have been intensely investigated [11-17, 123]. Comparing with the extensive studies on C/C multilayer films, the studies on mechanical behavior of C/A multilayer films are limited [74-82]. Previous studies show when the thickness of amorphous layers is sufficiently thin, crystalline layers can accommodate plasticity and counteract the shear deformation of amorphous alloys (or constrain the formation or propagation of shear bands), and increases the ductility of the C/A multilayer composites [83-86]. Prior studies also suggest a transition of plastic deformation modes from pronounced shear banding to homogeneous co-deformation of C/A layers when layer thickness reduces [87-93]. Most previous studies show that the peak hardness of C/A multilayers approaches or even exceeds the hardness of single layer amorphous metal films [74, 75, 88, 91, 92].

In spite of these previous studies, numerous aspects remain to be investigated in C/A multilayer composites. First, most prior studies focus on amorphous systems (a-CuZr and a-PdSi) wherein the constituents (elements) have negative heat of mixing. There are few studies on amorphous systems consisting of elements with positive heat of mixing. Second, the C/A interfaces require further investigation. As the deformation modes of crystalline and amorphous layers are drastically different, the co-deformation of the multilayers, if accomplished, is largely dominated by the C/A interfaces. In fact, Cu/a-CuZr multilayer films with gradient C/A interfaces have better strength and ductility compared with sharp interfaces [124].

In this paper, we investigate the size-dependent strengthening mechanisms in Cu/a-CuNb multilayers for the following reasons. On the one hand, a-CuNb contains elements with positive heat of mixing (ΔHmix is 3 kJ/mol for Cu-Nb, compared with -23 kJ/mol for Cu-Zr [73]). On the other hand, the strengthening mechanisms of Cu/a-CuNb have not been investigated before, and can be compared to the intensively studied Cu/Nb and Cu/a-CuZr systems. Detailed microscopy and nanoindentation studies show that the maximum strength of Cu/a-CuNb multilayers is much lower than that of Cu/a-CuZr and single layer a-CuNb. Such large difference arises from the formation of an intermediate a-CuNb layer (with semi-crystalline nature) along interfaces. Furthermore MD simulations show that dislocation pile-ups in Cu layer significantly reduce the barrier strength of the C/A interface by facilitating the activation of STZs in a-CuNb. This study sheds light on the design of C/A multilayers by tailoring the amorphous structure along interfaces, and highlights the needs to investigate plasticity of amorphous systems consisting of elements with positive heat of mixing.

III.3 Experimental

Cu/a-CuNb multilayers were deposited on Si substrates by direct current (DC) magnetron sputtering at room temperature. The multilayers were designed with identical individual layer thickness (h) ranging from 1 to 200 nm. The chamber was evacuated to a base pressure lower than 1×10^{-7} Torr, and $1\text{-}3 \times 10^{-3}$ Torr Ar was used during deposition. a-CuNb layers were deposited by co-sputtering Cu and Nb to achieve a composition of Cu 50 at.% and Nb 50 at.% ($Cu_{50}Nb_{50}$). The total thickness of Cu/a-CuNb multilayers ranges from 1 to 3.2 µm and the a-CuNb layer is always the cap layer for all the multilayer films. Single layer Cu and a-CuNb films were also deposited as references. Specimens for cross-section transmission electron microscopy (XTEM) studies were prepared by grinding, polishing, followed by low energy Ar ion milling/polishing. An FEI Tecnai G2 F20 microscope operated at 200 kV was employed to study the microstructure and chemistry of the films. Scanning transmission electron microscopy (STEM) and energy dispersive X-ray (EDX) analysis were conducted using a Fischione ultra-high resolution high angle annular dark field (HADDF) detector with 0.23 nm special resolution in the STEM imaging mode, and an Oxford Instruments detector with a spatial resolution of ~1 nm attached to the Tecnai F20. X-ray diffraction (XRD) patterns were acquired on a diffractometer (Empyrean 2, PANalytical, Almelo, NL). The hardness and elastic modulus of the specimens were determined by using the instrumented nanoindentation technique [115] on a Fischerscope 2000XYp nano/micro indenter. A minimum of 25 indents was used to obtain an average hardness value at various indentation depths. The hardness of the specimens was determined as the hardness plateau in the plots of hardness vs. indentation depth [125, 126]. A Hysitron TI 950 TriboIndenter was also employed to perform partial loading/unloading indentations to obtain the hardness and modulus at various depths, and probe pop-in events during indentation. Both methods confirm the hardness trend in this study.

III.4 Results

III.4.1 Microstructure

The XRD profiles of Cu/a-CuNb multilayers with different h are compared to that of a-CuNb films in Fig. 22a. The amorphous peak in single layer a-CuNb is at ~ 39^o. The interplanar spacings of Cu (111) and Cu (200) in Cu/a-CuNb multilayers match that of bulk Cu (dashed lines) when h > 50 nm. The intensity of Cu (111) (Cu (200)) peak gradually increases (diminishes) with decreasing h. A slight left shift of Cu (111) peaks was observed, corresponding to a moderate in-plane compressive stress in multilayers. When h = 10 nm, the Cu (200) peak disappears. When h = 1 and 2.5 nm, a broad peak was observed as shown in Fig. 22b, which can be decomposed into three peaks, corresponding to the a-CuNb, Cu (111), and a middle peak with the d-spacing of 1/2($d_{a\text{-CuNb}}$+$d_{Cu(111)}$).

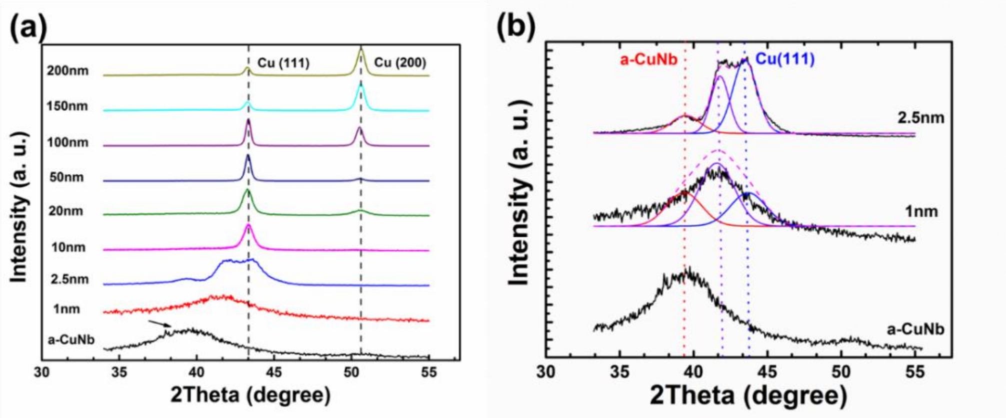

Figure 22. (a) The XRD profiles of Cu/a-CuNb multilayers (with individual layer thickness h=1-200nm) show Cu layers with (111) and (200) texture and amorphous humps from a-CuNb layers. (b) Peak deconvolution of the XRD profiles of Cu/a-CuNb 2.5 nm and 1 nm multilayers. A middle peak emerges with inter-planar spacing identical to the average of a-CuNb and Cu (111).

We further characterized microstructures of Cu/a-CuNb multilayers using TEM. The XTEM micrograph of Cu/a-CuNb 50 nm multilayers in Fig. 23a shows clear layer interfaces, and the average columnar grain size of Cu is comparable to layer thickness. In addition, nanotwins and stacking faults are frequently observed in Cu layers. The selected area diffraction (SAD) pattern of Cu/a-CuNb 50 nm in Fig. 23b shows an amorphous ring arising from a-CuNb, and the continuous diffraction ring due to the formation of nanocrystalline Cu. Similarly XTEM micrographs of Cu/a-CuNb 10 nm and Cu/a-CuNb 100 nm multilayers in Fig. 23c and 23d show abrupt layer interfaces and the formation of alternating a-CuNb and Cu layers. The columnar grain size of Cu in Cu/a-CuNb 10 nm multilayers is slightly greater than layer thickness, and the grain size of Cu is comparable to layer thickness in Cu/a-CuNb 100 nm multilayer.

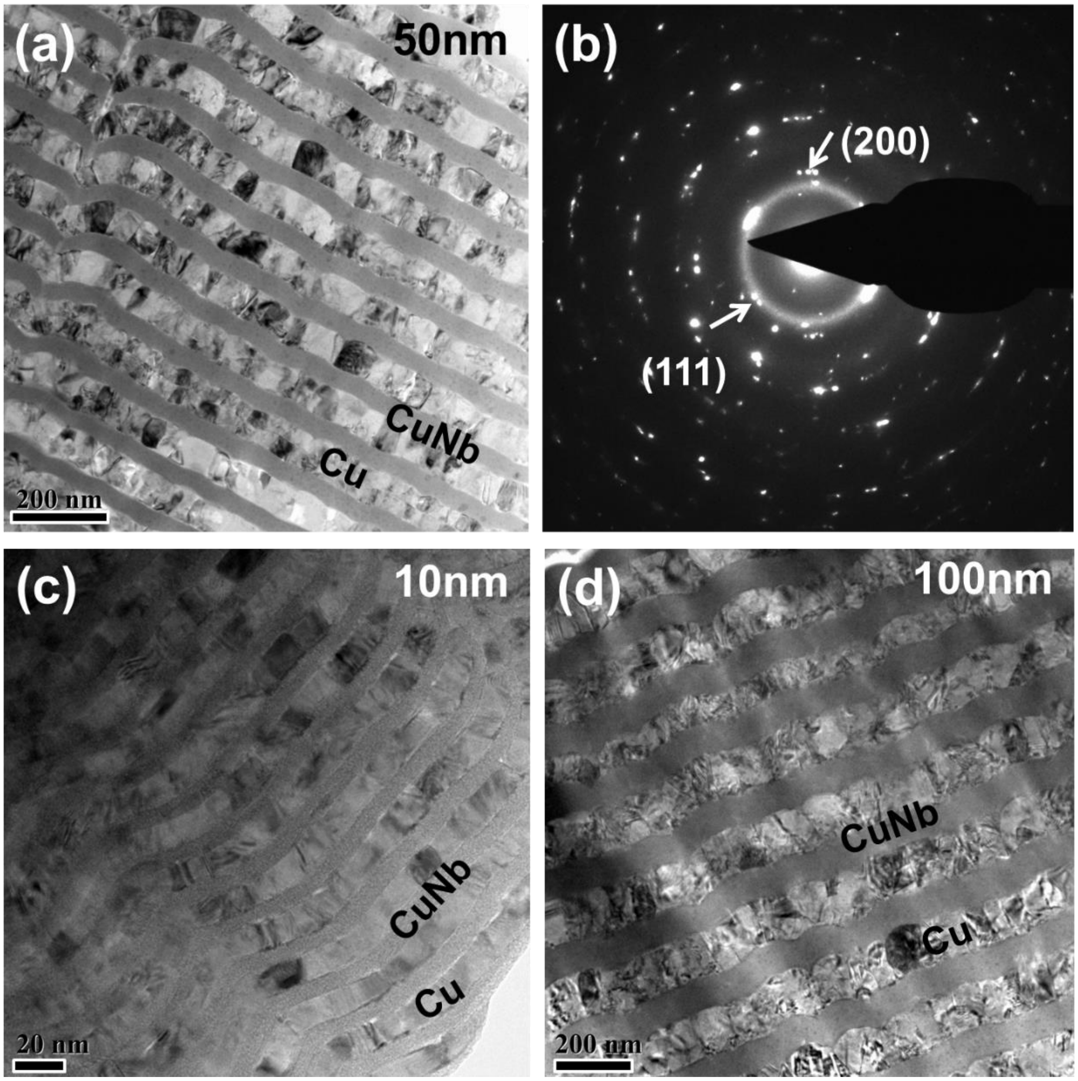

Figure 23. Cross-sectional TEM micrographs of Cu/a-CuNb multilayers with different individual layer thickness. (a) XTEM image of Cu/a-CuNb 50 nm multilayer shows alternating nanocrystalline Cu and featureless amorphous CuNb layers with clear layer interfaces. (b) SAD pattern of the Cu/a-CuNb 50 nm multilayer shows semi-continuous Cu (111) and (200) diffraction dots and the diffuse halo ring from a-CuNb layer. (c-d) XTEM micrographs of the Cu/a-CuNb 10 nm and 100 nm multilayers with discrete layers and abrupt layer interfaces.

Fig. 24 shows the HRTEM micrographs of Cu/a-CuNb 2.5 nm, 10 nm, and 50 nm multilayers. The amorphous CuNb in the interfacial regions appears to contain extremely fine semi-crystalline structures, implying the emergence of a medium-range-order (MRO) type of structure, as marked by the arrows. The fraction of interfacial layer with MRO increases with decreasing h. For the Cu/a-CuNb 2.5 nm multilayer, the thickness of interfacial MRO layers is comparable to h.

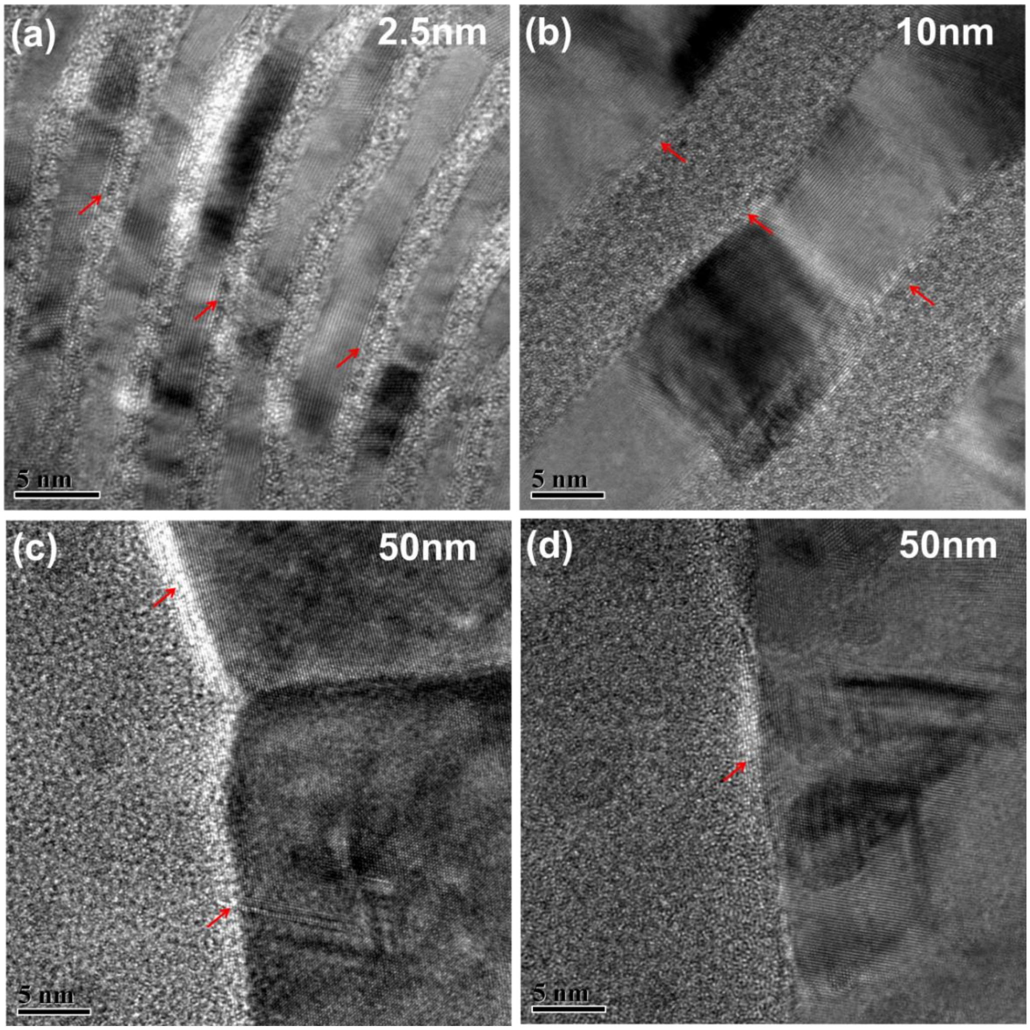

Figure 24. High resolution TEM (HRTEM) images of (a) Cu/a-CuNb 2.5 nm, (b) Cu/a-CuNb 10 nm, and (c-d) Cu/a-CuNb 50 nm multilayers. In the a-CuNb layers, extremely thin (several monolayer thick) semi-crystalline layers are observed as indicated by the arrows.

III.4.2 Mechanical behaviors of Cu/a-CuNb multilayers

The size dependent evolution of indentation hardness (H_{IT}) of Cu/a-CuNb multilayers (squares) in Fig. 25 shows that when h decreases from 200 to 50 nm, the hardness of multilayers increases monotonically, following the Hall-Petch relation as indicated by the dashed line. When h < 50 nm, the hardness of Cu/a-CuNb multilayers reaches a plateau, ~4.5 GPa, and is independent of h.

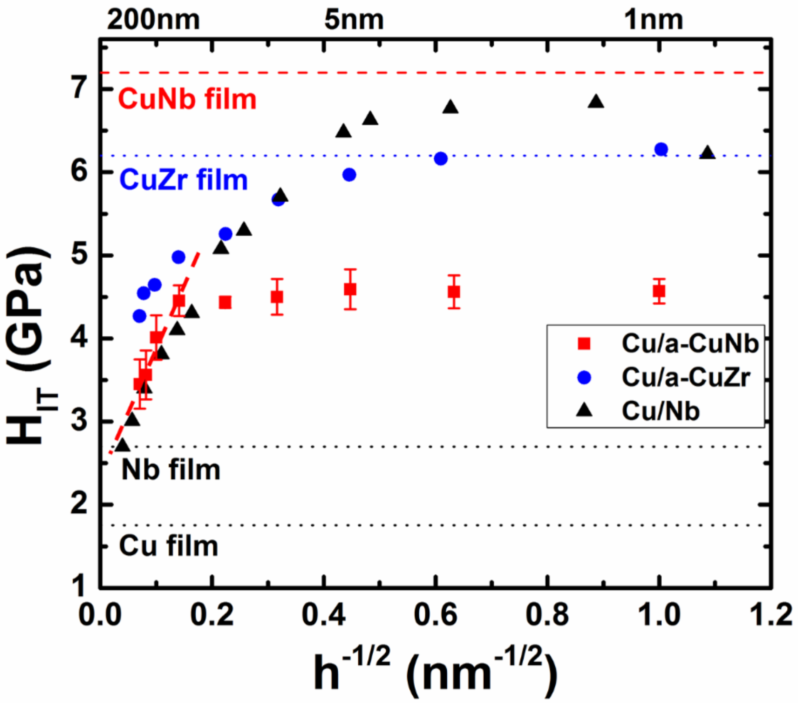

Figure 25. Comparison of indentation hardness of Cu/Nb [11], Cu/a-CuZr [75], and Cu/a-CuNb multilayers. A linear fit for Cu/a-CuNb was made when h=200-50nm, shown as the dashed line. The indentation hardnesses of the single layer Cu, Nb, a-CuZr, and a-CuNb films are also shown. The peak hardness of Cu/a-CuZr approaches that of the a-CuZr; whereas the peak hardness of Cu/a-CuNb is much lower than that of the a-CuNb.

For comparison, the hardnesses of Cu/Nb [11] and Cu/a-CuZr [75] multilayers as a function of layer thickness are also shown in the same plot. Cu/Nb multilayers have the highest peak strength (~ 6.9 GPa) among the three multilayer systems, followed by a peak strength of 6.3 GPa in Cu/a-CuZr multilayers. It is noted that the peak hardness of Cu/Nb and Cu/a-CuZr approaches the hardness of single layer a-CuNb and a-CuZr respectively, while Cu/a-CuNb multilayer has a much lower peak hardness compared with the hardness of single layer a-CuNb.

Table 1. Measured modulus of single layer and multilayer thin films

	a-CuNb	Cu/a-CuNb 5nm	Cu/a-CuNb 20nm	Cu/a-CuNb 50nm	Cu/a-CuNb 100nm	Cu/a-CuNb 150nm	Cu
Modulus (GPa)	136±3	123±5	126±3	119±5	122±4	120±5	113±9

When 50 nm < h < 200 nm, the hardness of multilayers can be well fitted by a linear line, consistent with the Hall-Petch relation. The Hall-Petch slope can be described by using the following equation [11]

$$\text{Equation 27} \qquad k = \left(\frac{\tau^{*}\mu b}{\pi(1-v)}\right)^{0.5},$$

where τ^{*} is the C/A interface barrier strength for slip transmission, k can be obtained from the measured Hall-Petch slope for indentation hardness ($k=k_{\text{Hall-Petch}}/3.1/2.7$), μ is the shear modulus, *b* is the Burgers vector of the crystalline layer (Cu), and *v* is the Poisson's ratio. The measured Hall-Petch slope for Cu/a-CuNb from the hardness plot is 14.5 GPa $\sqrt{\text{nm}}$, thus k equals to 1.734 GPa $\sqrt{\text{nm}}$. By using μ = 48 GPa, *b* = 0.25 nm, and *v* = 0.3 for Cu, *the barrier strength is calculated to be 0.55 GPa, corresponding to a maximum hardness of 4.6 GPa, which agrees well with the measured peak hardness of Cu/a-CuNb multilayers.* Hardness and modulus were also measured by partial loading/unloading indentation, and the summary of reduced moduli of single layer and multilayer films were shown in Table 1. The reduced modulus of single layer a-CuNb, Cu/a-CuNb multilayers, and single layer Cu is ~136 GPa, 119-126 GPa, and 113 GPa, respectively.

III.5 Discussions

III.5.1 Evolution of microstructure with layer thickness

Cu/a-CuNb multilayers consist of alternating amorphous CuNb layers and nanocrystalline Cu layers were synthesized. Although the calculated Gibbs free energy vs. concentration diagram suggests that the a-CuNb phase could form in a wide window (if Cu concentration is between 35-80 at. % [127]), our studies show that the structure of a-CuNb could be tailored by changing the individual layer thickness of a-CuNb and Cu. When h equals 1 or 2.5 nm, the broad peaks can be decomposed into an amorphous peak (a-CuNb), a Cu (111) peak, and a middle peak with the d-spacing of ½ ($d_{a\text{-}CuNb}+d_{Cu(111)}$). The formation of middle peak implies the possible structural change of a-CuNb along interfaces in these very fine multilayers. The formation of the middle peak has been frequently observed in crystalline/crystalline metallic multilayers, such as Cu/V [125], Ag/Ni [128] and Fe/W [129] and such phenomena were ascribed to the interface constraint between the adjacent layers. The observation of this similar phenomenon in the current Cu/a-CuNb is somewhat unusual, because a-CuNb does not have a regular crystal lattice. Consequently one would not anticipate the prominent interfacial constraint between Cu and a-CuNb, which could affect the plasticity transfer between layers. The amorphous hump corresponds to the average nearest neighbor distance (NND) in the amorphous structure, and the formation of a middle peak in the Cu/a-CuNb thus may indicate a slight variation of NND in a-CuNb.

On the other hand, as shown in Fig. 24, interfacial MRO layers with semi-crystalline nature exist along the C/A interfaces. As there is no mutual solubility between Cu and Nb at room temperature (due to positive heat of mixing) [73], Cu (Nb) atoms may have the tendency to stay in extremely fine nanoclusters (< 1 nm) instead of the ideal random distribution of Cu and Nb atoms in typical amorphous metals. Atomic resolution STEM images may be needed in future studies to further confirm this hypothesis. While depositing the first few monolayers of a-CuNb on Cu layers, there is a tendency for Cu atoms in a-CuNb to segregate (into sub-nanometer clusters) due to the influence of underlying Cu layers. Such an arrangement could reduce the mismatch between NND of a-CuNb and Cu (reduce mismatch strain energy) and may consequently leads to the formation of MRO layers that lattice parameters equivalent to the average of a-CuNb and Cu (111) as evidenced by XRD and TEM-SAD studies. The formation of these MRO layers could lead to softening of a-CuNb in multilayers comparing to the single layer a-CuNb.

III.5.2 "Weak" strengthening effect in Cu/a-CuNb multilayers

The unusual size dependent variation of hardness for Cu/a-CuNb multilayers is intriguing compared with other C/A multilayers such as Cu/a-CuZr. Previous studies on several C/A multilayers show that the peak hardness of multilayer approaches the hardness of the single layer amorphous films [75, 91, 92]. For instance, the peak hardness of Cu/a-CuZr is similar to the hardness of single layer a-CuZr (Table 2). This is expected as the one would anticipate that the maximum hardness of C/A multilayers is ultimate determined the stress required to yield the single layer metallic glass. If the same hypothesis holds for other systems with C/A interfaces, then one would anticipate that the peak hardness of Cu/a-CuNb should be similar to that of a-CuNb, ~ 7 GPa. However the peak hardness for Cu/a-CuNb multilayer in our study is merely 4.5 GPa, much lower than the hardness of the single layer a-CuNb. In fact, as shown in Table 2, the rule-of-mixture hardness (H_{rom}) value, calculated as $H_{rom} = 1/2(H_{a\text{-}CuNb}+H_{Cu})$, is very close to the peak hardness of Cu/a-CuNb multilayers as shown in Fig. 26. Such a drastic difference between the current study and prior studies on C/A multilayers suggest unusual strengthening mechanism in Cu/a-CuNb multilayers. Notice in Table 1, the moduli of Cu/a-CuNb multilayers are similar to the rule-of-mixture modulus of single layer a-CuNb and Cu.

Table 2. Comparison of hardness of several Cu-based multilayer films

System	H-P slope ($\mathrm{GPa}\sqrt{\mathrm{nm}}$)	Measured peak hardness (GPa)	Calculated peak hardness from H-P slope (GPa)	Single layer film hardness (GPa)	ROM hardness (GPa)
Cu/Nb	2.1	6.9	6.8	H_{Nb}=2.7	2.2
Cu/a-CuZr	1.05	6.3	1.5	$H_{a\text{-}CuNb}$=6.2	3.9
Cu/a-CuNb	1.7	4.5	4.6	H^{SL}_{a-CuNb}=7.2	4.5
				H^{ML}_{a-CuNb}=4.5	3.2

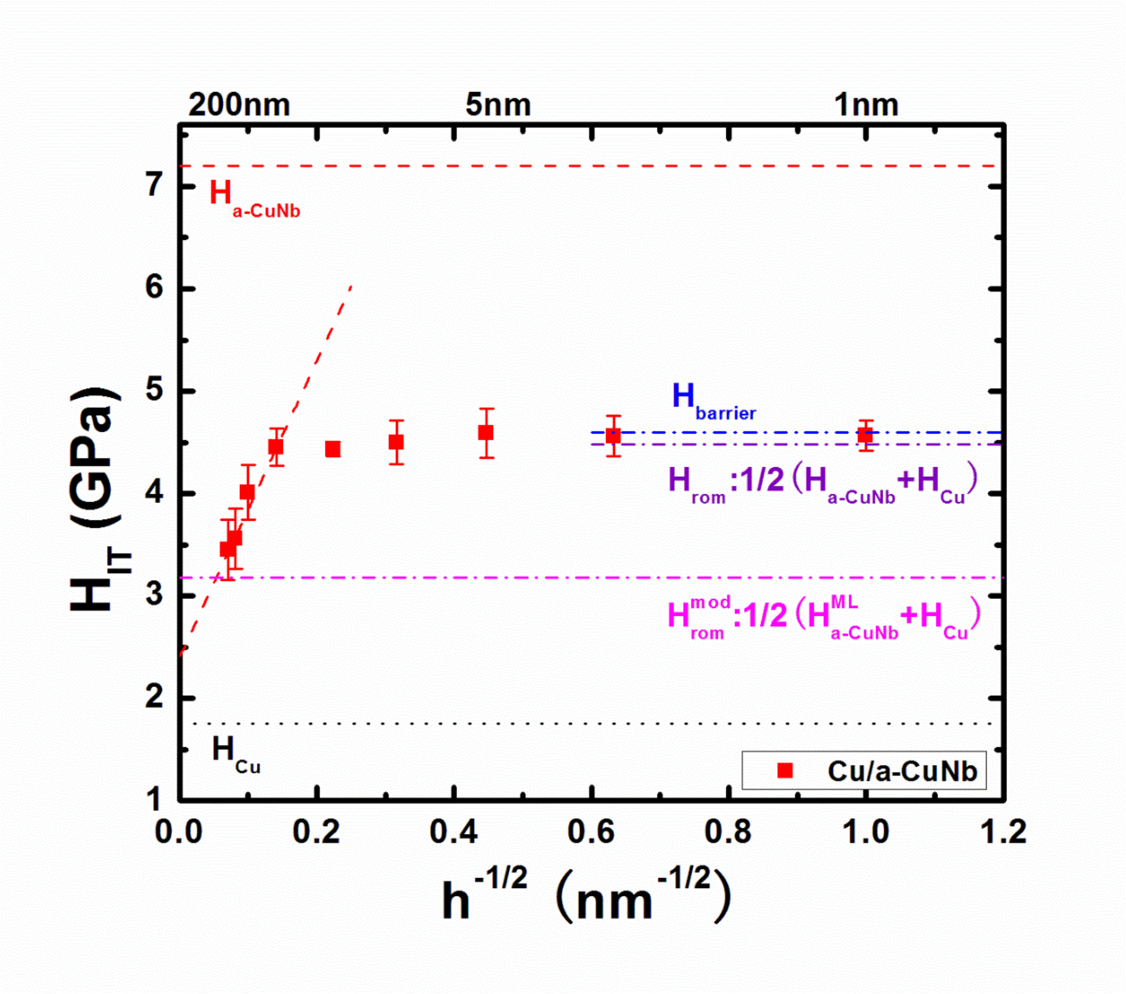

Figure 26. Evolution of indentation hardness (H_{IT}) of Cu/a-CuNb multilayers as a function of $h^{-1/2}$, where h is the individual layer thickness. A linear fit was made when h=200-50nm shown as the dashed line. The hardness for the single layer a-CuNb and Cu films were added as references. $H_{barrier}$ was converted by the interface barrier strength which was calculated by Hall-Petch slope. H_{rom} is the average of $H_{a\text{-}CuNb}$ and H_{Cu}, while H_{rom}^{mod} is the average of H_{a-CuNb}^{ML} and H_{Cu}.

We now examine the correlation between peak hardness and H-P slope of several multilayer systems, including Cu/Nb [11], Cu/a-CuZr [75], and Cu/a-CuNb. It has been established that using the Hall-Petch slope, one can estimate the peak hardness of multilayers by using equ. (1). As shown in Table 2, the calculated peak hardnesses of

Cu/Nb and Cu/a-CuNb both match well with the measured peak hardnesses. In contrast the hardness calculated from the H-P slope for Cu/a-CuZr is significantly lower than the measured peak hardness.

Since the H-P slope can correctly predict the peak hardness of Cu/a-CuNb multilayers, we hypothesize that the peak hardness of Cu/a-CuNb multilayers could be limited by the inherently low hardness of a-CuNb in multilayers, which is ~ 4.6 GPa, similar to the barrier strength predicated by H-P slope. The prediction that the hardness of a-CuNb layer in multilayers may be inherently lower than that of the single layer a-CuNb is somewhat surprising and will be discussed again in the next sections. Nonetheless if the assumption is correct, the modified ROM hardness, H_{rom}^{mod}, can be calculated as ½ (H_{a-CuNb}^{ML}+H_{Cu}) = 3.2 GPa, close to the lower bound hardness of Cu/a-CuNb multilayers at large h. Similar trend is observed in both Cu/Nb and Cu/a-CuZr multilayers as shown in Fig. 25 and Table 2.

According to the models proposed by Nix [130] and Misra [11], when the layer thickness of multilayers is small enough (tens of nm or so), the Hall-Petch relation cannot explain the size dependent strengthening well. Instead, the confined layer slip (CLS) model works much better for numerous crystalline metallic multilayers. In contrast to crystalline multilayers and Cu/a-CuZr multilayers, there is not a thickness range corresponding to the CLS strengthening mechanisms in the current Cu/a-CuNb multilayers, as when h = 50 nm, the strength of multilayers has already reached a plateau. CLS models cannot describe the hardness plateau observed in our study, indicating a "weak" strengthening effect from the Cu/a-CuNb layer interfaces.

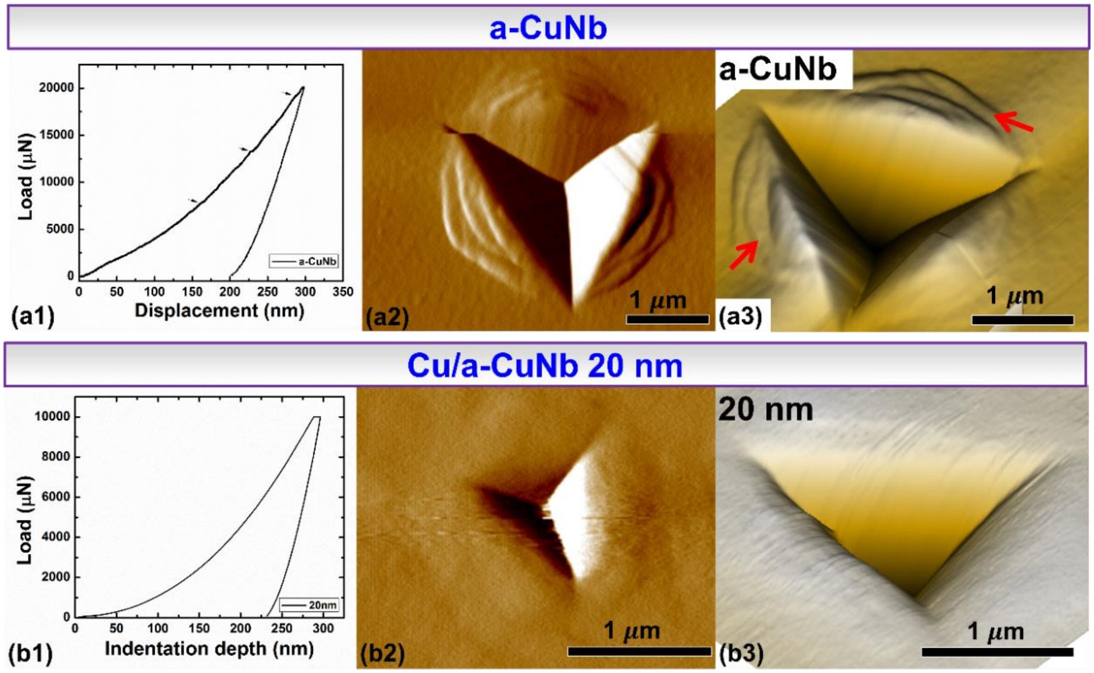

Figure 27. Load-displacement curves and images of surface morphology of indents after nanoindentation of single layer a-CuNb and Cu/a-CuNb 20 nm multilayers. (a1) and (b1) show the load-displacement curves of a-CuNb and Cu/a-CuNb 20nm multilayers respectively. Discrete pop-in events in the a-CuNb are indicated by arrows. (a2-b2) The SPM images of the indent morphology after indentation for a-CuNb (a2) and Cu/a-CuNb 20 nm multilayers (b2). (a3-b3) Comparisons of the 3D SPM images show prominent step-like pile-ups and shear bands (indicated by arrow) for the single layer a-CuNb (a3), as compared to the homogeneous deformation for the Cu/a-CuNb 20 nm multilayers.

The fundamental mechanisms that lead to such discrepancy between the current system and the Cu/a-CuZr system could be related to the formation of interfacial MRO layers in a-CuNb. Binary CuZr BMGs were successfully fabricated and studied because of the good glass forming ability [131, 132], in contrast the glass forming ability of CuNb system is not ideal. Bulk CuNb amorphous has been prepared by mechanical alloying or heavy cold-rolling, but the as-received CuNb is not completely amorphous [127, 133, 134] similar to the MRO a-CuNb layer observed at layer interface in our study. The formation of such an MRO interfacial layer equivalently reduces the thickness of amorphous layer which can be seen in the extensive HRTEMs of Cu/a-CuNb 2.5 nm. In Cu/a-CuNb multilayer, the interfacial MRO layer could prevent incoming lattice dislocations from smearing the stress/strain concentration at the interface, thus facilitating slip transmission into amorphous layers and weakening the barrier strength of amorphous layer. Therefore this interfacial MRO layer in a-CuNb could reduce the peak hardness of Cu/a-CuNb multilayers.

The H_{IT} of Cu/a-CuNb multilayers reaches a plateau at the peak value of 4.6 GPa, which is much lower than the hardness of single layer a-CuNb (~7 GPa). To address this "weak" strengthening effect, we examined plastic deformation modes of single layer amorphous and the multilayers with h of 50 nm or less. Fig. 27 shows load-displacement curves and surface morphologies of films after nanoindentation. Single layer a-CuNb shows a load-displacement curves with multiple pop-ins (a1), which matches well with the shear bands (local terrace-like pile-ups around the indent indicated by arrows) revealed by the SPM images in (a2 and a3); in contrast, the Cu/a-CuNb 20 nm multilayers have smooth load-displacement curves (b1), consistent with the homogeneous surface morphology (no clear step-like pile-ups) in (b2 and b3). The absence of step-wise pile-up after indenting to a greater depth is also confirmed for Cu/a-CuNb 5 nm multilayer. These studies show that the single layer a-CuNb (1μm) and Cu/a-CuNb multilayers (h<50nm) have different plastic deformation modes. The a-CuNb deforms inhomogeneously by forming shear bands, but the multilayers could deform homogeneously by formation of clusters of STZs. It should be noted that strain rate was kept similar during nanoindentation tests of all specimens in order to eliminate the influence of strain rate on deformation mode of amorphous metals [97, 100, 135]).

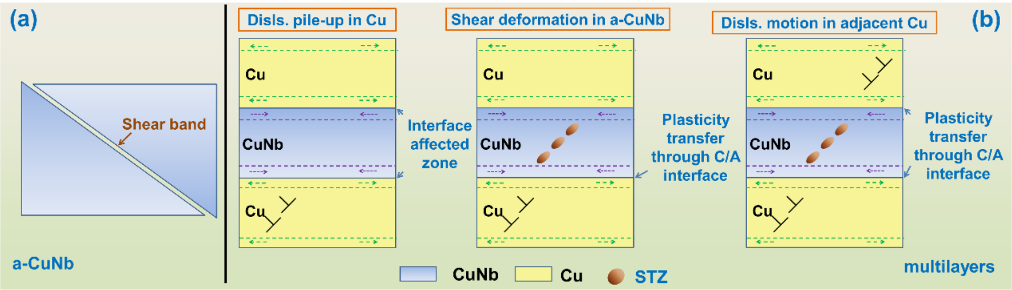

Figure 28. A schematic to illustrate the deformation mechanism in the Cu/a-CuNb multilayers. (a) Single layer a-CuNb deforms by shear banding. (b) In Cu/a-CuNb multilayers (h<50), deformation is dominated by dislocation pile-ups in Cu layers and the formation of STZs in a-CuNb layers. In the beginning, dislocations in Cu layer accommodate the plasticity; then through the crystalline/amorphous interface plasticity is transferred into a-CuNb layer in the form of shear events (motion of STZs); later, dislocations motion in the adjacent Cu is triggered by the shear events in a-CuNb through another crystalline/amorphous interface.

It has been shown [60] that the critical stress σ for shear band formation in amorphous alloys can be expressed as $\sigma = \sqrt{2^{3/2}\Gamma E/h}$, where Γ is the energy per unit area of shear band, E is the Young's modulus, and h is the height of the column (thickness of the film). This equation shows that the critical stress for shear band formation increases with the decrease of film thickness at a rate of $h^{-1/2}$. According to this formula, the critical stress for shear band formation in the 50 nm thick a-CuNb in the Cu/a-CuNb 50 nm multilayers is more than 7 GPa (using Γ = 10J/m^2 and E = 100 GPa), much larger than the stress for the formation of shear bands in 1 μm thick a-CuNb film (~1.7GPa). As the hardness of Cu/a-CuNb 50 nm multilayer is merely 4.5 GPa, the a-CuNb in the multilayers (when h<50 nm) may accommodate the plasticity by nucleation of numerous shear transformation zones (STZs), which requires a much lower stress and is an indication of more homogeneous deformation in amorphous metals. Similar softening phenomenon due to homogeneous deformation has been observed during nanoindentation studies of amorphous PdSi pillars with various diameters [60]. The average flow stress at 5% strain for homogeneous deformation of a-PdSi pillars is ~1.6 GPa for pillars with diameter of 400 nm or less, but above 2 GPa for inhomogeneous deformation of pillars with larger diameters [60].

The intriguing phenomenon that hardness of Cu/a-CuNb multilayers (h<50) reaches a plateau is closely tied to the microstructure of C/A interface and the dimension of h. As illustrated in Fig. 28, the interfacial a-CuNb with MRO leads to an interface affected zone, which may facilitate the transfer of plasticity from the soft Cu layers into the much stiffer a-CuNb layers at a lower stress (Fig. 27b). Also the reduction of h in multilayers promotes the transition of deformation mode in a-CuNb and thus reduces the barrier stress for transmission of plasticity across layer interfaces.

III.5.3 MD simulation studies of plastic deformation in Cu/a-CuNb multilayers

To understand the plastic deformation and strengthening mechanism of Cu/a-CuNb multilayers, we conducted a series of molecular dynamic simulations of Cu 5 nm/a-CuNb 2.5 nm multilayers under uniaxial compression at a temperature of 10 K. Empirical interatomic potentials for Cu and Nb and their cross-pair have been widely used in our previous studies [136-138]. The compression strain rate is 10^8/s. The simulation cell contains 5 bilayers as shown in Fig. 29a (See supplementary Video 1). The in-plane dimensions for Cu are 10.5 nm along the <112> direction and 11.5 nm along the <110> direction. Periodic boundary conditions are applied in all three directions. Dislocations are characterized using common neighbor analysis.

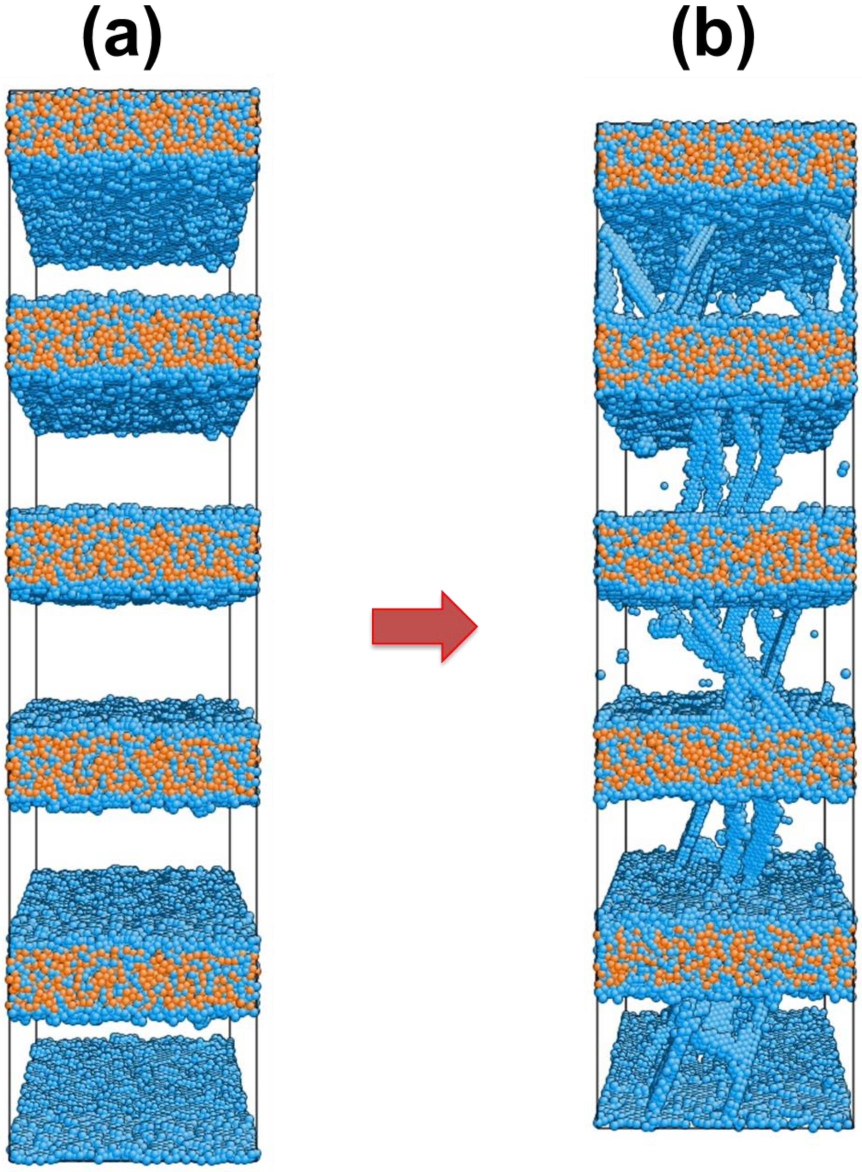

Figure 29. Atomic structures of Cu 5 nm / a-CuNb 2.5 nm multilayers, showing (a) initial structure before deformation, and (b) the deformed multilayers containing glide dislocations in Cu layers under uniaxial compression at a strain of 6.5%. Atoms are colored according their centro-symmetry parameter. Cu atoms are in blue and Nb atoms are in orange.

MD simulations demonstrated the transfer of plasticity across the Cu/a-CuNb layer interfaces. Plastic deformation commences in Cu layers via the nucleation and propagation of glide dislocations on {111} planes in Cu. As shown in Fig. 29b, plastic deformation in Cu layers is carried over by nucleation and glide of lattice dislocations of ½<110>{111}. During compression, abundant dislocations nucleate from layer interfaces, propagate within the Cu layer, and then deposit on the two interfaces that confine the layer. Previous studies show that during deformation of metallic multilayers, such as Cu/Nb, dislocations nucleated within the Cu or Nb layers will accumulate along layer interfaces [11, 136, 137] and the slip transmission of dislocations across layer interface will reduce the dislocation density at layer interfaces. Jia et al. [139] showed that formation of shear bands of the Cu/Nb (C/C) metal matrix composite is related to the co-deformation of heterophase alloy, triggered by the stress concentration at the interfaces. However, in the current study, we did not observe the accumulation of dislocations along the Cu/a-CuNb layer interface. Instead, the a-CuNb layers are locally sheared without the generation of shear bands. The shear deformation in a-CuNb effectively reduces the dislocation content arrived at the Cu/a-CuNb interfaces, in contrast to the reduction of dislocations at interface via slip transmission in crystalline metallic multilayers. Fig. 30 shows the evolution of atomic structures in a-CuNb layer in the Cu 5 nm/a-CuNb 2.5 nm multilayer before and after loading to a uniaxial compressive strain of 8.0%. The black dotted lines indicate the position of original layer interfaces, and the red dotted lines indicate the location of layer interfaces after 8% compression. Deformation distorted the sharp C/A layer interfaces. More importantly the plastic deformation induces prominent local shears as evidenced by high-density shear deformed regions (denoted by three ellipses) across the a-CuNb layer. MD simulations of the single layer a-CuNb (not shown here) suggest that the shear stress to nucleate a shear band is ~ 8 GPa under uniaxial compression, and deformation is dominated by a single shear band. In contrast, the shear stress to nuclear shear transformation regions (ellipses) in a-CuNb in the multilayer is ~ 4.8 GPa under uniaxial compression, indicating that the Cu/a-CuNb layer interfaces reduces the stress to nucleate shear deformation in a-CuNb, consistent with experimental studies that show the maximum strength of Cu/a-CuNb multilayers is less than the strength of single-layer a-CuNb.

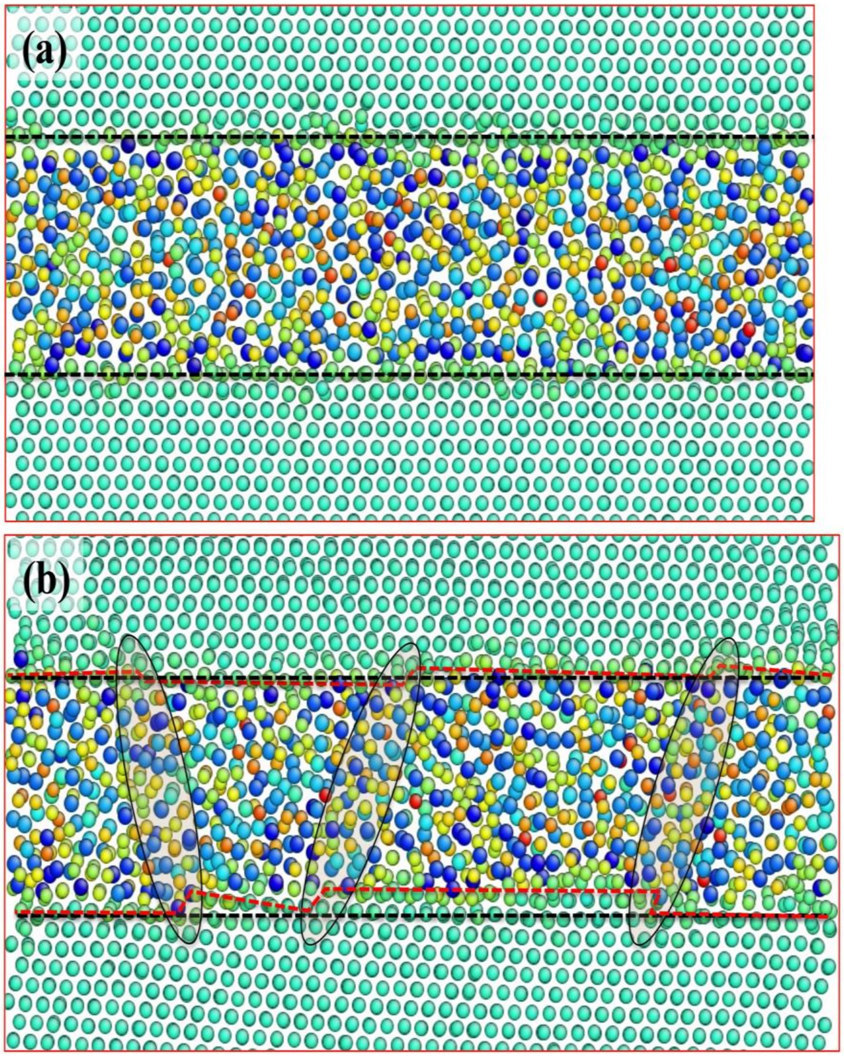

Figure 30. Atomic structures around one a-CuNb layer in Cu 5 nm/a-CuNb 2.5 nm multilayers, showing (a) undeformed structure and (b) the structure after uniaxial compressive strain of 8.0%. The black dotted lines indicate the original interfaces. The red dotted lines indicate the interfaces after 8% compressive strain. The local shears of atomic clusters across the a-CuNb layer are denoted by three ellipses. Atoms are colored according to their excess energy.

III.6 Conclusions

The microstructure and mechanical properties of Cu/a-CuNb multilayers have been systematically studied. When h $\leq$ 50 nm, the hardness of multilayers reaches a plateau value, which is much lower than the hardness of single-layer a-CuNb. Such a phenomenon is distinctly different from size dependent strengthening reported in Cu/a-CuZr multilayers. Microstructure analyses show that the a-CuNb at interfaces may have MRO that lowers the resistance to activate shear transformation zones in amorphous-CuNb layers. MD simulations suggest that the stress for the activation of STZs in the a-CuNb in multilayers is much less than the stress necessary to trigger shear bands in single-layer a-CuNb. This study provides a new perspective in tailoring the size dependent mechanical behavior of C/A multilayers with amorphous alloys that have positive heat of mixing.

CHAPTER IV

TAILORING PLASTICITY OF METALLIC GLASSES VIA INTERFACES IN CU/AMORPHOUS CUNB LAMINATES*

IV.1 Overview

Nanostructured crystalline/amorphous metallic multilayers have been increasingly studied due to their high strength and potential enhancement of plasticity in amorphous metals. Here we report on mechanical behaviors of Cu/amorphous CuNb multilayers that were prepared by magnetron sputtering with equal individual layer thickness (h) varying from 1 to 200 nm. A medium-range-order amorphous CuNb layer formed between Cu and amorphous CuNb layers. This intermediate layer facilitates transmission of plasticity from Cu to amorphous layers by preventing the smear of dislocation core on the interface. The maximum hardness of Cu/amorphous CuNb multilayers is achieved when $h \leq 50$ nm, and is much lower than the hardness of single-layer amorphous CuNb films. Molecular dynamics simulations show that, comparing with single-layer amorphous CuNb, the pile-up of dislocations in Cu layers lowered the stress for the activation of shear transformation zones in amorphous CuNb layers in multilayers.

---

* This chapter is reprinted from "Tailoring plasticity of metallic glasses via interfaces in Cu/amorphous CuNb laminates" by Z. Fan, Q. Li, J. Li, S. Xue, H. Wang, and X. Zhang, *J. Mater. Res.*, 1(2017), with permission of Cambridge University Press.

IV.2 Introduction

Metallic glasses (MGs) exhibit high yield strength, large elastic strain, and excellent wear resistance,[1-4] but they show limited plasticity and often fail catastrophically by forming shear bands especially under tension.[34, 37, 43] The incorporation of crystalline phases into MGs can hinder the propagation of shear bands and promote the formation and multiplication of shear bands, and thus increase the ductility of metallic glass composites (MGc).[7, 8, 64, 140, 141] The tensile ductility of ZrTi-based bulk metallic glass composites (BMGc) can exceed 10% strain by the introduction of soft crystalline dendrites.[62] The motif of adding ductile crystalline phases into MGs to enhance plasticity and ductility also works for thin film metallic glass composites (TFMGc).[74, 76, 77, 84, 91-93, 142] For instance, Cu 35nm/amorphous CuZr 5nm multilayer film can attain ~14% tensile ductility.[86] The constraint induced by crystalline phases on MGs can enhance plasticity of MGs under tension,[84, 86] compression,[92, 143] or bending,[93] but the effects of volume fraction of crystalline phase on fracture behaviors of MGs under tension are less well understood especially at nanoscale.

Meanwhile micropillar compression tests are proved to be a suitable method to study the deformation behaviors of MGs.[60, 83, 88, 90, 117, 144] For instance, pillar compression results show that the yield strength of MGs increases and the deformation mode changes from “highly localized” (shear band formation) to “homogeneous” with decreasing diameter of MGs.[60, 90, 145] Via *in situ* pillar compression technique, stress-strain behaviors can be directly correlated to deformation events during compression, permitting the exploration of underlying mechanisms behind deformation.

Investigation of fracture mode and fracture surface can reveal deformation and fracture mechanisms, and thus can help to design materials with improved plasticity and fracture toughness.[38, 44, 146-149] The fracture surface of MGs typically has single or sporadic shear bands, manifestation of brittle fracture, and plastic deformation is highly localized in a limited number of shear bands.[44, 51, 146] The rapid propagation of few shear bands dissipates little energy, and MGs only accommodate scant plasticity after yielding. There are some examples that show, however, by optimizing composition, some monolithic MG can sustain 160% true strain under compression;[56] and certain BMGc with second phases can have substantial plasticity and even fracture by necking under tension.[62] In these rare examples of ductile fractures of MGs or MGc, the fracture surface usually contains abundant intersecting shear bands, which delocalize strain and accommodate more plasticity.[56, 62] Bei et al. [69] showed that plastic strain of Zr-based BMG increases with increasing density of shear bands under compression. In contrast to featureless fracture surface of most MGs (cleavage-like brittle fracture), certain MGs contains high-density, tangled shear bands (both primary and secondary shear bands) and vein patterns (dimples), indicating greater fracture toughness and plasticity.[70, 150, 151]

In this study, numerous Cu/amorphous CuNb (referred to Cu/a-CuNb) multilayers on polyimide substrates were tested under tension. Considering the wide applications of crystalline films on compliant substrate such as electronic skin and paper-like displays,[152, 153] and potential usage of amorphous alloys in flexible electronics or as functional thin films,[154, 155] the study of amorphous films or crystalline/amorphous (**C/A**) multilayers on compliant substrates is worthy of investigations. Meanwhile *in situ* micropillar compression tests were performed to understand how crystalline phases can enhance the overall plasticity of MGc. To avoid the effect of sample size, the dimension of a-CuNb layer in single layer film and C/A multilayer is kept the same (2 μm). Our studies show that, by deliberately tailoring the individual layer thickness and architecture of the C/A multilayered thin films, fracture behaviors of C/A multilayers can be effectively tuned. In particular, under tension, fracture surface with dimples or river patterns can be achieved for MGs in multilayers by adjusting the volume fraction and layer thickness, in drastic contrast to featureless brittle fracture surface of single layer metallic glass films. *In situ* micropillar compression studies show that under the constraint of crystalline phases, MGs can deform substantially via shear delocalization.

IV.3 Experimental

Cu/a-CuNb multilayers were deposited by direct current magnetron sputtering on Silicon and polyimide (Dupont^{TM} Kapton, Type HN) substrates. The polyimide substrates (with 25.4 μm thickness) were pre-cut into dog-bone geometry with a dimension of 7 × 26 mm and a gauge area of 3 × 8 mm. The a-CuNb layer was co-sputtered with atomic percentage of Cu50%Nb50%. The sputter chamber was evacuated to a base pressure better than 1×10^{-7} Torr, and $1\text{-}3\times10^{-3}$ Torr Ar was used during deposition. Tensile tests were operated on a Shimadzu tensile tester (AGS-X series) at a strain rate 6×10^{-3} s^{-1} and special grips were used to avoid slippage of samples during testing. The load cell used in this study has a capacity of 1000 N with a precision of ± 0.5 N. The gauge length is measured as the cross-head distance, and the elongation is obtained from the cross-head displacement from the tensile tester. At least six samples were tested to ensure the repeatability of results. Micropillar compression tests were performed by Hysitron PI X 87R SEM PicoIndenter® at room temperature inside an FEI Quanta 3D FEG dual-beam Scanning Electron Microscope (SEM). For each sample, at least five pillars were compressed to ensure repeatability. *In situ* videos were recorded during compression tests. An FEI Tecnai G2 F20 microscope operated at 200 kV was employed to carry out transmission electron microscopy (TEM) experiments in order to study the microstructure. A Tescan LYRA-3 (Model GMH) focused ion beam (FIB) SEM was used to study the fracture surface of specimens. X-ray diffraction (XRD) patterns were acquired on a diffractometer (Empyrean 2, PANalytical, Almelo, NL).

IV.4 Results

IV.4.1 Microstructure characterization

Fig. 31a illustrates the architectures of as-deposited films: 1 and 2 μm thick single layer a-CuNb films were used as references (Fig. 31a1); 1 μm thick Cu was utilized to form two TFMGcs (Fig. 31a2): bilayer Cu1μm/a-CuNb1μm and trilayer Cu1μm/a-CuNb2μm/Cu1μm (50% volume fraction of amorphous CuNb phase); 100 nm thick Cu was utilized to form two TFMGcs (Fig. 31a3): Cu100nm/a-CuNb1μm/Cu100nm and Cu100nm/(a-CuNb300nm/Cu100nm)×2 (the total thickness of the two stacks was kept similar, ~ 1 μm). These specimens allow us to probe the influence of layer interface and dimension of a-CuNb on the plasticity of MGs.

A typical dog-bone specimen before and after tensile test was shown by the optical micrograph in Fig. 31b. XRD pattern shows the amorphous nature of single layer a-CuNb film (Fig. 31c). Cross-section SEM (XSEM) image of Cu1μm/a-CuNb2μm/Cu1μm (Fig. 31d) shows the designed structure and the columnar grains in Cu layer. XTEM micrograph of Cu100nm/(a-CuNb300nm/Cu100 nm)×2 (Fig. 31e) shows featureless a-CuNb and nanocrystalline Cu layers. The C/A interface is abrupt with little sign of intermixing. The selected area diffraction (SAD) pattern shows the amorphous halo from a-CuNb layers and diffraction dots from nanocrystalline grains in Cu layers.

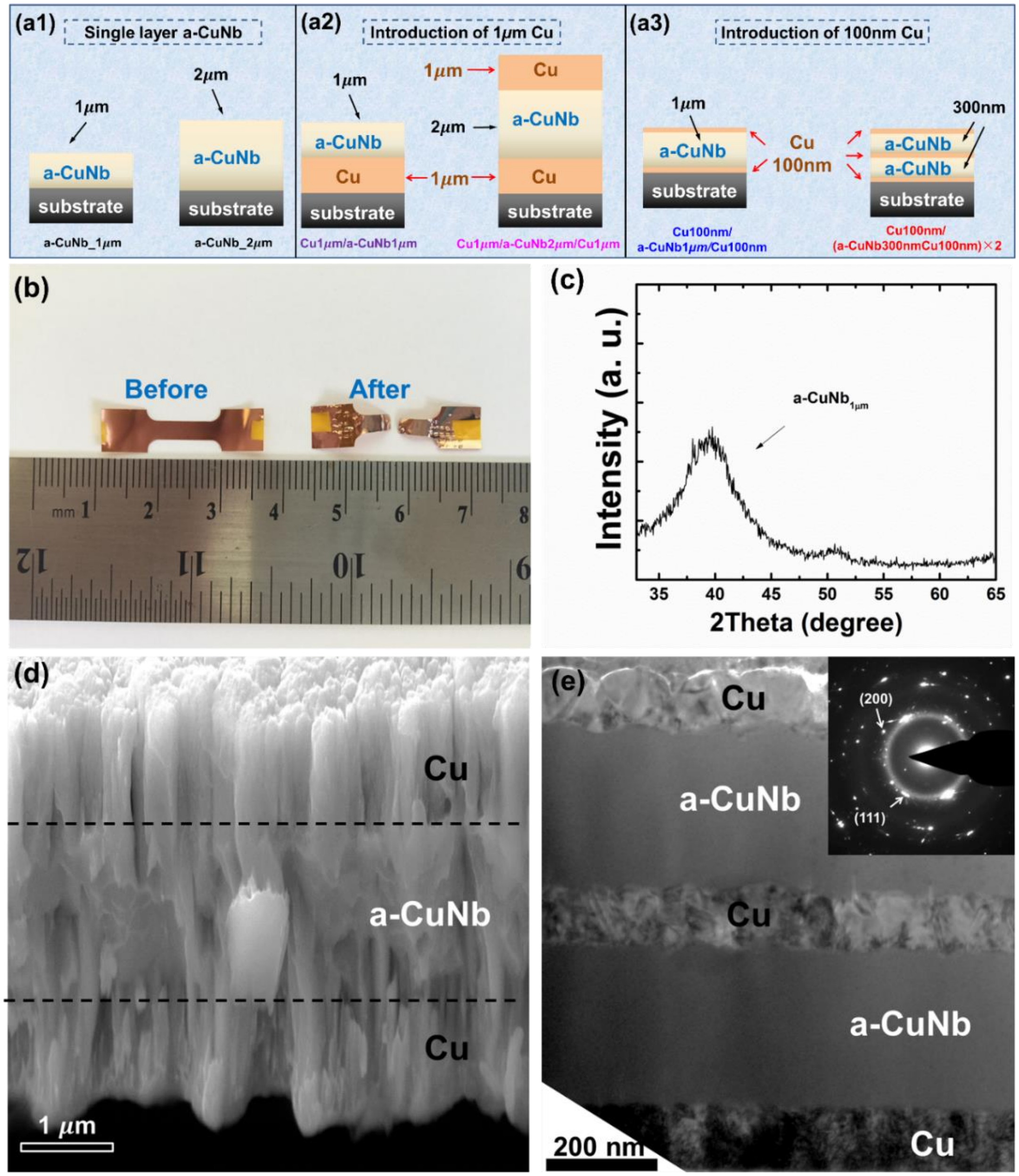

Figure 31. Experimental design and microstructure of the films. (a) A schematic showing the architecture of all the films. (a1) Single layer 1 μm and 2 μm a-CuNb films were deposited as references; (a2) Cu/a-CuNb multilayers with 1μm thick Cu; (a3) Cu/a-CuNb multilayers with 100 nm thick Cu layers. (b) An optical micrograph of Cu film on Kapton substrates before and after tensile test. (c) XRD profile shows the amorphous hump of single layer a-CuNb film. (d) An SEM image shows the microstructure of trilayer Cu1μm/a-CuNb2μm/Cu1μm. (e) A cross-section TEM image demonstrates the microstructure of 5 layer film: Cu100nm/(a-CuNb300nmCu100nm)×2.

IV.4.2 Fracture behaviors under tension tests

Engineering stress-strain curves of the films (Fig. 32) were obtained by subtracting the force of Kapton substrate ($F_{Kapton}(\varepsilon)$) from the applied force ($F_{total}(\varepsilon)$) on film-substrate composite using equation $\sigma(\varepsilon) = \frac{1}{hw}\left[F_{total}(\varepsilon) - F_{Kapton}(\varepsilon)\right]$, where h and w is the thickness and width of the film, respectively.[156, 157] Single layer a-CuNb has the greatest peak stress, 1165±42 MPa, and a critical strain (strain at peak stress) of ~2.3% similar to the elastic strain of typical MGs.[1] The peak stress of Cu1μm/a-CuNb2μmC/Cu1μm is 432±6 MPa similar to Cu1μm/a-CuNb1μm, 395±85 MPa, probably due to the similar volume fraction of amorphous phase (~50%) for both films. Despite the similar peak stress for both films, Cu1μm/a-CuNb2μm/Cu1μm has a much larger critical strain and the indication of this observation on fracture resistance will be discussed later. On the other hand, Cu100nm/a-CuNb1μm/Cu100nm with 83 % volume fraction (83 v.%) of amorphous phase has a peak stress of 855±66 MPa, smaller than that of Cu100nm/(a-CuNb300nm/Cu100 nm)×2 with 67 v.% of amorphous phase (955±109 MPa).

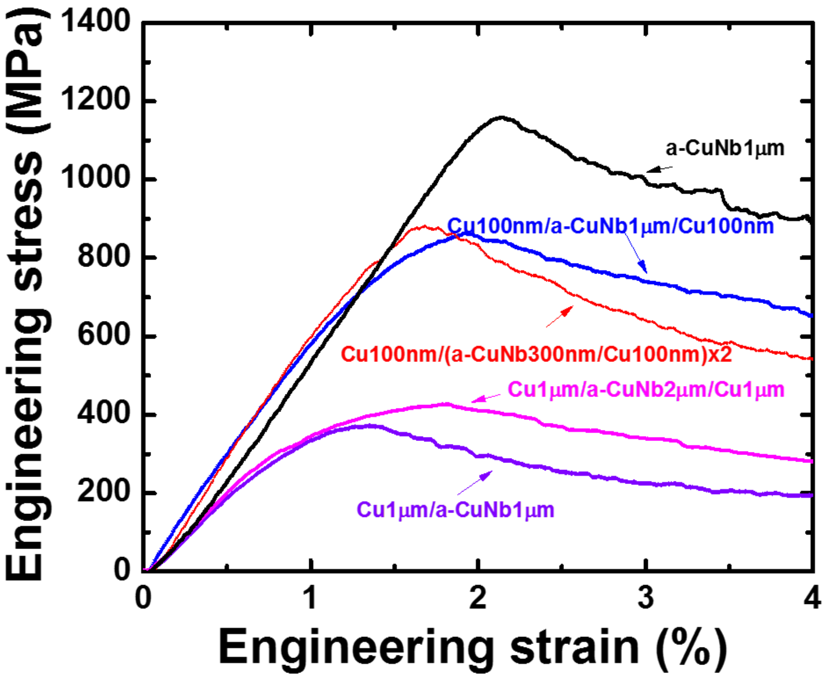

Figure 32. Engineering stress-strain curves of Cu/a-CuNb multilayers deposited on Kapton substrates. The stress-strain curve of single layer a-CuNb (1μm) was added as a reference.

Fracture surfaces of 1 and 2 μm thick single-layer a-CuNb films are shown in Fig. 33. Both films fracture along a smooth and straight path and leave a featureless crack surface with multiple shear bands identified.

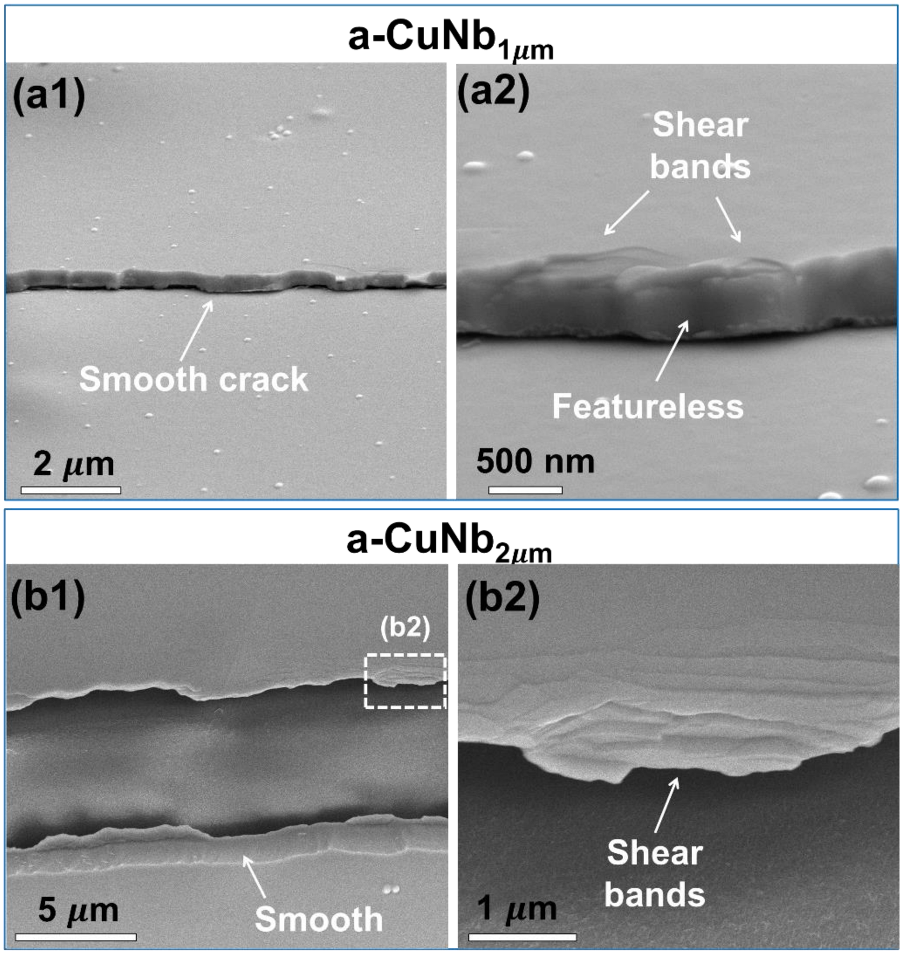

Figure 33. SEM micrographs comparing tensile fracture surfaces of single layer 1μm (a) and 2μm (b) a-CuNb films. (a1) An SEM image shows a representative smooth crack of 1μm thick a-CuNb. (a2) Higher magnification SEM image reveals the featureless fracture surface and shear bands. (b1) An SEM image shows the smooth fracture surface of 2μm thick a-CuNb. (b2) Higher magnification SEM image from the dashed box in (b1) reveals high-density shear bands.

The fracture morphology of the bilayer Cu1μm/a-CuNb1μm and trilayer Cu1μm/a-CuNb2μm/Cu1μm films is shown in Fig. 34. Compared to the single layer a-CuNb, the Cu1μm/a-CuNb1μm bilayer appears to have wavy (curved) fracture path and rough (columnar-like) fracture surface (Fig. 34a1). A representative micrograph of the fracture surface (Fig. 34a2) shows that the column sizes in a-CuNb are larger than those in Cu. In comparison, the Cu1μm/a-CuNb2μm/Cu1μm film fractures along a rough path with frequent turns, and the fracture surface of a-CuNb has mixed morphology (Fig. 34b). Fig. 34b1 and 3b2 show that a propagating crack perpendicular to the tensile direction was deflected to make turns before traveling perpendicular to the tensile direction again. More surprisingly, dimples and river patterns were frequently observed on the fracture surface of a-CuNb in this trilayer specimen (Fig. 34b3 and b4). It is unusual to observe nanoscale dimples/river patterns (average dimple dimension of ~106 nm) in 2 μm thick a-CuNb in the trilayer, in drastic contrast to the featureless fracture surface of 2 μm single layer a-CuNb.

Figure 34. Comparison of fracture surfaces between multilayers in which 1μm thick Cu layer was introduced. (a1) An SEM image shows a typical crack of bilayer Cu1μm/a-CuNb1μm film. Curved crack path was frequently observed. (a2) The higher magnification SEM image shows that both Cu and a-CuNb layers have columnar-like fracture surface, and Cu has a smaller columnar feature size. (b1) A representative SEM image shows a crack in the trilayer Cu1μm/a-CuNb2μm/Cu1μm and the crack frequently changes its path during propagation in a direction perpendicularly to the tensile direction. (b2) Higher magnification SEM image shows the coexistence of featureless and columnar-like surface for the trilayer system. (b3) An SEM image shows a region of the same specimen in which the fracture surface of a-CuNb layer is filled with dimples and river patterns. (b4) Higher magnification SEM image shows the nanoscale dimples in a-CuNb layer along its 2 μm thickness direction.

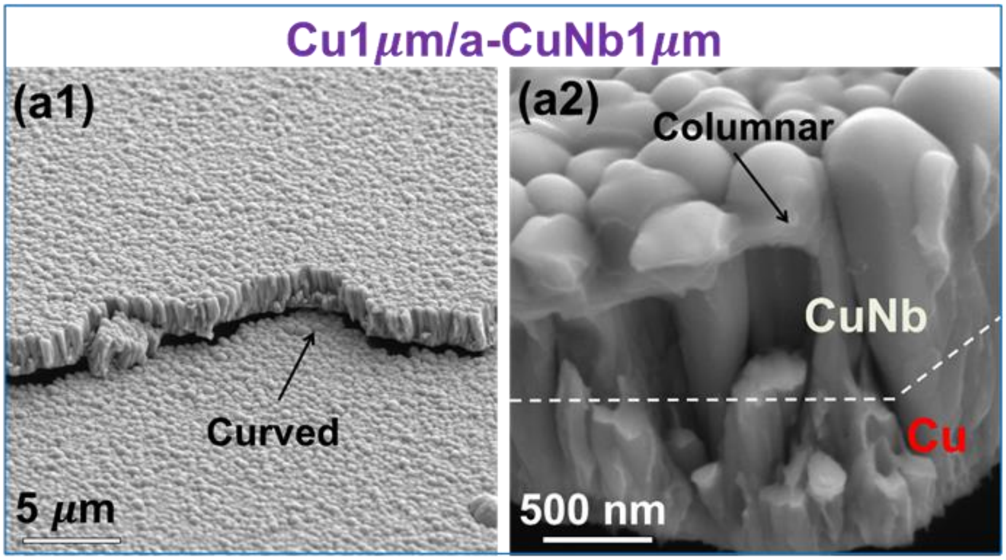
Cu1μm/a-CuNb1μm
(a1)
Curved
5 μm
(a2)
Columnar
CuNb
Cu
500 nm

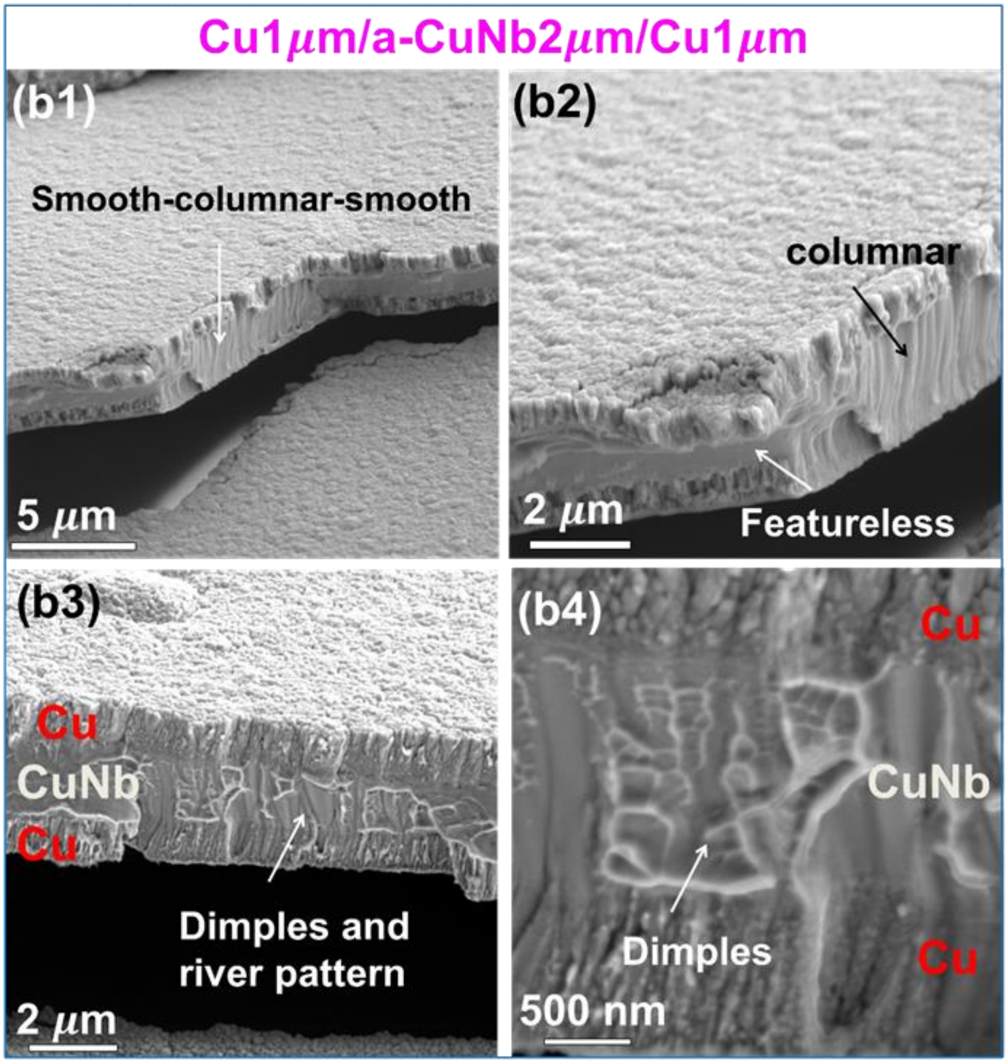
Cu1μm/a-CuNb2μm/Cu1μm
(b1)
Smooth-columnar-smooth
5 μm
(b2)
columnar
2 μm
Featureless
(b3)
Cu
CuNb
Cu
Dimples and
river pattern
2 μm
(b4)
Cu
CuNb
Dimples
Cu
500 nm

However, sandwiching 1μm thick a-CuNb with 100 nm Cu seems to help little with the plasticity in a-CuNb layer. The fracture surface of Cu100nm/a-CuNb1μm/Cu100 nm shown in Fig. 35a1 is featureless and contains clear shear bands. A higher magnification SEM image (Fig. 35a2) reveals that interface between Cu (top) and a-CuNb layers (middle) delaminates during the fracturing process. In comparison, the fracture surface of another multilayer (Fig. 35b1 and b2), Cu100nm/(a-CuNb300nm/Cu100 nm)×2 shows that the lower a-CuNb layer is full of ductile dimples and river patterns, despite the fact that the upper a-CuNb layer is filled with nanosized columns (without dimples). The average size of the dimples/river pattern is ~ 61±22 nm in 300 nm thick a-CuNb, much smaller than the dimples formed in a-CuNb in the Cu1μm/a-CuNb2μm/Cu1μm trilayer.

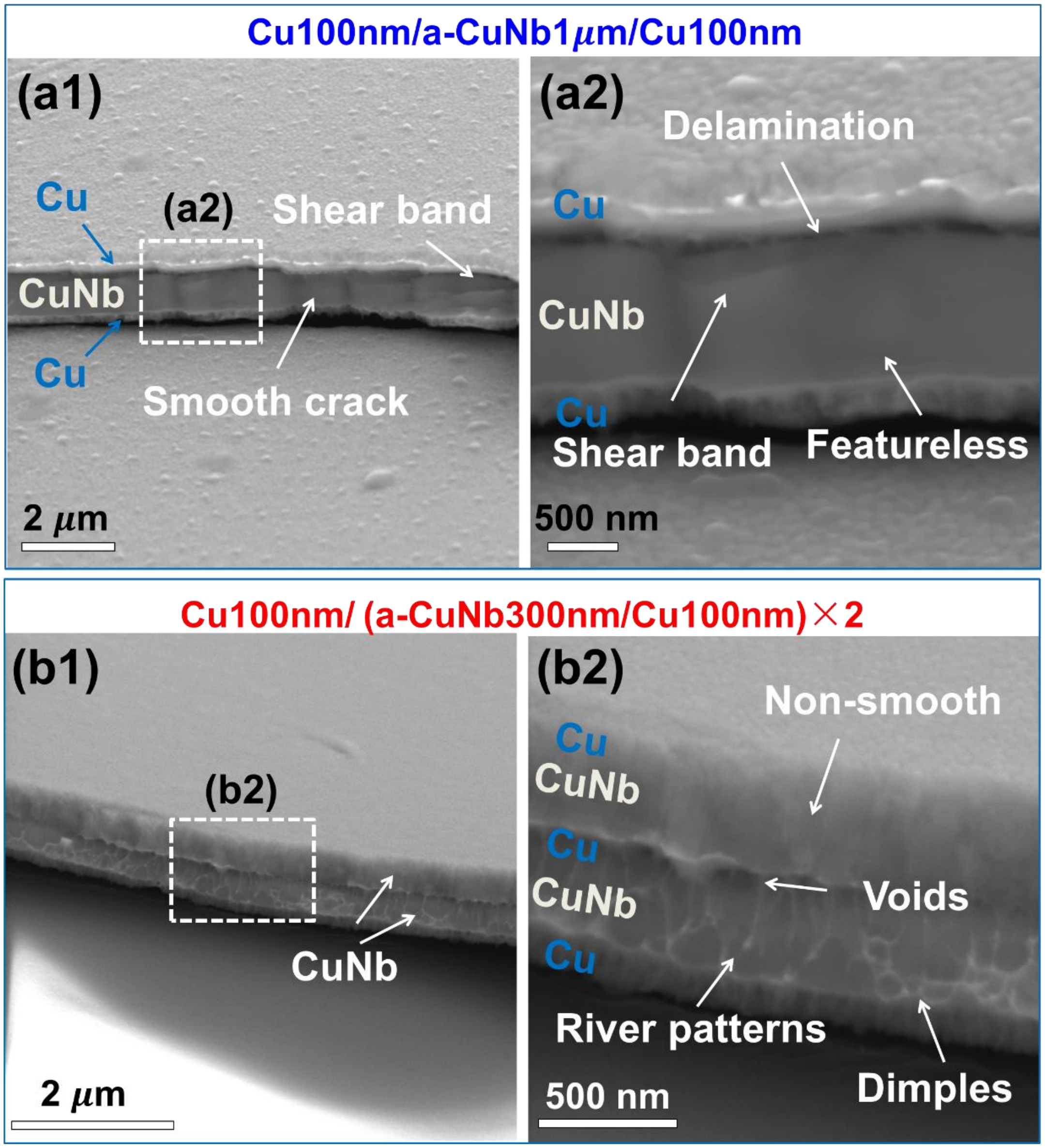

Figure 35. Comparison of fracture behaviors between multilayers in which 100 nm thick Cu layer was introduced. (a1) An SEM image shows the fracture surface of Cu100nm/a-CuNb1μm/Cu100nm film. (a2) High magnification SEM image of the dashed box in (a1) shows the featureless fracture surface of a-CuNb layer. Delamination between the top Cu and a-CuNb layers happened and a gap between them was observed. (b1) An SEM image shows the fracture surface in the tested Cu100nm/(a-CuNb300nmCu100nm)×2 film, different fracture surface for the upper and lower a-CuNb layers was seen. (b2) High magnification SEM image of the dashed box in (b1) shows that for the lower a-CuNb layer, the fracture surface contains river patterns or dimples, but the upper a-CuNb layer has a relatively smooth fracture surface. The middle Cu layer is filled with voids.

IV.4.3 Fracture behaviors under micropillar compression tests

The aspect ratio (height/diameter) of single layer 2 μm a-CuNb and Cu1μm/a-CuNb2μm/Cu1μm pillars is kept as 2:1 and the thickness for a-CuNb phase is 2 μm in both specimens. Representative true stress-strain curve along with *in situ* SEM snapshots acquired during compression tests of a single layer 2 μm a-CuNb are shown in Fig. 36. Four shear bands were observed during experiments and each of them corresponding to an individual load drop (marked as 1 to 4) is marked in Fig. 36a. A magnified stress-strain curve is shown in Fig. 36b. Right after the first load drop (point 1 on the stress-strain curve), the first shear band emerged (Fig. 36c), and then the second shear band (2) could be observed after another load drop (Fig. 36d). While these two existing shear bands were developing, a major shear band (3) formed after the third load drop. Soon after that, shear serrations became prominent, and shear bands developed quickly (Fig. 36e and 36f). The fourth shear band (4) corresponded with a major load drop seems to be connected to other shear bands, which went through the diameter of the pillar. All four shear bands can be clearly identified in Fig. 36g, and the SEM image of the pillar after being fully unloaded (Fig. 36h) shows the accumulated multiple shear bands.

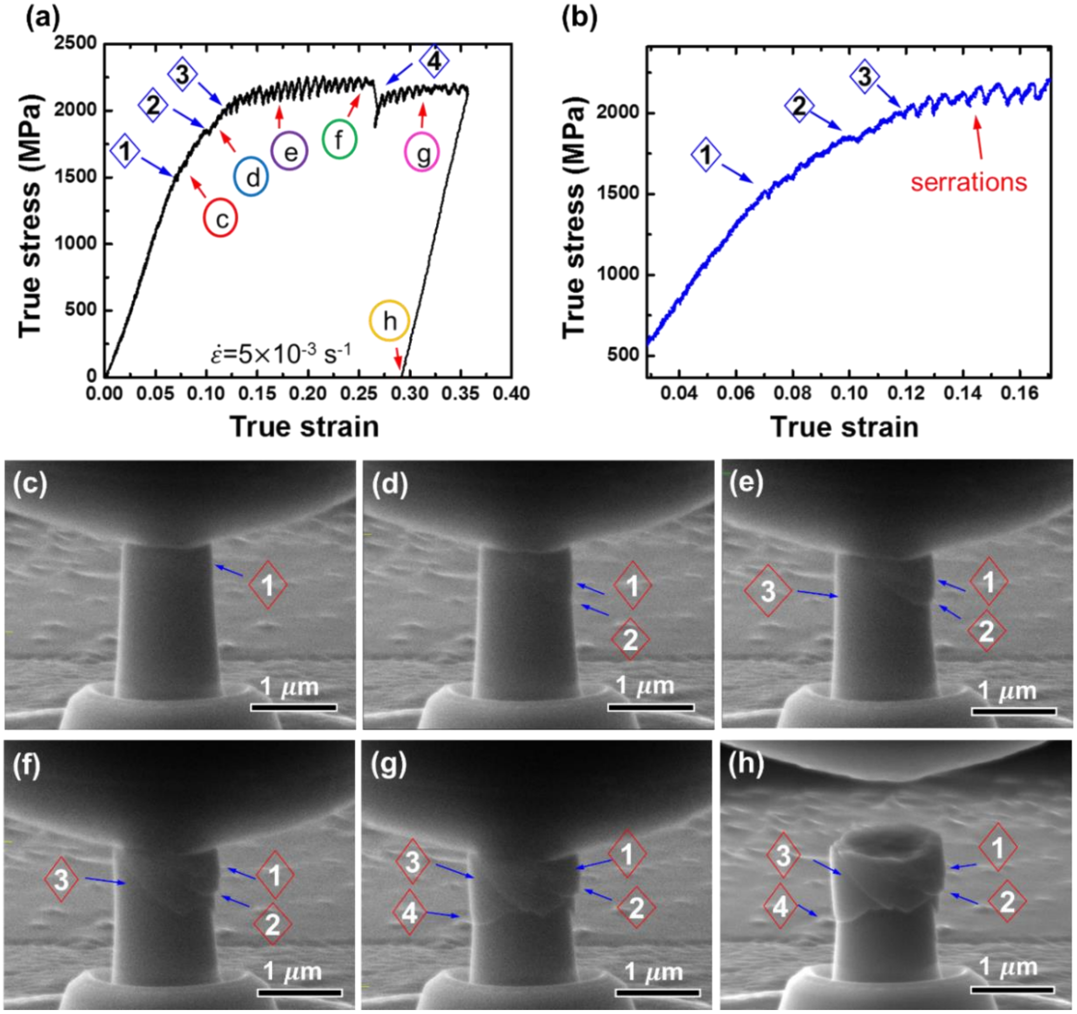

Figure 36. (a) True stress-strain curve of a single layer 2 μm a-CuNb film under compression obtained during *in situ* micropillar compression test in a scanning electron microscope. Four shear bands were identified during *in situ* compression test and correlated well with the pop-in events (marked as number from 1-4) on the stress-strain curve. (b) Magnified stress-strain curve shows the serrations associated with formation of shear bands. (c-h) SEM images (obtained from *in situ* tests) corresponding to point c-h in stress-strain curve were shown in (c-h) accordingly. Prominent shear bands were identified.

Representative engineering stress-strain curve and *in situ* SEM micrographs of Cu1μm/a-CuNb2μm/Cu1μm are shown in Fig. 37 (since the diameter change for different layer is drastically different, an engineering stress-strain curve instead of true stress-strain curve is used). After compressing up to the same engineering strain (50%), single layer a-CuNb pillar formed multiple shear bands and eventually failed through a major shear band; in contrast, a-CuNb layer in Cu1μm/a-CuNb2μm/Cu1μm pillar accommodated substantial plasticity through formation of multiple intersecting shear bands and remained deformable, and the two crystalline Cu layers were squeezed into a "pancake" morphology. The stress-strain curve and deformation behaviors of the trilayer are very different from the single layer a-CuNb. During compression test, the dominant deformation of the trilayer pillar went through four representative stages, correlated with the deformation of upper Cu layer (I), a-CuNb layer (II), lower Cu layer (III), and shear band formation (IV) (Fig. 37a). Shear band formation stage (IV) can be better illustrated in Fig. 37b, wherein prominent shear serrations can be observed. The upper Cu layer deformed and yielded at ~ 0.68 GPa (Fig. 37c, all the presented stresses for pillar compression are true stresses, which were not as the same as the stresses in Fig. 37 and were obtained by measuring the diameter of each layer from *in situ* SEM snapshots). Stress kept on increasing due to work hardening of the upper Cu layer, and meanwhile the upper Cu expanded substantially (Fig. 37d). During stage II, the stress increased at a higher rate up to 1.43 GPa (up to point e) and the width of a-CuNb slightly increased. After point e, the lower Cu layer started to deform and correspondingly the stress-strain curve dropped (stage III). Significant plastic deformation of the lower Cu layer occurred as shown in Fig. 37f and the stress increased again afterwards (Stage III). By ~ 1.8 GPa (30% engineering strain), serrations occurred (as shown in Fig. 37b). The SEM micrograph in Fig. 37g shows significant expansion of the lower Cu layer and slight dilation of the a-CuNb layer. A noticeable load drop was captured at point g presumably due to the formation a major shear band. Afterwards, a-CuNb deformed through formation of multiple shear bands manifested by the serrations in stress-strain curves (stage IV), and after fully unloaded at least three major shear bands can be seen as shown in Fig. 37h.

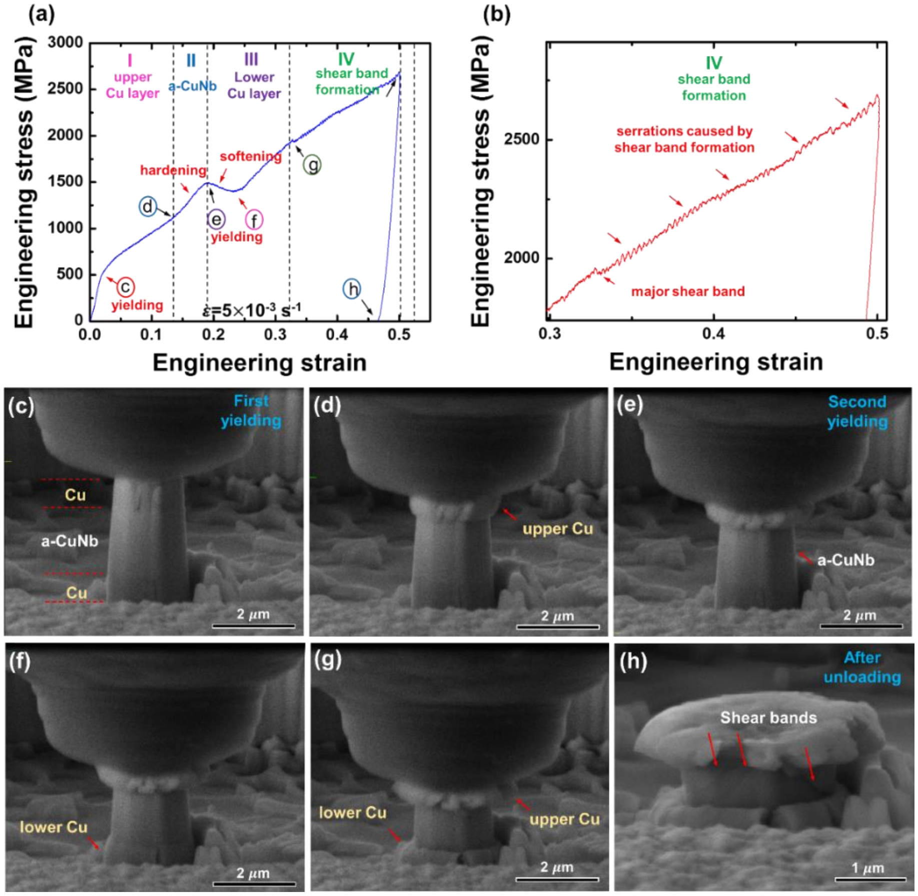

Figure 37. *In situ* micropillar compression studies on Cu1μm/a-CuNb2μm/Cu1μm trilayer. (a) Engineering stress-strain curve of the trilayer. The stress-strain curve can be divided into four stages: I - dominant deformation of the upper Cu layer; II – hardening due to increasing elastic deformation of a-CuNb layer; III – plastic deformation of the lower Cu layer; IV - shear band formations of the a-CuNb layer. (b) Magnified stress-strain curve of regime IV clearly shows the serrations caused by shear bands formations. (c-h) *In situ* SEM images corresponding to point c-h on the stress-strain curve. Prominent plastic deformation of the upper Cu layer is observed in (d). Plastic deformation of the lower Cu layer is observed in (f). Shear bands form in a-CuNb in (h). Obvious transition of dominant deformation at various stages can be identified.

IV.5 Discussions

IV.5.1 Tensile fracture behaviors of a-CuNb

The peak stress in the stress-strain curves (Fig. 32) indicates the formation of a major or sufficient number of small cracks so that the load necessary to sustain further deformation decreases with increasing strain. After reaching the peak stress, crack density (fragmentation perpendicular to the tensile direction) surges until reaches saturation. Single layer a-CuNb films deform through formation of sporadic/primary shear bands, leaving featureless fracture surface (Fig. 33) and forming parallel straight cracks (the direction of most cracks is orthogonal to the tensile loading axis). Through the introduction of 1μm Cu, the fracture path of Cu1μm/a-CuNb1μm bilayer becomes wavy (Fig. 34a). Moreover, the fracture surface of a-CuNb is filled with columns, which may dissipate more energy during fracture than the featureless smooth surface of tensile fractured single layer a-CuNb films. Prior studies show that MGs with 1-2 μm dimension typically experience inhomogeneous deformation by formation of few shear bands.[60, 61] Surprisingly, ductile dimples and river patterns are observed in Cu1μm/a-CuNb2μm/Cu1μm (Fig. 34b). The drastic change of fracture morphology (for a-CuNb) from featureless to column-like and eventually ductile dimples should arise from the constraint of Cu layers. Also sandwiching the a-CuNb with Cu on both sides (Cu1μm/a-CuNb2μm/Cu1μm) is more effective to increase the fracture resistance compared with Cu on one side only (Cu1μm/a-CuNb1μm bilayer), since shear step in amorphous layer can occur on the unconstraint side. Therefore, Cu1μm/a-CuNb2μm/Cu1μm has a greater critical strain than Cu1μm/a-CuNb1μm (Fig. 32), which should result from better fracture resistance of the trilayer.

The fracture morphology of two specimens, Cu100nm/a-CuNb1μm/Cu100nm and Cu100nm/(a-CuNb300nm/Cu100 nm)×2, is quite different. In Cu100nm/a-CuNb1μm/Cu100nm, the upper C/A interface shows decohesion after tensile test, and fracture surface of a-CuNb is featureless, similar to the fracture morphology of the single layer a-CuNb (Fig. 35a). This indicates that 100 nm thick Cu layer is insufficient to promote plasticity in a-CuNb in this multilayer. But the fracture surface of Cu100nm/(a-CuNb300nm/Cu100nm)×2 is drastically different. In particular both river patterns and dimples were observed in the lower a-CuNb layer (Fig. 35b). Hence, the volume fraction and the layer thickness of amorphous phase clearly impact its fracture behaviors. Similarly, Liu et al. [143] showed that, under compression, a critical thickness (volume fraction) of crystalline layer is needed to block the incipient shear bands. The ubiquitous formation of dimples/river patterns in the lower a-CuNb layer in Cu100nm/(a-CuNb300nm/Cu100 nm)×2 specimen indicates that more energy will be dissipated during the creation of dimpled/river patterns fracture surface. The very high density of dimples (or river patterns) demonstrates that instead of strain localization, the Cu100nm/(a-CuNb300nm/Cu100 nm)×2 film accommodates strain more homogeneously. These river patterns could be the results of connection of shear cracks (voids) inside the materials following large plastic shear deformation and during fracture, and may be the evidence of local necking.[38, 158]

Additionally it is intriguing to see that in the tensile tested Cu100nm/(a-CuNb300nm/Cu100 nm)×2 specimen, the lower a-CuNb layer has ductile dimples, but the upper a-CuNb has relatively smooth fracture surface (Fig. 35b). Although the fundamental mechanisms behind the different fracture morphology of the lower and upper a-CuNb are not fully understood, it is likely that the thick polyimide substrate assist the Cu layers to promote the plastic deformation in the lower a-CuNb layer. The polymer substrate may store a considerable amount of elastic energy and facilitate Cu to promote shear delocalization in the lower a-CuNb layer. In contrast, once the plasticity is transferred across the upper C/A interface into upper Cu layer, the 100 nm thick Cu does not have sufficient thickness to sustain plasticity, making it inefficient to constrain shear bands in the upper a-CuNb layer. The polymer substrate effect could also lead to the observed interface decohesion in the upper C/A interface for Cu100nm/a-CuNb1μm/Cu100nm (Fig. 35a), but not in the lower C/A interface. It should be mentioned that Xi et al. [70] and Wang et al. [159] showed that brittle MGs can also have nanoscale dimples or corrugations respectively on fracture surface. However, by comparing the featureless fracture surface of single layer a-CuNb film and fracture surface with dimples of various Cu/a-CuNb multilayers in this study, the enhancement of plasticity in a-CuNb layer due to the constraint of crystalline phase and effect of C/A interface is evident.

IV.5.2 Plasticity and fracture of multilayers under compression

Single layer a-CuNb film in this study can achieve ~ 34% true strain without failure, which is much larger than other monolithic amorphous films, such as a-CuZr.[88] The underlying reason could be related to the positive heat of mixing between Cu and

Nb,[73, 160] which will not be discussed in detail in this paper. *In situ* micropillar compression studies show that the single layer a-CuNb deform via forming few major primary shear bands. Serrations, indication of formation of shear bands, occur at a compressive stress of ~ 1.5 GPa (Fig. 36). However, as shown in Fig. 37, the 2 μm thick a-CuNb in Cu1μm/a-CuNb2μm/Cu1μm trilayer appears to be much more ductile. When the Cu layer deforms, high-density dislocations migrate towards the C/A interfaces, through which plasticity can be transferred into amorphous layer in a more homogeneous way, instead of localized deformation only through several shear bands in single layer a-CuNb film. The sheared regions in a-CuNb layer can reduce incoming dislocations accumulated at C/A interface and favor more homogeneous deformation.[160] The tendency of forming shear bands is also inhibited by the C/A interface since Cu layers can counteract the shear steps of a-CuNb by deforming elastically or plastically. As a result, shear instability in a-CuNb in the trilayer is suppressed in comparison to the single layer a-CuNb. Shear serrations in the single layer a-CuNb films occurred very early at a strain of ~ 7% and at a stress ~1.5 GPa. In contrast, serrations in trilayer started at ~ 30% strain and a stress of ~1.8 GPa. Also the average load drop associated with serrations is 13±4 MPa for trilayer, which is much smaller than 81±55 MPa for the single layer a-CuNb. When compressing up to ~65% true strain, single layer a-CuNb failed but the trilayer remained deformable. Clearly, the C/A laminates accommodate more plasticity with reduced shear instability, but without sacrificing strength, since the C/A trilayer shows similar flow stress compared with single layer a-CuNb. It should be mentioned that the decrease of serration amplitude is not a result of strain rate,[97, 98] since all the experiments were carried out at the same strain rate, 5×10^{-3} s^{-1}.

Another intriguing phenomenon observed from *in situ* pillar compression tests of trilayer is that the lower Cu layer deforms at a much larger strain and at a much higher stress. *In situ* compression tests show that the yield strength of the upper Cu layer is ~ 0.68 GPa, comparable to the measured hardness of 1μm thick Cu layer, ~ 1.8 GPa. Whereas the lower Cu layer deforms at a yield stress of ~ 1.27 GPa. Although the taper angle may affect the deformation of pillar to some extent in the very early stage of deformation, but the smaller tapering cannot satisfactorily explain why the lower Cu layer has a much greater yield strength. Geometrically necessary dislocations could play a role in this case,[161] since strain gradient could exist during compression. Another possible reason comes from the interface. While under compression, upper Cu layer is only partially confined by the C/A interface. However the lower Cu layer is confined by the C/A interface and interface between lower Cu and silicon substrate. A large (compressive) friction stress may develop along C/A interface, and significantly strengthen the lower Cu layer. As shown by the different yield strength of upper and lower Cu layers, the architecture of C/A nanolaminates can affect deformation behaviors. While utilizing TFMGcs in wear- or corrosion-resistant applications, the architecture of films should be considered.

It is also important to see that the simple trilayer experiences a prominent multi-stage deformation. Stage I is primarily related to the plastic deformation of the upper Cu layer and elastic deformation of a-CuNb. During stage II, the work hardening rate increases, presumably due to increasing load transfer to the more rigid a-CuNb layer. The reduction of flow stress in stage III is associated with plastic yielding of the lower Cu layers. As mentioned earlier the yield strength of the lower Cu layers increased significantly to ~1.27 GPa, which is remarkable for polycrystalline Cu. Stage IV experiences shear band formation in a-CuNb and plastic deformation of Cu. In this stage, deformation and strain hardening in crystalline layers compensate shear softening in amorphous layer, which resulted in a more stable fracture for trilayer.

IV.5.3 Effect of interface and size on plasticity of metallic glasses

As shown in this study and other studies, interface and size effects can substantially influence the plasticity of metallic glasses.[16, 60, 81, 162] Unless the size of MGs is under several hundred nanometers or smaller, MGs could not deform homogeneously without the formation of catastrophic shear bands.[60, 68, 163] Monolithic MGs with larger dimension would deform by shear band formation. In order to form shear band, a shear step needs to be generated by shear stress.[93] With the existence of ductile crystalline Cu layers, the shear steps in amorphous layers can be blocked by the crystalline layers through C/A interface. The C/A interface can play an important role in transferring plasticity between the two phases and trigger more homogeneous deformation in the amorphous phase.[16, 81, 162] Moreover, the different fracture behaviors between trilayer Cu1μm/a-CuNb2μm/Cu1μm and bilayer Cu1μm/a-CuNb1μm demonstrate that the constraint on amorphous layer by crystalline phase on both sides is necessary to enhance the plasticity and fracture resistance of a-CuNb, since shear steps can be formed on the unconstraint side. Once surface steps are created, the rapid propagation of shear bands along the steps cannot be contained. Interface decohesion and featureless fracture surface of the Cu100nm/a-CuNb1μm/Cu100nm film indicate that the volume fraction of crystalline phases needs to be sufficiently large to counteract the shear deformation in the amorphous phase. Reduction of dimension of amorphous phase can also effectively promote shear delocalization, as manifested by dimples (river patterns) on fracture surface.

IV.6 Conclusions

In this study, the fracture and plasticity of Cu/a-CuNb laminates are explored under both tension and compression. The incorporation of Cu can prominently promote shear delocalization in a-CuNb, which would normally have featureless brittle fracture surface. By tailoring the volume fraction of a-CuNb, the plasticity of a-CuNb can be enhanced further as shown by formation of river patterns/dimples under tension, and by substantial plasticity under compression. The Cu/a-CuNb interfaces not only promote plasticity in a-CuNb, but also significantly increase the flow stress of Cu to an unprecedented level.

CHAPTER V

LAYER THICKNESS DEPENDENT STRAIN RATE SENSITIVITY OF CU/AMORPHOUS CUNB MULTILAYERS[*]

V.1 Overview

Strain rate sensitivity of crystalline materials is closely related to dislocation activity. In the absence of dislocations, amorphous alloys are usually considered to be strain rate insensitive. However, the strain rate sensitivity of crystalline/amorphous composites is rarely studied, especially at nanoscale. In this study, we show that the strain rate sensitivity of Cu/amorphous CuNb multilayers is layer thickness dependent. At small layer thickness (below 50 nm), the multilayers demonstrate limited strain rate sensitivity; at relatively large layer thickness (above 100 nm), the strain rate sensitivity of multilayers is close to that of single layer Cu film. Mechanisms that lead to size dependent variation of strain rate sensitivity in these multilayers are discussed.

---

[*] This chapter is reprinted from “Layer thickness dependent strain rate sensitivity of Cu/amorphous CuNb multilayer” by Z. Fan, Y. Liu, S. Xue, R.M. Rahimi, D.F. Bahr, H. Wang, and X. Zhang, Volume 110, Issue 16, 161905 (2017), with permission of AIP Publishing.

V.2 Introduction

Metallic glasses (MGs) exhibit extraordinary mechanical properties, such as very high yield strength, large elastic limit, and outstanding wear resistance.[1-3, 5] But the formation and rapid propagation of shear bands often lead to catastrophic failure and very limited ductility.[37] Extensive efforts have been made to enhance the plasticity of MGs. Studies show that the deformation behaviors of MGs are size dependent and plasticity can be improved by reducing the size of MGs.[60, 61] Under compression, amorphous PdSi pillars with diameters under 400 nm deform homogeneously, but form shear bands in pillars with greater diameters.[60] Under tension, nanoscale Zr-based MG pillars fracture with necking in a ductile manner in contrast to the brittle fracture of the larger diameter pillars.[61] Adding crystalline phases into an amorphous matrix is another approach that can effectively enhance the ductility and toughness of MGs[7, 8, 62] by promoting the formation of profuse shear bands instead of highly localized shear bands and/or suppressing the propagation of shear bands. ZrTi-based bulk metallic glass composites (BMGc) containing crystalline phases show more than 10% tensile ductility while maintaining very high strength.[62]

One method that can precisely control the volume fraction and dimension of both crystalline and amorphous phases is to construct nanostructured crystalline/amorphous (C/A) multilayers.[74, 77, 81, 160, 164] Cu 35 nm/amorphous CuZr 5nm multilayers can achieve 14% tensile ductility.[86] The strength of Cu/amorphous CuZr multilayers can be tailored, via reducing individual layer thickness, to be greater than that of monolithic CuZr MG.[91] Donohue et al.[93] showed that under rolling and bending the shear band instability of amorphous layers is suppressed and amorphous layers co-deform with crystalline layers. The dimension of layers plays an important role on the mechanical behaviors of C/A multilayers. For instance, similar to crystalline/crystalline multilayers,[11-13] the hardness of C/A multilayers also increases with decreasing individual layer thickness (*h*).[91, 92, 106] Studies also suggest a transition of plastic deformation mode from pronounced shear banding to homogeneous deformation as layer thickness decreases.[83, 91, 92, 106] Crystalline layers can accommodate plasticity by dislocation movements, constrain propagation of shear bands, and enable co-deformation of the C/A multilayers.

The strain rate dependent deformation behaviors of MGs have also been investigated by measuring their strain rate sensitivity (SRS, *m*). SRS not only measures the flow stress sensitivity to strain rate and but also indicates the deformation mechanism of the materials. For face-centered cubic (fcc) metals, such as Cu and Ni, SRS increases with decreasing grain size (when grain size is under several hundred nm) or decreasing twin spacing.[95, 96, 165-167] Although strain rate changes the deformation behaviors of MGs, due to the absence of dislocations strain rate typically has little effect on the hardness or yield strength of MGs.[97, 168] However, both positive[101-103] and negative[104, 105] SRS were reported for MGs.

Although there are numerous studies on size dependent strengthening of C/A multilayers, the SRS of C/A multilayers is rarely studied.[106] Here, by comparing the indentation hardness of Cu/amorphous CuNb (Cu/a-CuNb) multilayers with *h* ranging from 5 nm-150 nm at various strain rates, we show that layer thickness has prominent influence on SRS of the composites. The mechanisms for size dependent variation of SRS in C/A multilayers and the implication of SRS on plasticity of MGc are discussed.

V.3 Experimental

Cu/a-CuNb multilayers with *h* varying from 5 to 150 nm were deposited on Si substrates by DC (direct current) magnetron sputtering. The a-CuNb (also served as cap layer) was deposited by co-sputtering Cu and Nb (Cu 50 at.%-Nb 50 at.%). Total film thickness for Cu/a-CuNb ranges from 1 to 2.4 μm. 1 μm thick single layer Cu and a-CuNb films were also deposited as references. Nanoindentation tests were performed by using a Hysitron TI950 TriboIndenter with a Berkovich indenter under CMX mode to continuously measure stiffness. For each sample, the maximum indentation depth was limited to 15% of the total film thickness. At least 10 indentation tests were performed on each sample at constant indentation strain rates of 0.01, 0.05, and 0.2 s^{-1}. An FEI Tecnai G2 F20 microscope operated at 20 kV was employed to study the microstructure of the films.

V.4 Results and discussions

Cross-section TEM images of Cu/a-CuNb 50 (Fig. 38a) and 100 nm (Fig. 38b) specimens show that a-CuNb layers are featureless and Cu layers contain nanoscale columnar grains. Selected area diffraction (SAD) patterns (insets) show diffuse diffraction ring (halo) from a-CuNb and diffraction dots from polycrystalline Cu. The average grain size (*d*) is ~ 47 and 94 nm for Cu/a-CuNb 50 and 100 nm multilayers, respectively (Fig. 38c-d). When h >20 nm, d is comparable to h, but d is larger than h when h < 20 nm. Stacking faults and twins are frequently observed in Cu grains.

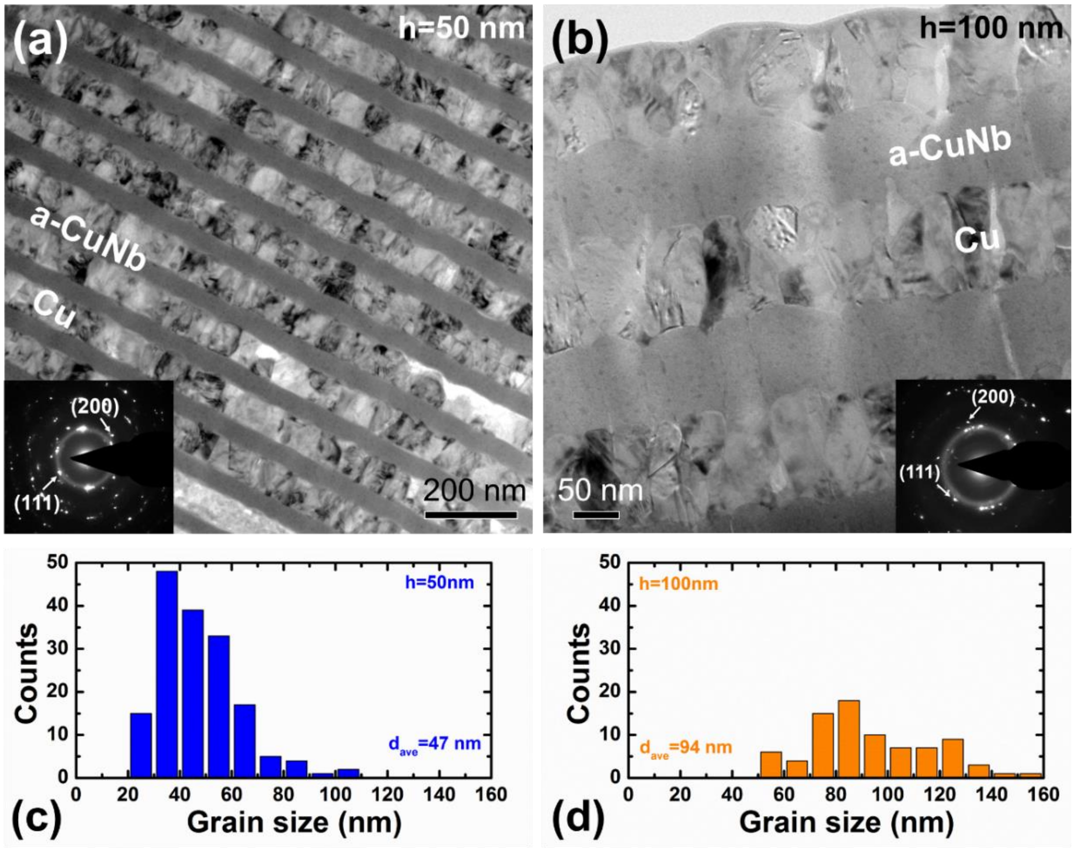

Figure 38. Cross-section TEM micrographs of (a) Cu/a-CuNb 50 nm and (b) Cu/a-CuNb 100 nm multilayers show featureless amorphous layers and Cu layers with columnar grains. SAD patterns (insets) show amorphous halo from a-CuNb, and (111) and (200) diffraction dots from Cu layers. (c-d) Statistics of grain size distributions show that the average grain size for Cu/a-CuNb 50 nm and 100 nm is ~ 47 nm and 94 nm, respectively.

During indentation tests at low strain rates, thermal drift is a major concern and may lead to significant variation. Flow chart in Fig. 39 depicts how to obtain accurate and consistent hardness at low strain rate with a modified method developed recently.[169] Like the conventional method, the modified method is also based on the fundamental relationship between E_r (reduced modulus), A (contact area), and S (stiffness).[115, 170, 171] The key difference lies in how to accurately calculate A. The conventional method calculates E and H based on measured h, P (Load), and S. At low strain rates, as thermal drift is substantial, the measurement of h may be unreliable. In comparison, the modified method measures P and S, and uses E_r measured at high strain rate to calculate A and h. Such a simple method significantly reduces the error associated with inaccurate measurement of h during low strain rate nanoindentation. Page et al.[172] showed that for given E_r and $\frac{P}{S^2}$, the "continuous stiffness" method directly provides H, which can be expressed as: $H = \frac{P}{S^2} \cdot \frac{4E_r^2}{\pi}$. Here $\frac{P}{S^2}$ is a material property and irrelevant to the shape of indenter tip, but would vary at various indentation depths.[169, 172, 173] In our study, $\frac{P}{S^2}$ would change with the change of strain rate.

Fig. 39a-c compares the results of hardness vs. indentation depth for the single layer a-CuNb film measured at various strain rates using conventional and modified methods. E_r used for modification is 136 GPa which is measured from both single indentations and indentations at high strain rate. At relatively high strain rates (0.05-0.2 s^{-1}), both methods lead to similar results (Fig. 39b-c). But at low strain rate (0.01 s^{-1}), the modified method yields more converged and consistent data (Fig. 39a).

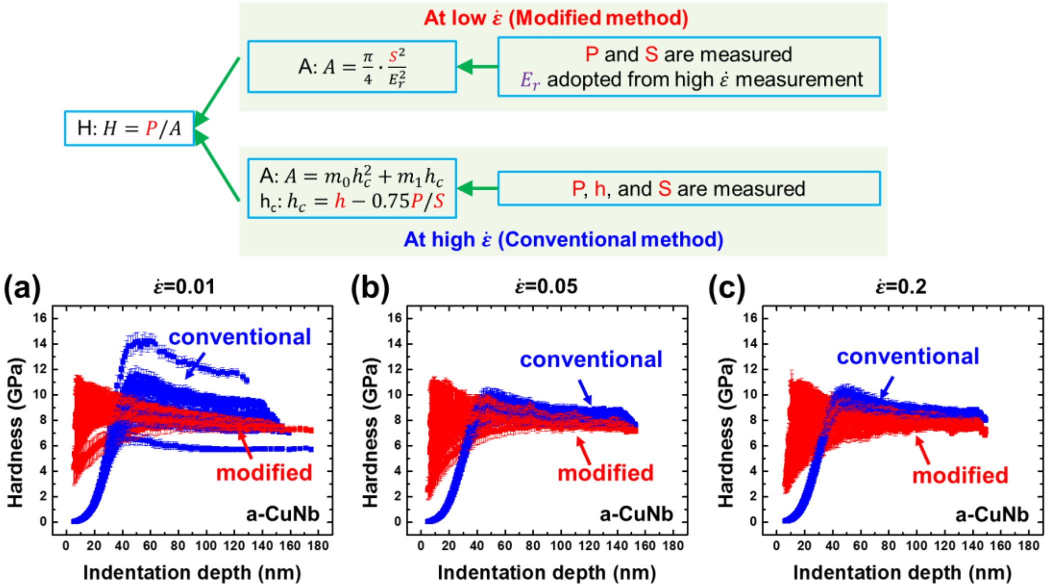

Figure 39. Flow chart illustrates the differences between conventional method and modified method to calculate indentation hardness. In the conventional method, *P*, *h*, and *S* are measured. In contrast, the modified method only measure *P* and *S*, but calculate *A* and *h*. Hardness vs. indentation depth of single layer a-CuNb at strain rates of 0.01, 0.05, and 0.2 s^{-1} was shown in (a), (b), and (c) respectively. The modified method (red) and conventional method (blue) demonstrate similar results at high strain rate, but the modified method show consistent and converged data at low strain rate.

Hardness with respect to strain rate for all the tested films are shown in Fig. 40a and 40b. Strain rate has little effect on the hardness of single layer a-CuNb film. But the hardness of Cu film clearly increases with increasing strain rate (Fig. 40a). Meanwhile, the hardnesses of Cu/a-CuNb multilayers with *h* of 5-50 nm show little strain rate dependence (Fig. 40a). In comparison, the hardness of Cu/a-CuNb 100 and 150 nm films increases prominently with increasing strain rate, as indicated by the positive slope (Fig. 40b).

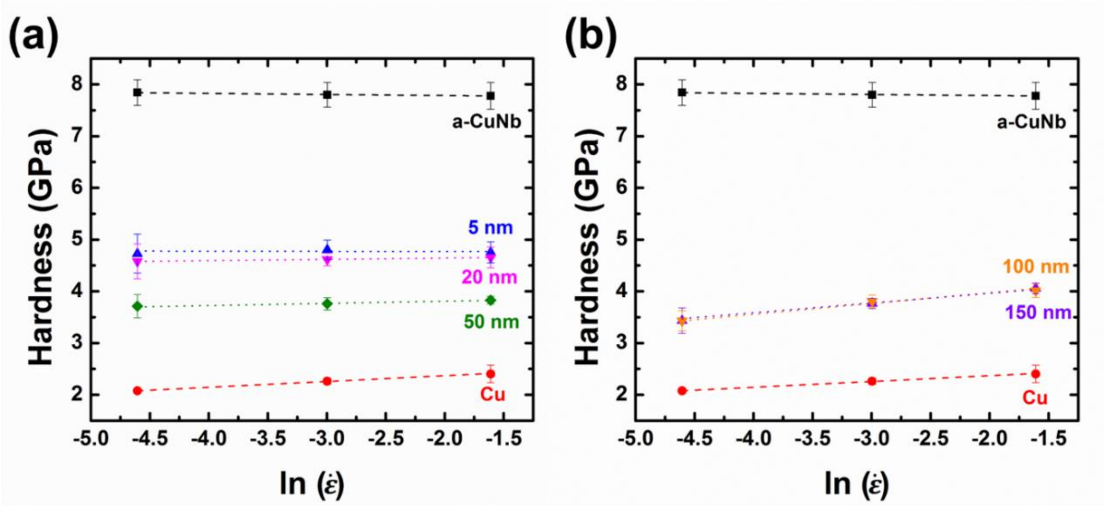

Figure 40. (a) With the increase of strain rate, the hardness of Cu/a-CuNb 5 nm, 20 nm, and 50 nm multilayers shows little increase. (b) With the increase of strain rate, the hardness of Cu/a-CuNb 100 nm and 150 nm multilayers increases monotonically. Data of single layer a-CuNb and Cu were also added as references.

The evolution of SRS with respect to individual layer thickness is shown in Fig. 41a. The SRS of the Cu film is 0.05. The Cu film has polycrystalline grains, with grain size comparable to that of Cu/a-CuNb 100 and 150 nm multilayers, as confirmed by TEM results (not shown here). The m of single layer a-CuNb layer is -0.0027. For Cu/a-CuNb multilayers, when $h \leq 50$ nm, smaller h results in a smaller m value approaching that of a-CuNb. But when $h \geq 100$ nm, m is ~ 0.05, nearly identical to that of Cu. Activation volume of Cu/a-CuNb multilayers decreases from $136b^3$ to $6b^3$ when h increases from 5 to 100 nm as shown in Fig. 41b (b is magnitude of the Burgers vector of dislocations in Cu, 0.255 nm) and it is ~$11b^3$ for the single layer Cu film. The activation volume in this study is consistent with literature data and falls in the lower boundary.[95, 166, 174]

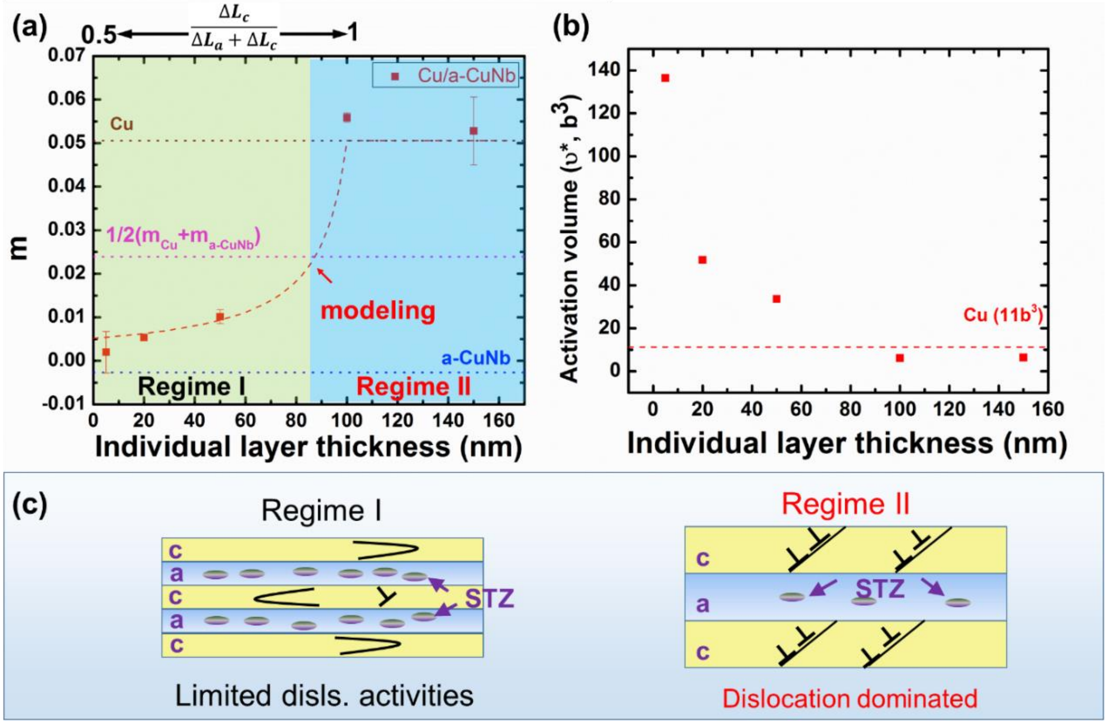

Figure 41. (a) Strain rate sensitivity (*m*) as a function of individual layer thickness (*h*) of Cu/a-CuNb multilayers. *m* of a-CuNb, Cu, and their average value were added as dotted lines. When $h < 50$ nm, *m* of Cu/a-CuNb multilayers decreases with decreasing *h*. When $h > 100$ nm, Cu/a-CuNb multilayers has apparent strain rate sensitivity value similar to single layer Cu film. The modeled curve (dashed line) is calculated from Equ. 33. (b) The activation volume of Cu/a-CuNb multilayers as a function of *h*. Activation volume for single layer Cu films is $11b^3$, which is shown as the dashed line. (c) A schematic shows the different deformation mechanisms at different *h*. When *h* is very small (<50 nm), dislocation activities are limited and crystalline and amorphous layers can co-deform; when *h* is relatively large (>100 nm), deformation is dominated by dislocation activities, and crystalline layers accommodate more strain than amorphous layers.

Systematic indentation experiments at various strain rates clearly show that strain rate has different influences on hardness of single a-CuNb, Cu, and Cu/a-CuNb multilayers. The negative *m* value for a-CuNb may result from deformation-induced devitrification,[106, 107] which causes local temperature rise. At higher strain rate, local temperature rise could not be conducted right away, causing a local decrease of viscosity and lower hardness. But the size dependent evolution of *m* for multilayers warrants further investigation.

For FCC metals with ultrafine grains or nanograins, SRS can be expressed by[95],

Equation 28 $$m = \frac{kT}{\xi b} \cdot \frac{1}{\chi\left(\alpha\mu b\sqrt{\rho}d + \beta\sqrt{d}\right)},$$

where *k* is the Boltzmann constant, *T* is the absolute temperature, ξ is the distance swept out by the glide dislocation during one activation event, μ is the shear modulus, α, β, χ are proportionality factors, p is dislocation density, and *d* is grain size. This equation suggests that for nanocrystalline Cu, SRS should increase with decreasing grain size.

We now consider the size dependent variation of *m* for multilayers. As amorphous layers are usually much harder than crystalline layers, during deformation the plastic strain accommodated by the crystalline and amorphous layers could be very different. Consider that the deformation of C/A multilayers is under iso-stress condition (similar to compressing micropillars made from C/A multilayers with flat punch). The *m* of C/A multilayers can be shown as,

Equation 29 $$\frac{1}{m} = \frac{\partial ln\dot{\varepsilon}}{\partial ln\sigma} \text{ (or } m = \frac{\partial ln\sigma}{\partial ln\dot{\varepsilon}}\text{)},$$

where σ is the flow stress and $\dot{\varepsilon}$ is the strain rate. Considering that crystalline and amorphous layers have equal individual layer thickness in this study, the total strain of C/A multilayers under iso-stress condition is,

Equation 30 $$\varepsilon = \frac{1}{2}(\varepsilon_a + \varepsilon_c),$$

where total strain, ε, is the displacement divided by the total film thickness $\Delta L/L$. ε_a (the strain of amorphous phase), and ε_c (the strain of crystalline phase), is $\frac{\Delta L_a}{L/2}$ and $\frac{\Delta L_c}{L/2}$, respectively. ΔL_a and ΔL_c are the displacement of crystalline and amorphous phase individually, and $\Delta L = \Delta L_a + \Delta L_c$. Therefore, the total strain rate of C/A multilayers can be obtained as follows,

$$\text{Equation 31} \qquad \dot{\varepsilon} = \frac{1}{2}(\dot{\varepsilon}_a + \dot{\varepsilon}_c).$$

From equation (29), (30), and (31), we can derive

$$\text{Equation 32} \qquad \frac{1}{m} = \frac{\partial ln\dot{\varepsilon}}{\partial ln\sigma} = \frac{\frac{\partial \dot{\varepsilon}}{\dot{\varepsilon}}}{\partial ln\sigma} = \frac{1}{(\dot{\varepsilon}_a+\dot{\varepsilon}_c)} \cdot \left(\frac{\partial \dot{\varepsilon}_a}{\partial ln\sigma} + \frac{\partial \dot{\varepsilon}_c}{\partial ln\sigma}\right) = \frac{1}{(\dot{\varepsilon}_a+\dot{\varepsilon}_c)} \cdot \left(\frac{\dot{\varepsilon}_a}{m_a} + \frac{\dot{\varepsilon}_c}{m_c}\right),$$

where m_a (SRS of amorphous phase) and m_c (SRS of crystalline phase) are $\frac{\partial ln\sigma}{\partial ln\dot{\varepsilon}_a}$ and $\frac{\partial ln\sigma}{\partial ln\dot{\varepsilon}_c}$, respectively.

Equation (32) can be simplified into the following equation in the form of displacement for each phase:

$$\text{Equation 33} \qquad \frac{1}{m} = \frac{\Delta L_a}{\Delta L_a+\Delta L_c} \cdot \frac{1}{m_a} + \frac{\Delta L_c}{\Delta L_a+\Delta L_c} \cdot \frac{1}{m_c}.$$

This equation should be applicable for the determination of SRS of composites from SRS of each phase under iso-stress condition. For Cu/a-CuNb multilayers in this study, $\frac{\Delta L_a}{\Delta L_a+\Delta L_c}$ and $\frac{\Delta L_c}{\Delta L_a+\Delta L_c}$ (displacement by each phase over the total displacement) represent how much deformation is accommodated by crystalline Cu layers and a-CuNb layers among the total deformation. $\frac{\Delta L_c}{\Delta L_a+\Delta L_c}$ should vary from 0.5 to 1 in this study. A value of 1 (upper boundary) means that at larger h, Cu layers accommodate most of the plastic deformation; and 0.5 (lower boundary) indicates that at smaller h, Cu and a-CuNb equally share the plastic deformation (co-deformation of Cu and a-CuNb layers). Here we made a simple assumption that $\frac{\Delta L_c}{\Delta L_a+\Delta L_c}$ is proportional to the increase of h ($\frac{\Delta L_c}{\Delta L_a+\Delta L_c} = 0.5 + \frac{h}{200}$). By taking m_c as the SRS of Cu in this study, 0.05, and m_a as a number close to zero (due to the limited SRS of amorphous alloys), a calculated m vs. h can be generated from Equ. 33 (shown as the dashed curved line in Fig. 41a). Good agreement between the simple modelling and experimental data suggests that plastic strain accommodated by amorphous and crystalline layers varies with the change of h.

Studies have shown that by tailoring the thickness of crystalline and amorphous layers, C/A multilayers can co-deform without the formation of shear bands at smaller h.[83, 92, 93] In this study, when h > 100 nm (Regime II, $\frac{\Delta L_c}{\Delta L_a+\Delta L_c}$ is approaching 1), the Cu layers deform plastically due to their lower yield strength, and accommodate a majority of the total strain by dislocation motions. The SRS of C/A multilayers is controlled by dislocation pile-up against C/A interfaces and dislocation interactions insides Cu layers (Fig. 41c), so Cu/a-CuNb 100 nm and 150 nm multilayers have SRS similar to that of the single layer Cu. A larger m for the Cu/a-CuNb multilayers than Cu film should result from smaller grain size and smaller activation volume in multilayers. The enhanced SRS (a large m value) for C/A multilayers indicates better ductility and strain hardening behaviors. In contrast, when h < 50 nm, the yield strength of Cu is approaching that of a-CuNb, and at the same time, the a-CuNb with smaller h becomes more ductile than those with larger h. Consequently Cu and a-CuNb layers may co-deform and partition the total strain (regime I, $\frac{\Delta L_c}{\Delta L_a+\Delta L_c}$ is approaching 0.5). For Cu layers, because of finer layer thickness and lower dislocation density, limited dislocation activities occur in the form of confined layer slip instead of dislocation pile-ups; for a-CuNb layers, the deformation is accommodated by motions of shear transformation zones (Fig. 41c). Depending on the strain accommodated by Cu and a-CuNb layers, the overall SRS (m) is affected by h as shown in Fig. 41a. As shown in Fig. 41b, the activation volume of Cu/a-CuNb multilayers decreases with the increase of h up to 100 nm, which also suggest fewer dislocation activities at smaller h.

V.5 Conclusions

In summary, the SRS of C/A multilayers determined from nanoindentation tests is layer-thickness dependent: the SRS of multilayers increases with increasing h up to 50 nm and is comparable to that of Cu film when h > 100 nm. At smaller h, crystalline and amorphous layers co-deform with limited dislocation activities, and at larger h, crystalline layers accommodate most of the plastic strain by dislocation motions. Based on the model of crystalline/amorphous composites under iso-stress condition, the relationship between SRS of C/A multilayers and individual layer thickness can be predicted.

CHAPTER VI

STUDY OF LAYER THICKNESS EFFECT ON FRICTION BEHAVIORS OF CU/AMORPHOUS-CUNB MULTILAYERS BY NANOSCRATCH TECHNIQUE

VI.1 Overview

Amorphous alloys are shown to exhibit high hardness and good wear resistance. However, the brittleness of amorphous alloys could present undesired properties such as shear softening and cracking under mechanical loading. In this study, we focus on comparison of friction behaviors of Cu/amorphous-CuNb multilayers and single layer amorphous CuNb films via nanoscratching. Single layer amorphous CuNb film shows good friction behaviors until certain loads after which coefficient of friction jumps to a much higher value. In contrast, Cu/amorphous-CuNb multilayers can exhibit more stable coefficient of friction without forming shear bands. By tailoring individual layer thickness, optimal friction behaviors can be achieved at 20 nm.

VI.2 Introduction

Extraordinary mechanical properties of MGs including outstanding yield strength and wear resistance make them suitable engineering materials in tribological applications [1, 3, 6, 111]. In the absence of dislocations and grain boundaries, MGs can be fabricated with superior surface flatness which alleviate the wear and energy loss by friction [26]. Zr-based Bulk metallic glasses (BMG) used for golf clubs show enhanced performance compared with crystalline alloys [27]; Micromotor equipped with Ni-based BMGs gears has a much longer life time compared with motors with conventional steel gears [26, 175, 176]; Zr-based BMGs as surgical blades demonstrate better sharpness and cutting ability compared commercial ones [177]. Meanwhile, thin film metallic glass (TFMG) as coatings are also applied in medical tools, MEMS, and enhancement of fatigue life of steels [77, 178]. In these applications, friction and wear properties are of great concern, and the attractive tribological properties benefit from high hardness (H) and very small surface roughness. According the classical Archard equation, larger H leads to better wear resistance [109]. Various MGs demonstrate enhanced wear behaviors with the increase of hardness [112, 113]. For example, Huang et al. [179] showed that wear resistance of Ce-, Ti-, and Fe-based MGs increases with increasing hardness. Although H can greatly affect the tribological behaviors, the ratio of H and E (elastic modulus) can serves as a more appropriate parameter to predict the wear behaviors [180]. This makes MGs more promising candidates in tribological applications, since MGs have very large H and smaller E, and thus a much larger H/E, compared with crystalline counterparts [1, 4]. Hodge and Nieh [181] compared wear behaviors of various MGs and suggested that wear resistance differences could result from different wear mechanisms instead of solely hardness. In short, tribological behaviors can be greatly affect by *H* (related to resistance to indentation), but also closely related with deformation and fracture modes such as crack nucleation and propagation. In order to achieve desired tribological properties, both high hardness and appropriate deformability are necessary.

Furthermore, crystallites/particles reinforced metallic glass composites (MGc) generally show improved wear behaviors along with increased *H* compared monolithic MGs [182-186]. But partially crystallized MGs can also exhibit poor wear behaviors due to the embrittlement of crystalline phases which leads to easier crack nucleation and propagation [113]. It has also been shown that separation of crystals in amorphous matrix can greatly affect the wear behaviors [187]. To understand the underlying mechanisms of crystalline/amorphous (C/A) interfaces and dimension of crystalline phases on friction behaviors of MGc, accurately designed and fabricated C/A structures are needed. Therefore, crystalline/amorphous multilayers with designed C/A interfaces and controlled layer thickness are desired. Alpas and Embury [114] showed that in Cu/Ni-based MGs laminated composites (at micron scale), MGs can accommodate applied load with small deformation due to its high hardness and suppress the damage in Cu, thus effectively enhancing the wear resistance. However, to the best of our knowledge, this is the first study on friction behaviors of C/A nanolaminates, despite of the intensive studies on friction behaviors of crystalline/crystalline multilayers [188-190] and ceramic/amorphous multilayers [191]. Studies show that C/A multilayers can exhibit enhanced mechanical properties in terms of strength and plasticity compared with monolithic MGs and that plasticity can be accommodated by homogeneous deformation instead of shear banding with decreasing layer thickness [74, 87, 88, 91-93, 164]. Therefore, layer thickness could potentially affect friction behaviors of C/A multilayers due to the change in deformation mode and strength.

In this paper, we investigate the friction behaviors of single layer amorphous CuNb films and Cu/amorphous CuNb multilayers (referred to as a-CuNb and Cu/a-CuNb respectively hereafter) via systematic nanoscratch tests performed under constant load, low ramping load, and high ramping load modes. Single layer a-CuNb films show superior friction behaviors under constant load mode. However, coefficient of friction (*COF*) of a-CuNb films jumps to a much at certain loads under ramping load modes. In comparison, even with lower *H*, Cu/a-CuNb multilayers demonstrate more stable *COF*. By tailoring individual layer thickness (*h*) of multilayers, optimal friction behaviors can be achieved when *h* =20 nm without forming shear bands or chips after nanoscratch. The results of this study help to understand the criteria to enhance tribological behaviors of MGc and TFMGc, which are beneficial for their applications in tribology-dominated environments such magnetic storage industry [192].

VI.3 Experimental

Cu/a-CuNb multilayers were deposited on Si substrates by direct current magnetron sputtering at room temperature. Individual layer thickness (*h* from 2.5 nm to 100 nm) for a-CuNb and Cu layers were the same in multilayers. Single layer a-CuNb and Cu films were also deposited as references. And all the films in study have a thickness of 1 μm. Chamber pressure was under 1×10^{-7} Torr and $1-3\times10^{-3}$ Torr Ar was used during deposition. a-CuNb layers were deposited by co-sputtering Cu and Nb with a composition of Cu 50 at.% and Nb 50 at.%. And for multilayers, a-CuNb layer is the cap layer and Cu layer is the bottom layer. Microstructure of films were characterized by Transmission Electron Microscopy studies *via* an FEI Tecnai G2 F20 microscope operated 200 kV. Hysitron TI950 TriboIndenter and TI Premier were employed to obtain the hardness and modulus of all the films. At least 12 tests were done for each specimen to ensure reproducibility. Data including *COF*, force, scratch depth and length were obtained by *in situ* measurements during nanoscratch, residual depths were acquired by retracing after nanoscratch. Morphology after nanoscratch was characterized by Scanning Electron Microscopy (SEM) experiments by Tescan LYRA-3 (Model GMH) Focused Ion Beam SEM.

VI.4 Results

VI.4.1 Experimental design and microstructure characterization

The films were tested under three different modes: constant load, low ramping load and high ramping load modes, as shown in Fig. 42. Normal load and scratch depth are not changed under constant load mode, but keep increasing under ramping modes. The indent tip radius for constant load and low ramping modes is 1μm, but 5 μm for high ramping load. Results from different modes suggest a change of friction mechanism and unfold the effect of tip radius.

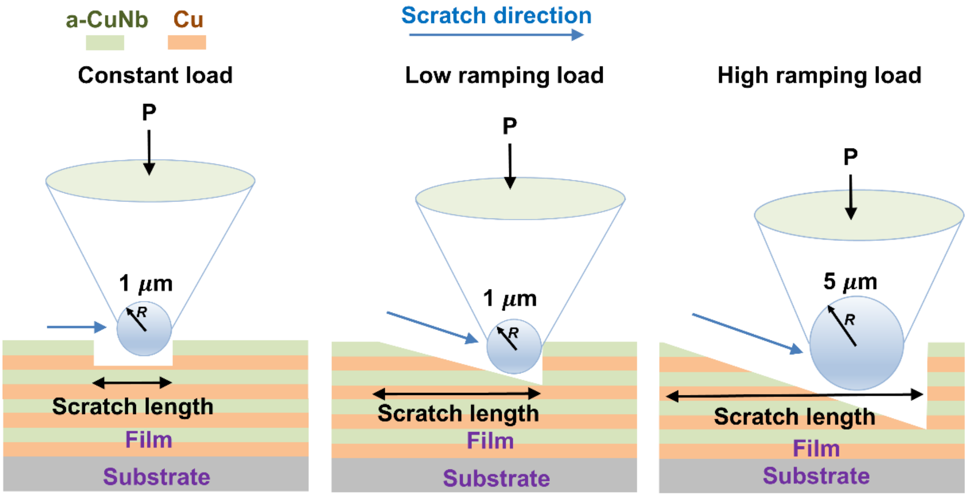

Mode	Load range	Loading rate	Scratch length	Scratch speed
Constant load	Constant	0	6 μm	0.4 μm/s
Low ramping load	0-2 mN	0.13 mN/s	11 μm	0.73 μm/s
High ramping load	0-25 mN	0.83 mN/s	250 μm	8.3 μm/s

Figure 42. Schematic showing the nanoscratch experiments under three different modes. Under constant load mode, load is not changed during nanoscratching; under low ramping load and high ramping load, load (scratch depth) is increasing during nanoscracthing. High ramping load was achieved with larger indenter tip, deeper depth, longer scratch length, and faster scratch speed.

Cross-section TEM images show the microstructure of Cu 2.5 nm/a-CuNb 2.5 nm (referred to Cu/a-CuNb 2.5 nm hereafter) and Cu/a-CuNb 50 nm in Fig. 2a and 2b respectively. Alternating crystalline Cu layers and featureless a-CuNb layers can be seen for all the multilayers. C/A interfaces can be clearly identified even when h is reduced to *h*. Grain size in Cu layers are comparable to *h* when h is above 20 nm. But grain size is larger than *h* when h is below 20 nm, as shown in Fig. 43.

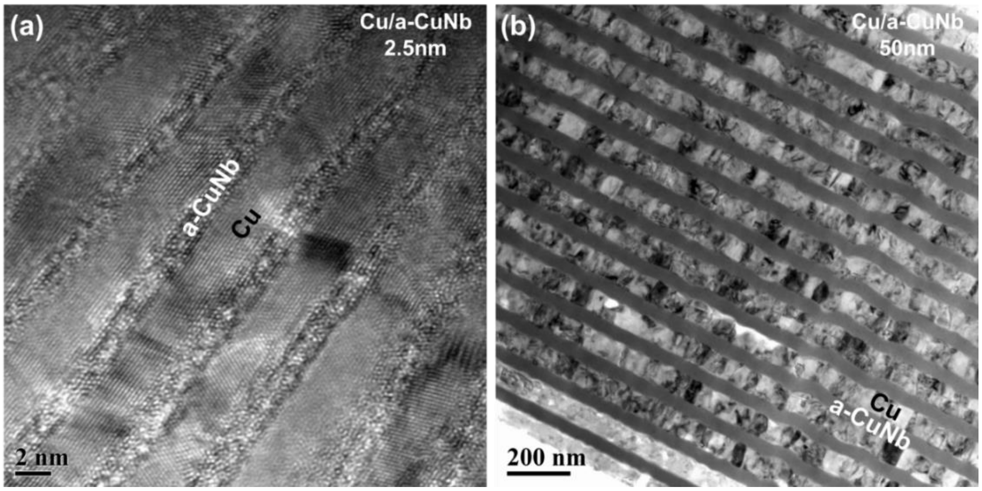

Figure 43. TEM images Cu/a-CuNb 2.5 nm (a) and Cu/a-CuNb 50nm (b) multilayers. Alternating crystalline Cu and featureless a-CuNb layers can be observed.

Table 3. Summary of Hardness, modulus and coefficient of friction for single layer and multilayer films

Specimen	**E (GPa)**	**H (GPa)**	**COF_Constant Load**	**COF_Ramp (0-2mN)**	**COF_Ramp (0-25mN)**
Cu	113±9.5	2.3±0.1	/	/	0.29-0.39
a-CuNb	135±3.1	7.3±0.1	0.115-0.255	0.12-0.55	0.15-0.46
Cu/a-CuNb_2.5nm	/	4.6±0.2	0.129-0.297	0.12-0.35	0.22-0.32
Cu/a-CuNb_20nm	126±3.5	4.8±0.2	0.128-0.279	0.12-0.34	0.18-0.23
Cu/a-CuNb_50nm	119±4.8	4.5±0.2	0.151-0.254	0.18-0.51	0.19-0.50
Cu/a-CuNb_100nm	122±4.5	3.8±0.2	/	/	0.27-0.51

VI.4.2 Nanoscratch tests under constant load mode

Normal displacement (scratch depth) and COF as a function of time of a-CuNb film and Cu/a-CuNb 2.5, 20, and 50 nm are shown in Fig.44. Because of the hardness variations among all the films (as shown in Table 3), different loads were applied for different films to ensure the similar scratch depths. For all the films, scratch depths remain unchanged due to the constant load applied and get deeper under larger loads (Fig. 44a). COF of all the films were stable during scratch with certain fluctuations and increases with the increase of load. COF with respect to normal displacement (scratch depth) is shown in Fig. 45. COF increases with the increase of scratch depth conforming to a linear relationship. However, for at any given scratch depths, a-CuNb has the lowest COF as indicated by the black dashed line. COF of multilayers are similar residing in the guided elliptical.

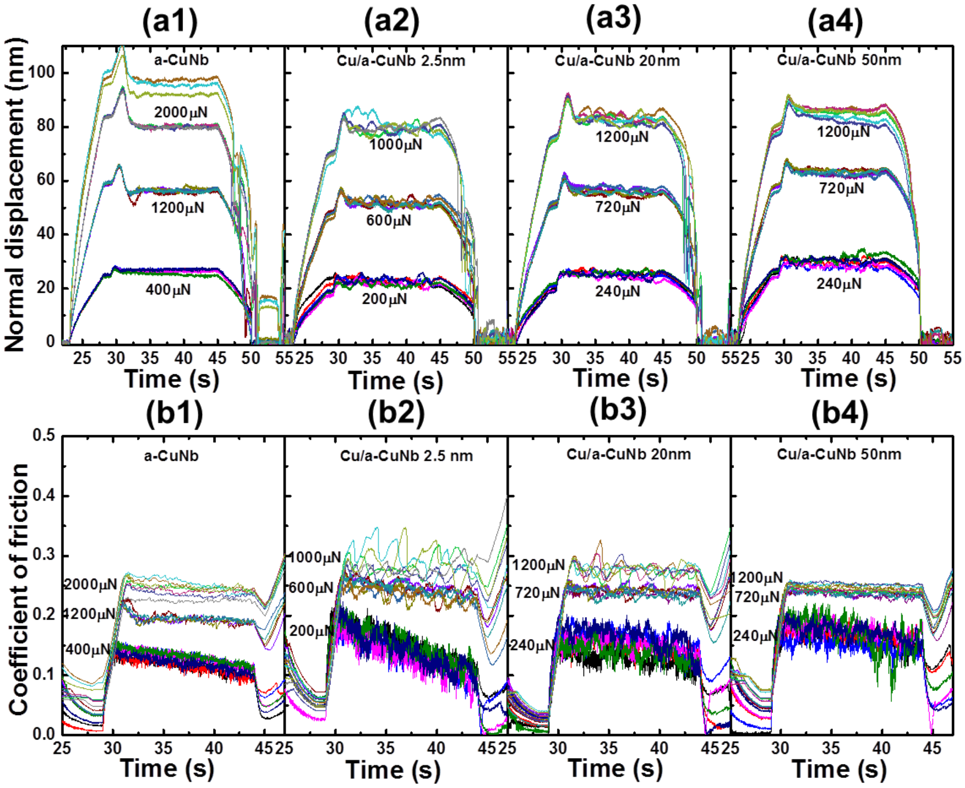

Figure 44. Nanoscratch tests under constant load mode. Normal displacement-time curves were shown for a-CuNb (a1), Cu/a-CuNb 2.5 nm (a2), Cu/a-CuNb 20 nm (a3), and Cu/a-CuNb 50 nm (a4). Various loads were employed to achieve similar normal displacements for different samples. Coefficient of friction-time curves were shown for a-CuNb (b1), Cu/a-CuNb 2.5 nm (b2), Cu/a-CuNb 20 nm (b3), and Cu/a-CuNb 50 nm (b4).

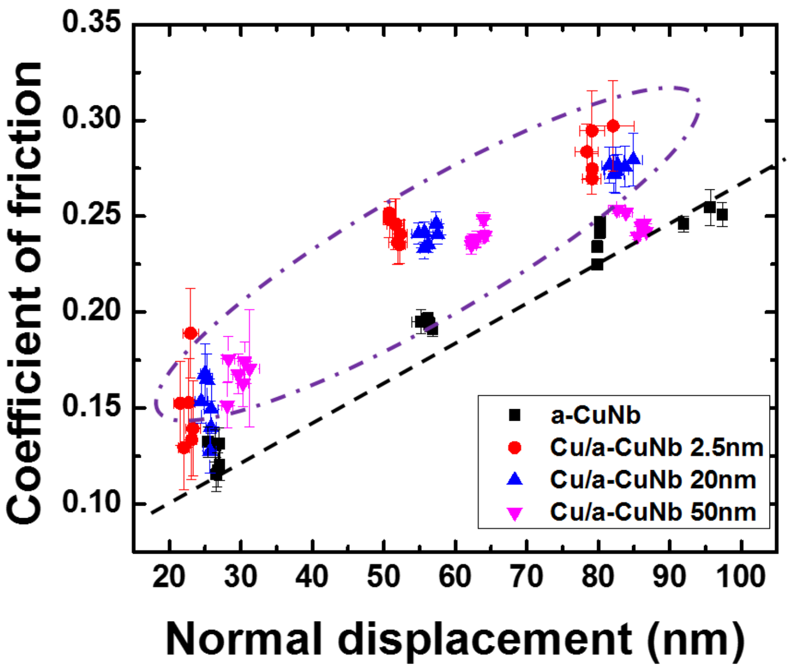

Figure 45. Coefficient of friction as a function of normal displacement under constant load mode. A guided dashed line is added for single layer a-CuNb film. Data of Cu/a-CuNb multilayers fall in the elliptical.

VI.4.3 Nanoscratch tests under ramping mode

The relationship of COF and normal load under low ramping mode is shown in Fig. 46a-d (Lines in different colors represent repeated scratch tests for the same sample). Despite that a-CuNb has the lowest starting COF (less than 0.2) in the beginning, COF of all the a-CuNb films increases sharply to ~0.5 at a load of ~ 1.2 mN. With the introduction of crystalline Cu, Cu/a-CuNb multilayers show more stable COF as a function of normal load. COF of Cu/a-CuNb 50 nm generally increases moderately after reaching a load of 1.6 mN. When reducing h to 20 nm, COF remains very stable up the maximum load 2 mN. And Cu/a-CuNb 2.5 nm has stable COF but with certain fluctuations. Normal displacement vs. scratch length is shown in Fig. 46e. a-CuNb has the smallest normal displacement due to its very high hardness, 7.3 GPa (Table 1), but a sudden dip occurred at ~ 7 um scratch length which also corresponds with jump at a load of 1.2 mN in Fig. 46a. All multilayers have similar normal displacement due to their similar hardness, 4.5-4.8 GPa (Table 3). Elastic recovery rate is the ratio of recovered displacement (h_{rec}) after nanoscratch over the total displacement (h_{total}) during nanoscratch. The recovered displacement can be obtained by subtracting the residual displacement (h_{res}) from h_{total}. In this study, h_{res} was measured by retracing of the tip with depth sensing capability after nanoscratch. Elastic recovery rate ($\frac{h_{total}-h_{res}}{h_{total}}$) plotted as a function of scratch length is shown in Fig. 46f. Multilayers have similar elastic recovery rate without jump. a-CuNb films starts with very good elastic recovery, but plummet at a scratch length of ~7 um, matching the jumps in Fig. 46a and 46e.

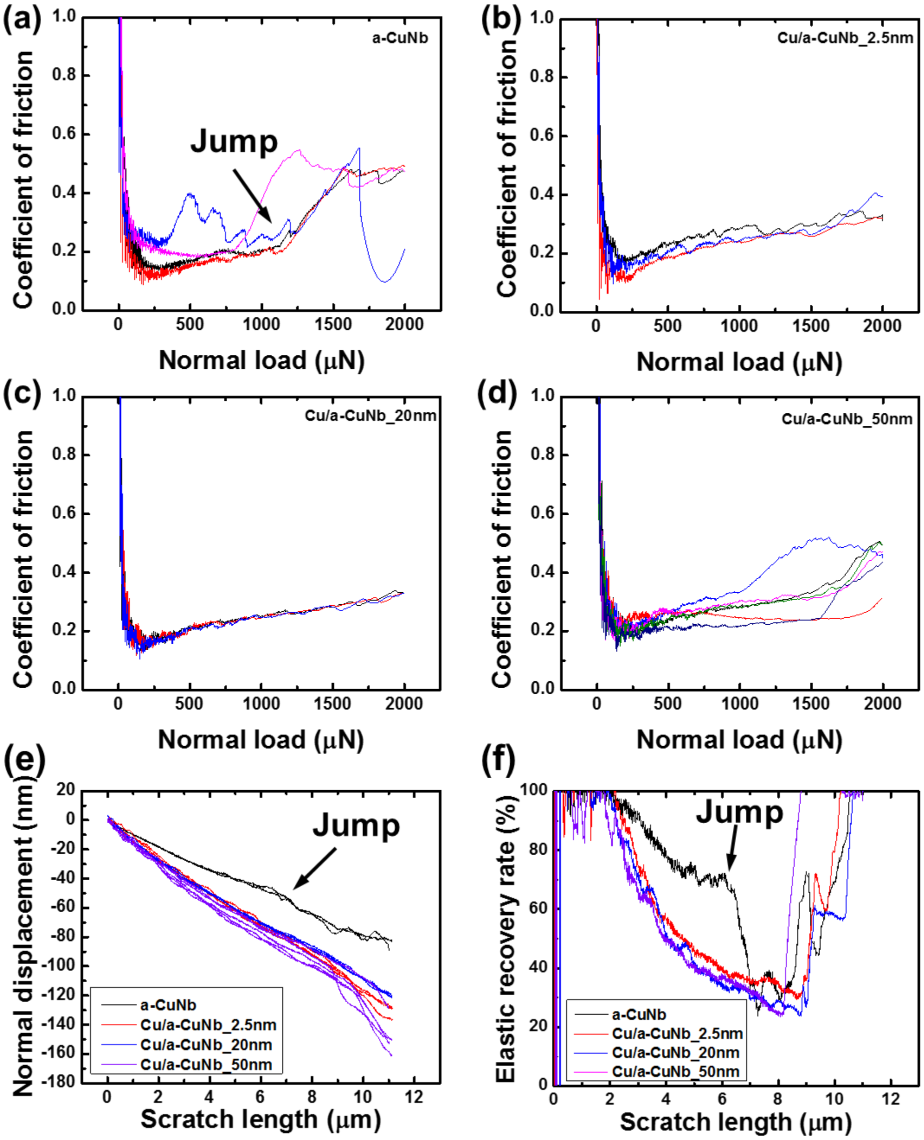

Figure 46. Nanoscratch results of all the films under low ramping mode. Coefficient of friction vs. normal load under low ramping load (up to 2 mN) is shown for a-CuNb (a), Cu/a-CuNb 2.5 nm (b), Cu/a-CuNb 20 nm (c), and Cu/a-CuNb 50nm (d). Normal displacement (scratch depth) (e) and elastic recovery rate (f) vs. scratch length of all the film are compared. Elastic recovery rate is the ratio of recovered displacement over total displacement.

Under high ramping load, similar results can be found in terms of relationship of COF vs. normal load for the films in Fig. 47. COF of a-CuNb films has clear jumps, jumps at a later stage for Cu/a-CuNb 50 nm multilayers, shows certain variations for Cu/a-CuNb 2.5 nm multilayers, and remains very stable for Cu/a-CuNb multilayer. However, for a-CuNb films, jump of COF happens in only ~ 50 % of tests performed under high ramping load, but occurs in all the tests under high ramping load. Besides, the load at which jump happens for a-CuNb and Cu/a-CuNb 50 nm is ~ 15 mN and 20 mN for a-CuNb and Cu/a-CuNb multilayer films, much larger than the loads under low ramping load.

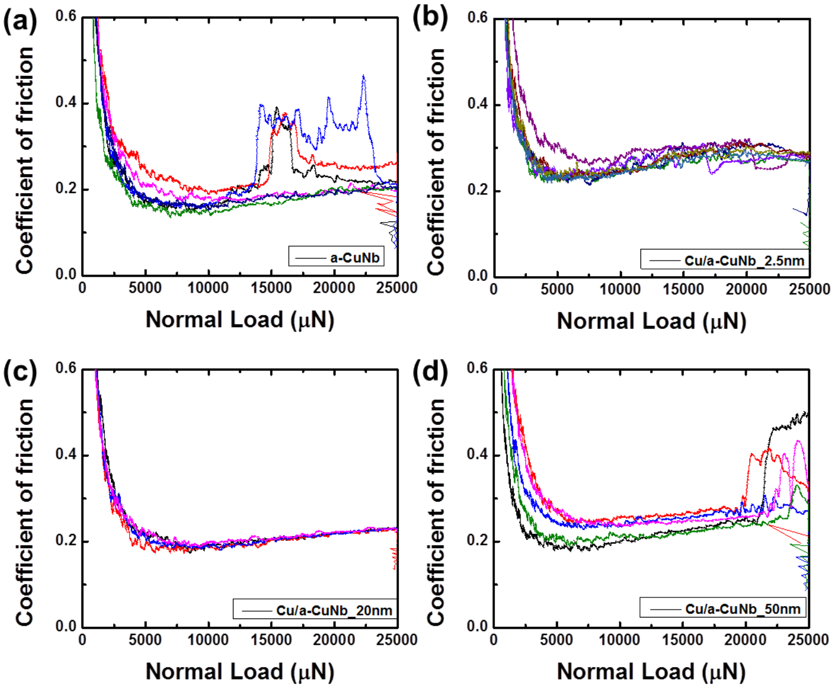

Figure 47. Coefficient of friction vs. normal load under high ramping load (up to 25 mN with a scratch length of 250 μm) is shown for a-CuNb (a), Cu/a-CuNb 2.5 nm (b), Cu/a-CuNb 20 nm (c), and Cu/a-CuNb 50nm (d).

VI.4.4 Morphology of films after nanoscratch under high ramping load

Scratch morphology of films were characterized by SEM studies. Morphology overview of all the films after high ramping load tests were shown in Fig. 48. Due to the very high hardness of a-CuNb film (the maximum load for all the films under high ramping load is the same, 25 mN), the scratches are shallow (Fig. 48a), and some chips are identified as shown in the inset (magnified area of the dashed box). In comparison, scratches of Cu films are deep and surrounded by very frequently observed fragmented chips (Fig. 48b). Cu/a-CuNb 100 nm multilayer has obvious chips but they are not as broken as Cu film, and very long chips reside on both side at the end of the scratch as shown in the inset (Fig. 48c). Cu/a-CuNb 2.5 nm has less obvious chips which usually form at the end of the scratch (Fig. 48d). However, Cu/a-CuNb 20 nm basically contains no chips after nanoscratching and has very smooth scratch morphology (Fig. 48e).

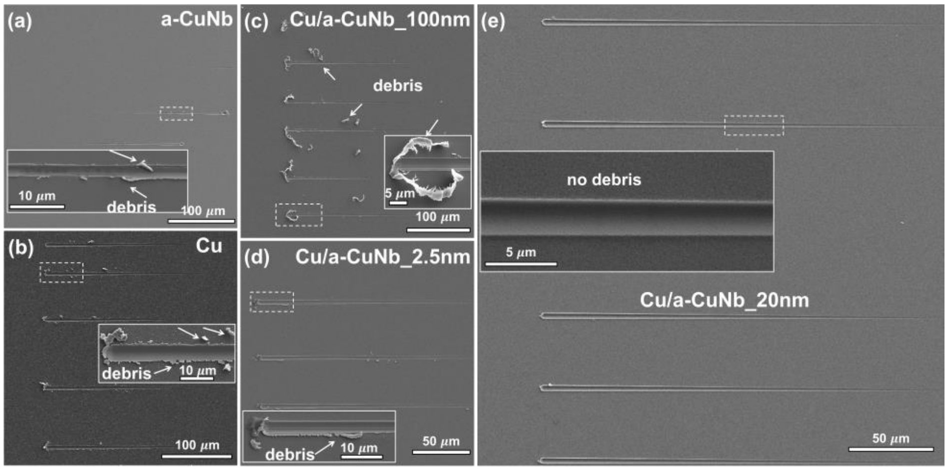

Figure 48. SEM images of a-CuNb (a), Cu (b), Cu/a-CuNb_100 nm (c), Cu/a-CuNb 2.5 nm (d), and Cu/a-CuNb_20 nm (e) after high ramping load scratch. Obvious debris has been observed for all the films except Cu/a-CuNb 20nm.

Higher magnified SEM images from Fig. 49 reveal the microstructure change after nanoscratch. For a-CuNb films (Fig. 49a), there are not so many chips overall after nanoscratching, but localized deformation occurs as revealed by the grooves and microcracks inside the scratch. Wing-like shear bands are clearly observed along the two sides of the scratch. Average spacing between shear bands is ~ 265 nm, and shear steps can be easily found. For Cu/a-CuNb 50 nm multilayer (Fig. 49b), grooves and microcracks exist but no shear bands can be found instead of the possible sheared zones (dashed elliptical in Fig. 49b2). Both films demonstrated obvious pile-up on both sides of the scratch which experienced severe deformation as manifested by cracks or shear bands. In drastic contrast, Cu/a-CuNb 20 nm (Fig. 49c) has less obvious pile-up and very smooth scratch morphology without any shear bands or cracks.

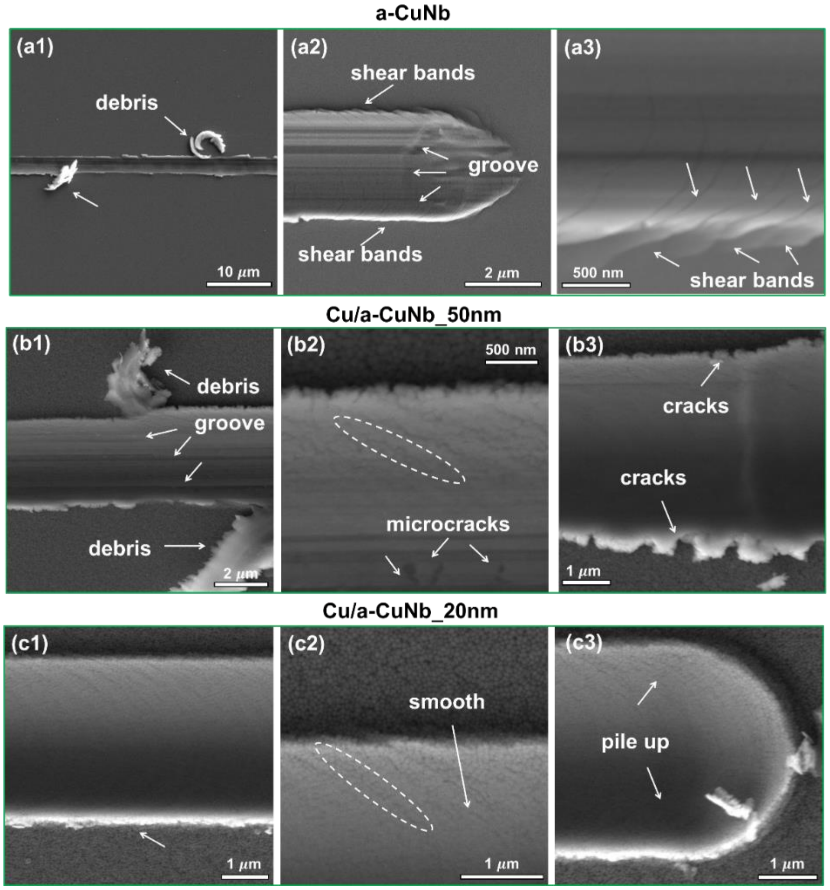

Figure 49. High resolution SEM images of a-CuNb (a), Cu/a-CuNb 50 nm (b), and Cu/a-CuNb 20 nm (c) after high ramping load scratch. Grooves, debris, pile-ups, and shear bands are frequently observed in a-CuNb film (a1-a3). No shear bands were formed in Cu/a-CuNb 50 nm multilayers, but debris, grooves, smeared pile-ups, and microcracks do exist (b1-b3). No shear bands, grooves or smeared pile-ups are found in Cu/a-CuNb 20 nm multilayer (c1-c3).

VI.5 Discussions

VI.5.1 Superior friction behaviors of a-CuNb films under constant load mode

A summary of hardness, modulus, and coefficient of friction for all the tested films in this study is shown in Table 3. Among all the tests, single layer a-CuNb film has the highest hardness and modulus, ~ 7.3 GPa and 135 GPa, while Cu film has the lowest, ~ 2.3 GPa and 113. Multilayer with layer thickness smaller than 50 nm has similar hardness, 4.5-4.8 GPa, which is also close to the rule of mixture value of single layer a-CuNb and Cu films, while Cu/a-CuNb 100 nm multilayer has a much lower value, ~ 3.8 GPa [160]. During nanoindentation tests, under the same load, smaller indentation depths are achieved for harder materials. Similarly, in order to achieve similar normal displacement during nanoscratch, a larger load needs to be applied for harder materials, as shown in Fig. 44a. Under constant load mode, once the maximum normal displacement is achieved, the coefficient of friction is very stable. Coefficient of friction with respect to normal displacement in Figure 45 shows that a-CuNb films has the lowest COF from 0.115 to 0.255, guided by the dashed line. This results can be expected, since based on the Archard relationship, harder materials usually has better wear resistance. COF of multilayers are similar as indicated by the elliptical. Since coefficient of friction the ratio of normal force/lateral force, the lateral friction force is the smallest for a-CuNb films. Since the contact area is similar due to the similar normal displacement, considering the similar at this scale (below 100 nm) is limited. The reasons lead to smallest lateral friction force for a-CuNb films could come from the deformability. Due to the high hardness of a-CuNb and limited deformability, materials from a-CuNb films are less likely to removed or pushed out. Instead, abraded materials in multilayers could reside between the tip and films, which shifts the process from sliding wear to abrasive wear and increases the COF.

Another important information is COF of the films increases with the increase of normal displacement instead of keeps as a constant. This phenomena could result from the very small normal displacement of nanoscratch, surface effect could play a role and the scratch process does not reach an equilibrium.

VI.5.2 Unstable friction behaviors of a-CuNb films under ramping load modes

Unlike the lowest COF for a-CuNb films under constant load mode, COF of a-CuNb jumps at certain load and normal displacement. High and low ramping modes have a much large scratch length and depth compared with constant load mode, during scratch. The jump happens at a normal displacement of ~ 50 nm at which depth there is no change of COF under constant load mode. This suggest that normal displacement is not the determinant factor for the occurrence of jump. Under ramping modes, instead of sliding itself, the tip is penetrating deeper and deeper therefore the stress state could be more complicated, and more materials are involved during scratch which could cause more stress concentrations and thus lead to sudden increase of plastic deformation. The unstable COF under these modes suggest that different deformation mechanisms could kick in during ramping modes. Under the low ramping mode, both normal displacement and elastic recovery rate plummet at a load of 1.2 mN and a length of 7 µm. A large elastic recovery rate corresponds to better wear resistance since less materials are displaced. This indicates the sudden increase of irrecoverable plastic deformation of a-CuNb films. On the other hand, SEM images post-nanoscratch shows high density shear bands and cracks at the end of the scratch (Figure 49). This suggests that due to the brittle nature of amorphous alloys, microcracking or shear banding occurs when certain required stress is reached. Either microcracks or shear bands will lead to sudden softening of the materials which leads to the sudden increase of normal displacement and decrease of elastic recovery rate. Besides, microcracks increase the local stress concentration and force the deformation to occur along the crack propagation direction, and shear banding results in localized deformation inside the shear bands. Both causes irrecoverable deformation and increases the contact area between the tip and the films. These effects in turn promote sudden increase of lateral friction, so a sudden increase of COF is also observed.

Comparison of sudden increase of COF under low and high ramping mode shows that at high ramping mode jumps do not always happen and require a larger load if happened. The reasons lies in the different scratch tip diameters and therefore different contact area under the indenter. The stress state below the tip during nanoscratch should involve both compressive and shear component more complicated than that during nanoindentation. But since in this study a spherical indenter tip is applied, an estimated stress (σ) can be calculated without consideration of materials sink-in and pile-up using,

$$\text{Equation 34} \qquad \sigma = \frac{P}{\pi(R^2-h^2)},$$

where P is the applied normal load, R is the tip diameter, and h is the normal displacement. For low ramping mode, if R and h is taken as 1μm and 50 nm, respectively, the calculated σ is 380 MPa. Taken R and h is taken as 5μm and 185 nm for high ramping mode, the calculated σ is 190 MPa. Both values are much lower than the resolved shear stress for single layer a-CuNb film to yield ~ 900 MPa (H/8.1). However, the calculated stresses do not cause the shear banding or cracking of the whole materials under tip but in some local region where stress concentrations are large due to the inhomogeneity or debris between the sample and tip. The is supported by the localized grooves after scratch. The calculated value does show that in order for instability to happen while scratching with a large tip, much larger loads should be applied.

On the other hand, the reason for absence of COF jumps for some a-CuNb tests could be two fold. First, the maximum stress applied in the end for high ramping load mode is 320 MPa, which may not be large enough to cause shear banding or microcracking. Second, applying the load over a much larger area (larger tip diameter) might reduce the overall stress concentration which could alleviate the jumps.

VI.5.3 Optimizing friction properties of Cu/a-CuNb multilayers by tailoring h

Wen et al. [189] attributed the improved friction and wear behaviors of Ag/Ni multilayers at finer individual layer thickness to the increased *H/E* (hardness/modulus). Cu/a-CuNb 100 nm has a lower H/E compared with multilayers with smaller *h*. But for Cu/a-CuNb multilayers 50 nm, COF jumps also occur. But the underlying mechanism could be very different. For multilayers, no signs of shear bands can be found after nanoscratch. But microcracks do exist for Cu/a-CuNb with h > 50 nm. Therefore, microcracking should dominate the jump of these multilayers. Nanoscratching in this study involves both compressive and shear stress. Therefore, considering the hardness of materials only is not sufficient. As shown in Fig. 50a, COF of the multilayer is the lowest for Cu/a-CuNb 20 nm. It is clear there exist an optimal layer thickness in order to achieve the optimal friction behaviors. Fig. 50b demonstrates that although hardness of multilayers reaches a plateau when *h* is under 50 nm, flow stress under tension has a reverse trend at 20 nm. Cu/a-CuNb 20 nm has the highest strength both under tension and under compression. This is why after nanoscratch, it has the lowest COF and very smooth scratch without shear bands or chips. This suggests under the same load Cu/a-CuNb 20 nm can deform without microcracking or shear banding but accommodate deformation in a relatively homogeneous manner. This can be achieved by delocalizing the strain into a much larger region without triggering the detrimental plastic deformation like microcracking or shear banding.

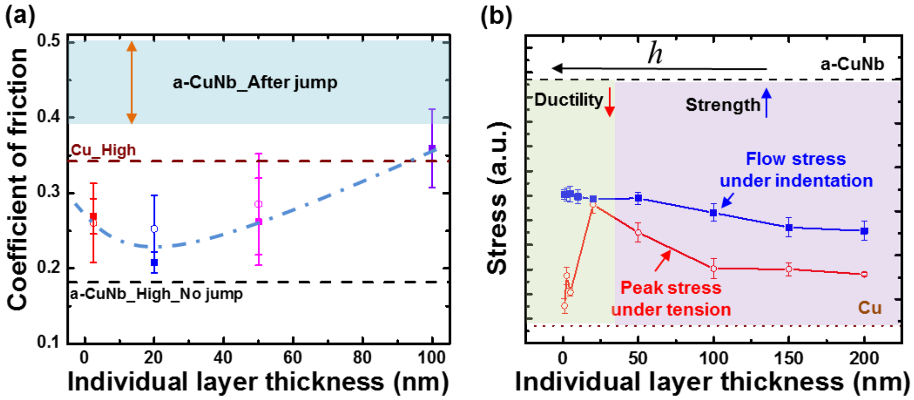

Figure 50. (a) Comparison of the average COF of multilayers under low (open hexagon) and high (solid filled squares) ramping load. COF of single layer Cu and a-CuNb films were also added as references. (b) Stress evolution of Cu/a-CuNb multilayers with respect to individual layer thickness under tension and indentation.

Another interesting phenomenon is that Cu somehow has a lower COF and less chips/debris than Cu/a-CuNb 100 nm, despite a much lower hardness. For Cu/a-CuNb 100 nm multilayers many chips can be identified after nanoscratch. The maximum stress under the tip for Cu/a-CuNb 100 nm is actually very close to the critical resolved shear stress is

469 MPa (H/8.1). Therefore, the delamination between Cu and a-CuNb multilayers can happen. In fact, Rosenfield [193] pointed out that shear could preferentially occur below the surface. The crystalline/amorphous interfaces parallel to the surface could delaminate during the process. Therefore, many materials are removed and sheared during scratch process, as supported by the large chunks of debris. Therefore, these phenomenon does not occur for Cu/a-CuNb with smaller *h* is probably due to their larger interface strength.

VI.6 Conclusions

Nanoscratch tests at various modes were performed for single layer a-CuNb, Cu, and multilayer films. Our results show that a-CuNb films have the best friction behaviors at constant load mode which has a smaller scratch length and depth but experience unstable COF jump at low ramping modes. For Cu/a-CuNb multilayers, varying the individual layer thickness, friction behaviors are changed. When *h* = 20 nm, optimal friction behaviors can be achieved. While designing the materials with optimal friction behaviors, both strength and deformability should be considered.

CHAPTER VII

SUMMARY

In conclusion, various mechanical properties of crystalline-amorphous nanolaminates were investigated. The strengthening mechanisms, fracture behaviors, strain rate sensitivity, and friction behaviors were studied in detail. First, our system, Cu/amorphous CuNb multilayers demonstrate different characteristic scale ~ 50 nm after which strength cannot be further increased. Crystalline/amorphous interface with medium-range-order and positive mixing enthalpy between Cu and Nb could result in the hardness plateau below 50 nm. Second, the architecture and volume fraction of crystalline/amorphous multilayers can have important effect on fracture behaviors. Third, layer thickness effect on strain rate sensitivity of crystalline/amorphous multilayers is reported. Dominant deformation mechanisms at different length scales control the strain rate sensitivity. Fourth, introduction of crystalline phases can suppress the instability of friction behaviors of single layer amorphous CuNb films. Softer multilayers can show better friction behaviors under certain circumstances. The studied four categories of properties of crystalline/amorphous multilayers are interconnected. The results demonstrate the mechanical responses of materials with the same microstructure under different testing conditions and could provide valuable insights in applications of crystalline-amorphous nanolaminates.

More importantly, the strategies of utilizing ductile phases (crystalline Cu) to enhance the mechanical behaviors of brittle phases (amorphous CuNb) are accomplished. The findings in this study could be potentially applied in other brittle/ductile systems, such as ceramic/crystalline, glass/crystalline, or crystalline/polymer composites. Furthermore, the interface and dimension of each phase can affect the overall mechanical behaviors. For example, Cu/a-CuNb 20 nm multilayers are not only the hardest film among multilayers, but also are the films with optimal fracture and friction behaviors. Thus, while designing the brittle/ductile systems for various applications, the dimension should be kept in mind especially at nanoscale. Last, although the work presented in this dissertation is significant, more questions could be solved by further research. I wish to continue pursuing a deeper understanding of the atomistic mechanisms of the systems under *in situ* TEM experiments as well as the detailed microstructure change after deformation.

REFERENCES

[1] L. Tian, Y.-Q. Cheng, Z.-W. Shan, J. Li, C.-C. Wang, X.-D. Han, J. Sun, E. Ma. Approaching the ideal elastic limit of metallic glasses, Nat. Commun. 3 (2012) 609.

[2] A.L. Greer, E. Ma. Bulk Metallic Glasses: At the Cutting Edge of Metals Research, MRS Bull. 32 (2007) 611-619.

[3] M.F. Ashby, A.L. Greer. Metallic glasses as structural materials, Scr. Mater. 54 (2006) 321-326.

[4] W.H. Wang. The elastic properties, elastic models and elastic perspectives of metallic glasses, Prog. Mater Sci. 57 (2012) 487-656.

[5] M. Chen. Mechanical behavior of metallic glasses: Microscopic understanding of strength and ductility, Annu. Rev. Mater. Res. 38 (2008) 445-469.

[6] A. Greer, E. Ma. Bulk metallic glasses: at the cutting edge of metals research, MRS Bull. 32 (2007) 611-619.

[7] H. Choi-Yim, W.L. Johnson. Bulk metallic glass matrix composites, Appl. Phys. Lett. 71 (1997) 3808-3810.

[8] J. Eckert, J. Das, S. Pauly, C. Duhamel. Mechanical properties of bulk metallic glasses and composites, J. Mater. Res. 22 (2007) 285-301.

[9] E. Hall. The deformation and ageing of mild steel: III discussion of results, Proceedings of the Physical Society. Section B 64 (1951) 747.

[10] N. Petch. The cleavage strength of polycrystals, J. Iron Steel Inst. 174 (1953) 25-28.

[11] A. Misra, J. Hirth, R. Hoagland. Length-scale-dependent deformation mechanisms in incoherent metallic multilayered composites, Acta Mater. 53 (2005) 4817-4824.

[12] X. Zhang, A. Misra, H. Wang, T.D. Shen, M. Nastasi, T.E. Mitchell, J.P. Hirth, R.G. Hoagland, J.D. Embury. Enhanced hardening in Cu/330 stainless steel multilayers by nanoscale twinning, Acta Mater. 52 (2004) 995-1002.

[13] Y. Liu, D. Bufford, H. Wang, C. Sun, X. Zhang. Mechanical properties of highly textured Cu/Ni multilayers, Acta Mater. 59 (2011) 1924-1933.

[14] E.G. Fu, N. Li, A. Misra, R.G. Hoagland, H. Wang, X. Zhang. Mechanical properties of sputtered Cu/V and Al/Nb multilayer films, Mater. Sci. Eng., A 493 (2008) 283-287.

[15] Y. Chen, Y. Liu, C. Sun, K. Yu, M. Song, H. Wang, X. Zhang. Microstructure and strengthening mechanisms in Cu/Fe multilayers, Acta Mater. 60 (2012) 6312-6321.

[16] J. Wang, A. Misra. An overview of interface-dominated deformation mechanisms in metallic multilayers, Curr. Opin. Solid State Mater. Sci. 15 (2011) 20-28.

[17] J. Wang, R.G. Hoagland, A. Misra. Mechanics of nanoscale metallic multilayers: From atomic-scale to micro-scale, Scr. Mater. 60 (2009) 1067-1072.

[18] J.Y. Zhang, S. Lei, Y. Liu, J.J. Niu, Y. Chen, G. Liu, X. Zhang, J. Sun. Length scale-dependent deformation behavior of nanolayered Cu/Zr micropillars, Acta Mater. 60 (2012) 1610-1622.

[19] X. Zhang, A. Misra, H. Wang, T. Shen, J. Swadener, J. Embury, H. Kung, R. Hoagland, M. Nastasi. Strengthening mechanisms in nanostructured copper/304 stainless steel multilayers, J. Mater. Res. 18 (2003) 1600-1606.

[20] N.A. Mara, T. Tamayo, A.V. Sergueeva, X. Zhang, A. Misra, A.K. Mukherjee. The effects of decreasing layer thickness on the high temperature mechanical behavior of Cu / Nb nanoscale multilayers, Thin Solid Films 515 (2007) 3241-3245.

[21] J. Wang, I.J. Beyerlein, N.A. Mara, D. Bhattacharyya. Interface-facilitated deformation twinning in copper within submicron Ag–Cu multilayered composites, Scr. Mater. 64 (2011) 1083-1086.

[22] J. Wang, K. Kang, R. Zhang, S. Zheng, I. Beyerlein, N. Mara. Structure and property of interfaces in ARB Cu/Nb laminated composites, JOM 64 (2012) 1208-1217.

[23] R. Hoagland, J. Hirth, A. Misra. On the role of weak interfaces in blocking slip in nanoscale layered composites, Philos. Mag. 86 (2006) 3537-3558.

[24] J. Koehler. Attempt to design a strong solid, Physical review B 2 (1970) 547.

[25] A. Misra, H. Krug. Deformation behavior of nanostructured metallic multilayers, Adv. Eng. Mater. 3 (2001) 217-222.

[26] A. Inoue, N. Nishiyama. New bulk metallic glasses for applications as magnetic-sensing, chemical, and structural materials, MRS Bull. 32 (2007) 651-658.

[27] H. Kakiuchi, A. Inoue, M. Onuki, Y. Takano, T. Yamaguchi. Bulk Metallic Glasses. III. Application of Zr-Based Bulk Glassy Alloys to Golf Clubs, Mater. Trans. 42 (2001) 678-681.

[28] J. Frenkel. The theory of the elastic limit and the solidity of crystal bodies, Z. Phys. 37 (1926) 572-609.

[29] S.S. Brenner. Tensile Strength of Whiskers, J. Appl. Phys. 27 (1956) 1484-1491.

[30] W. Johnson, K. Samwer. A universal criterion for plastic yielding of metallic glasses with a (T/T g) 2/3 temperature dependence, Phys. Rev. Lett. 95 (2005) 195501.

[31] A. Inoue. Stabilization of metallic supercooled liquid and bulk amorphous alloys, Acta Mater. 48 (2000) 279-306.

[32] H. Bei, Z. Lu, E. George. Theoretical strength and the onset of plasticity in bulk metallic glasses investigated by nanoindentation with a spherical indenter, Phys. Rev. Lett. 93 (2004) 125504.

[33] C. Packard, C. Schuh. Initiation of shear bands near a stress concentration in metallic glass, Acta Mater. 55 (2007) 5348-5358.

[34] C.A. Schuh, T.C. Hufnagel, U. Ramamurty. Mechanical behavior of amorphous alloys, Acta Mater. 55 (2007) 4067-4109.

[35] A. Argon. Plastic deformation in metallic glasses, Acta Metall. 27 (1979) 47-58.

[36] F. Spaepen. A microscopic mechanism for steady state inhomogeneous flow in metallic glasses, Acta Metall. 25 (1977) 407-415.

[37] A.L. Greer, Y.Q. Cheng, E. Ma. Shear bands in metallic glasses, Mater. Sci. Eng., R 74 (2013) 71-132.

[38] H. Leamy, T. Wang, H. Chen. Plastic flow and fracture of metallic glass, Metall. Trans. 3 (1972) 699-708.

[39] F. Spaepen, D. Turnbull. A mechanism for the flow and fracture of metallic glasses, Scr. Metall. 8 (1974) 563-568.

[40] D. Turnbull, M.H. Cohen. Free-volume model of the amorphous phase: glass transition, The Journal of chemical physics 34 (1961) 120-125.

[41] F. Spaepen. Homogeneous flow of metallic glasses: A free volume perspective, Scr. Mater. 54 (2006) 363-367.

[42] L. Li, E. Homer, C. Schuh. Shear transformation zone dynamics model for metallic glasses incorporating free volume as a state variable, Acta Mater. 61 (2013) 3347-3359.

[43] Z.F. Zhang, J. Eckert, L. Schultz. Difference in compressive and tensile fracture mechanisms of Zr59Cu20Al10Ni8Ti3 bulk metallic glass, Acta Mater. 51 (2003) 1167-1179.

[44] B.A. Sun, W.H. Wang. The fracture of bulk metallic glasses, Prog. Mater Sci. 74 (2015) 211-307.

[45] H. Sheng, W. Luo, F. Alamgir, J. Bai, E. Ma. Atomic packing and short-to-medium-range order in metallic glasses, Nature 439 (2006) 419-425.

[46] J. Schroers, W.L. Johnson. Ductile bulk metallic glass, Phys. Rev. Lett. 93 (2004) 255506.

[47] S. Madge, D. Louzguine-Luzgin, J. Lewandowski, A. Greer. Toughness, extrinsic effects and Poisson’s ratio of bulk metallic glasses, Acta Mater. 60 (2012) 4800-4809.

[48] J.P. Chu, J. Greene, J.S. Jang, J. Huang, Y.-L. Shen, P.K. Liaw, Y. Yokoyama, A. Inoue, T. Nieh. Bendable bulk metallic glass: Effects of a thin, adhesive, strong, and ductile coating, Acta Mater. 60 (2012) 3226-3238.

[49] R. Conner, W.L. Johnson, N. Paton, W. Nix. Shear bands and cracking of metallic glass plates in bending, J. Appl. Phys. 94 (2003) 904-911.

[50] A.H. Brothers, D.C. Dunand. Ductile bulk metallic glass foams, Adv. Mater. 17 (2005) 484-486.

[51] X.J. Gu, S.J. Poon, G.J. Shiflet, J.J. Lewandowski. Ductile-to-brittle transition in a Ti-based bulk metallic glass, Scr. Mater. 60 (2009) 1027-1030.

[52] Z.-D. Zhu, E. Ma, J. Xu. Elevating the fracture toughness of Cu49Hf42Al9 bulk metallic glass: Effects of cooling rate and frozen-in excess volume, Intermetallics 46 (2014) 164-172.

[53] P. Murali, U. Ramamurty. Embrittlement of a bulk metallic glass due to sub-Tg annealing, Acta Mater. 53 (2005) 1467-1478.

[54] M. Launey, R. Busch, J. Kruzic. Effects of free volume changes and residual stresses on the fatigue and fracture behavior of a Zr–Ti–Ni–Cu–Be bulk metallic glass, Acta Mater. 56 (2008) 500-510.

[55] K.B. Kim, J. Das, F. Baier, M.B. Tang, W.H. Wang, J. Eckert. Heterogeneity of a Cu47.5Zr47.5Al5 bulk metallic glass, Appl. Phys. Lett. 88 (2006) 051911.

[56] Y.H. Liu, G. Wang, R.J. Wang, M.X. Pan, W.H. Wang. Super plastic bulk metallic glasses at room temperature, Science 315 (2007) 1385-1388.

[57] C.T. Liu, M.F. Chisholm, M.K. Miller. Oxygen impurity and microalloying effect in a Zr-based bulk metallic glass alloy, Intermetallics 10 (2002) 1105-1112.

[58] Á. Révész, E. Schafler, Z. Kovács. Structural anisotropy in a Zr57Ti5Cu20Al10Ni8 bulk metallic glass deformed by high pressure torsion at room temperature, Appl. Phys. Lett. 92 (2008) 011910.

[59] J. Sort, D.C. Ile, A.P. Zhilyaev, A. Concustell, T. Czeppe, M. Stoica, S. Suriñach, J. Eckert, M.D. Baró. Cold-consolidation of ball-milled Fe-based amorphous ribbons by high pressure torsion, Scr. Mater. 50 (2004) 1221-1225.

[60] C. Volkert, A. Donohue, F. Spaepen. Effect of sample size on deformation in amorphous metals, J. Appl. Phys. 103 (2008) 83539-83539.

[61] D. Jang, J.R. Greer. Transition from a strong-yet-brittle to a stronger-and-ductile state by size reduction of metallic glasses, Nat. Mater. 9 (2010) 215-219.

[62] D.C. Hofmann, J.-Y. Suh, A. Wiest, G. Duan, M.-L. Lind, M.D. Demetriou, W.L. Johnson. Designing metallic glass matrix composites with high toughness and tensile ductility, Nature 451 (2008) 1085-1089.

[63] O. Biletska, K.J. Laws, M.A. Gibson, M. Ferry. Fabrication of an In Situ Bulk Metallic Glass Composite with High Magnesium Content, Metall. Mater. Trans. A 45 (2014) 2352-2356.

[64] G. Chen, J. Cheng, C.T. Liu. Large-sized Zr-based bulk-metallic-glass composite with enhanced tensile properties, Intermetallics 28 (2012) 25-33.

[65] Y. Wu, D. Zhou, W. Song, H. Wang, Z. Zhang, D. Ma, X. Wang, Z. Lu. Ductilizing bulk metallic glass composite by tailoring stacking fault energy, Phys. Rev. Lett. 109 (2012) 245506.

[66] F. Wu, K. Chan, S. Li, G. Wang, P. Lin. Tensile deformation of a Ti-based metallic glass composite lamella confined by commercially pure titanium, Philos. Mag. Lett. 94 (2014) 233-241.

[67] C. Fan, R. Ott, T. Hufnagel. Metallic glass matrix composite with precipitated ductile reinforcement, Appl. Phys. Lett. 81 (2002) 1020-1022.

[68] H. Guo, P. Yan, Y. Wang, J. Tan, Z. Zhang, M. Sui, E. Ma. Tensile ductility and necking of metallic glass, Nat. Mater. 6 (2007) 735-739.

[69] H. Bei, S. Xie, E.P. George. Softening caused by profuse shear banding in a bulk metallic glass, Phys. Rev. Lett. 96 (2006) 105503.

[70] X.K. Xi, D.Q. Zhao, M.X. Pan, W.H. Wang, Y. Wu, J.J. Lewandowski. Fracture of Brittle Metallic Glasses: Brittleness or Plasticity, Phys. Rev. Lett. 94 (2005) 125510.

[71] D.E. Polk, D. Turnbull. Flow of melt and glass forms of metallic alloys, Acta Metall. 20 (1972) 493-498.

[72] W. Klement, R.H. Willens, P.O.L. Duwez. Non-crystalline Structure in Solidified Gold-Silicon Alloys, Nature 187 (1960) 869-870.

[73] A. Takeuchi, A. Inoue. Classification of bulk metallic glasses by atomic size difference, heat of mixing and period of constituent elements and its application to characterization of the main alloying element, Mater. Trans. 46 (2005) 2817-2829.

[74] I. Knorr, N. Cordero, E.T. Lilleodden, C.A. Volkert. Mechanical behavior of nanoscale Cu/PdSi multilayers, Acta Mater. 61 (2013) 4984-4995.

[75] J. Zhang, Y. Liu, J. Chen, Y. Chen, G. Liu, X. Zhang, J. Sun. Mechanical properties of crystalline Cu/Zr and crystal–amorphous Cu/Cu–Zr multilayers, Mater. Sci. Eng., A 552 (2012) 392-398.

[76] H. Huang, H. Pei, Y. Chang, C. Lee, J. Huang. Tensile behaviors of amorphous-ZrCu/nanocrystalline-Cu multilayered thin film on polyimide substrate, Thin Solid Films 529 (2013) 177-180.

[77] J.P. Chu, J. Jang, J. Huang, H. Chou, Y. Yang, J. Ye, Y. Wang, J. Lee, F. Liu, P. Liaw. Thin film metallic glasses: Unique properties and potential applications, Thin Solid Films 520 (2012) 5097-5122.

[78] X. Zhou, C. Chen. Molecular dynamic simulations of the mechanical properties of crystalline/crystalline and crystalline/amorphous nanolayered pillars, Computational Materials Science 101 (2015) 194-200.

[79] M. Liu, J. Huang, Y. Fong, S. Ju, X. Du, H. Pei, T. Nieh. Assessing the interfacial strength of an amorphous–crystalline interface, Acta Mater. 61 (2013) 3304-3313.

[80] J. Chu, J. Huang, J. Jang, Y. Wang, P. Liaw. Thin film metallic glasses: preparations, properties, and applications, JOM 62 (2010) 19-24.

[81] L. Huang, J. Zhou, S. Zhang, Y. Wang, Y. Liu. Effects of interface and microstructure on the mechanical behaviors of crystalline Cu-amorphous Cu/Zr nanolaminates, Mater. Des. 36 (2012) 6-12.

[82] A. Alpas, J. Embury. Flow localization in thin layers of amorphous alloys in laminated composite structures, Scr. Metall. 22 (1988) 265-270.

[83] M.C. Liu, C.J. Lee, Y.H. Lai, J.C. Huang. Microscale deformation behavior of amorphous/nanocrystalline multilayered pillars, Thin Solid Films 518 (2010) 7295-7299.

[84] T. Nieh, J. Wadsworth. Bypassing shear band nucleation and ductilization of an amorphous–crystalline nanolaminate in tension, Intermetallics 16 (2008) 1156-1159.

[85] Y.M. Wang, A.V. Hamza, T.W. Barbee. Incipient plasticity in metallic glass modulated nanolaminates, Appl. Phys. Lett. 91 (2007) 061924.

[86] Y. Wang, J. Li, A.V. Hamza, T.W. Barbee. Ductile crystalline–amorphous nanolaminates, Proc. Natl. Acad. Sci. 104 (2007) 11155-11160.

[87] M. Liu, X. Du, I. Lin, H. Pei, J. Huang. Superplastic-like deformation in metallic amorphous/crystalline nanolayered micropillars, Intermetallics 30 (2012) 30-34.

[88] J. Zhang, G. Liu, S. Lei, J. Niu, J. Sun. Transition from homogeneous-like to shear-band deformation in nanolayered crystalline Cu/amorphous Cu–Zr micropillars: Intrinsic vs. extrinsic size effect, Acta Mater. 60 (2012) 7183-7196.

[89] W. Guo, E.A. Jägle, P.-P. Choi, J. Yao, A. Kostka, J.M. Schneider, D. Raabe. Shear-induced mixing governs codeformation of crystalline-amorphous nanolaminates, Phys. Rev. Lett. 113 (2014) 035501.

[90] D. Jang, C.T. Gross, J.R. Greer. Effects of size on the strength and deformation mechanism in Zr-based metallic glasses, Int. J. Plast. 27 (2011) 858-867.

[91] J.Y. Kim, D. Jang, J.R. Greer. Nanolaminates Utilizing Size-Dependent Homogeneous Plasticity of Metallic Glasses, Adv. Funct. Mater. 21 (2011) 4550-4554.

[92] W. Guo, E. Jägle, J. Yao, V. Maier, S. Korte-Kerzel, J.M. Schneider, D. Raabe. Intrinsic and extrinsic size effects in the deformation of amorphous CuZr/nanocrystalline Cu nanolaminates, Acta Mater. 80 (2014) 94-106.

[93] A. Donohue, F. Spaepen, R. Hoagland, A. Misra. Suppression of the shear band instability during plastic flow of nanometer-scale confined metallic glasses, Appl. Phys. Lett. 91 (2007) 241905.

[94] J. Cahn, F. Nabarro. Thermal activation under shear, Philos. Mag. A 81 (2001) 1409-1426.

[95] Q. Wei. Strain rate effects in the ultrafine grain and nanocrystalline regimes—influence on some constitutive responses, J. Mater. Sci. 42 (2007) 1709-1727.

[96] Q. Wei, S. Cheng, K. Ramesh, E. Ma. Effect of nanocrystalline and ultrafine grain sizes on the strain rate sensitivity and activation volume: fcc versus bcc metals, Mater. Sci. Eng., A 381 (2004) 71-79.

[97] C. Schuh, T. Nieh, Y. Kawamura. Rate dependence of serrated flow during nanoindentation of a bulk metallic glass, J. Mater. Res. 17 (2002) 1651-1654.

[98] W. Jiang, M. Atzmon. Rate dependence of serrated flow in a metallic glass, J. Mater. Res. 18 (2003) 755-757.

[99] W. Jiang, G. Fan, F. Liu, G. Wang, H. Choo, P. Liaw. Rate dependence of shear banding and serrated flows in a bulk metallic glass, J. Mater. Res. 21 (2006) 2164-2167.

[100] C. Schuh, T. Nieh. A survey of instrumented indentation studies on metallic glasses, J. Mater. Res. 19 (2004) 46-57.

[101] J. Zhang, J.M. Park, D.H. Kim, H.S. Kim. Effect of strain rate on compressive behavior of Ti45Zr16Ni9Cu10Be20 bulk metallic glass, Mater. Sci. Eng., A 449–451 (2007) 290-294.

[102] R. Limbach, B.P. Rodrigues, L. Wondraczek. Strain-rate sensitivity of glasses, J. Non-Cryst. Solids 404 (2014) 124-134.

[103] W. Ma, H. Kou, J. Li, H. Chang, L. Zhou. Effect of strain rate on compressive behavior of Ti-based bulk metallic glass at room temperature, J. Alloys Compd. 472 (2009) 214-218.

[104] Y.F. Xue, H.N. Cai, L. Wang, F.C. Wang, H.F. Zhang. Effect of loading rate on failure in Zr-based bulk metallic glass, Mater. Sci. Eng., A 473 (2008) 105-110.

[105] F.H. Dalla Torre, A. Dubach, M.E. Siegrist, J.F. Löffler. Negative strain rate sensitivity in bulk metallic glass and its similarities with the dynamic strain aging effect during deformation, Appl. Phys. Lett. 89 (2006) 091918.

[106] Y. Wang, J. Zhang, X. Liang, K. Wu, G. Liu, J. Sun. Size-and constituent-dependent deformation mechanisms and strain rate sensitivity in nanolaminated crystalline Cu/amorphous Cu–Zr films, Acta Mater. 95 (2015) 132-144.

[107] M. Chen, A. Inoue, W. Zhang, T. Sakurai. Extraordinary Plasticity of Ductile Bulk Metallic Glasses, Phys. Rev. Lett. 96 (2006) 245502.

[108] D. Rigney. Sliding wear of metals, Annu. Rev. Mater. Sci. 18 (1988) 141-163.

[109] J. Archard. Contact and rubbing of flat surfaces, J. Appl. Phys. 24 (1953) 981-988.

[110] I. Finch. The Beilby layer on non-metals, Nature 138 (1936) 1010.

[111] A. Greer, K. Rutherford, I. Hutchings. Wear resistance of amorphous alloys and related materials, Int. Mater. Rev. 47 (2002) 87-112.

[112] G. Zhang, X. Li, M. Shao, L. Wang, J. Yang, L. Gao, L. Chen, C. Liu. Wear behavior of a series of Zr-based bulk metallic glasses, Mater. Sci. Eng., A 475 (2008) 124-127.

[113] J. Bhatt, S. Kumar, C. Dong, B. Murty. Tribological behaviour of Cu 60 Zr 30 Ti 10 bulk metallic glass, Mater. Sci. Eng., A 458 (2007) 290-294.

[114] A. Alpas, J. Embury. The role of subsurface deformation and strain localization on the sliding wear behaviour of laminated composites, Wear 146 (1991) 285-300.

[115] W.C. Oliver, G.M. Pharr. An improved technique for determining hardness and elastic modulus using load and displacement sensing indentation experiments, J. Mater. Res. 7 (1992) 1564-1583.

[116] W.C. Oliver, G.M. Pharr. Measurement of hardness and elastic modulus by instrumented indentation: Advances in understanding and refinements to methodology, J. Mater. Res. 19 (2004) 3-20.

[117] B.-G. Yoo, J.-Y. Kim, Y.-J. Kim, I.-C. Choi, S. Shim, T.Y. Tsui, H. Bei, U. Ramamurty, J.-i. Jang. Increased time-dependent room temperature plasticity in metallic glass nanopillars and its size-dependency, Int. J. Plast. 37 (2012) 108-118.

[118] F.F. Wu, W. Zheng, S.D. Wu, Z.F. Zhang, J. Shen. Shear stability of metallic glasses, Int. J. Plast. 27 (2011) 560-575.

[119] Y. Chen, M.Q. Jiang, L.H. Dai. Collective evolution dynamics of multiple shear bands in bulk metallic glasses, Int. J. Plast. 50 (2013) 18-36.

[120] H. Zhou, S. Qu, W. Yang. An atomistic investigation of structural evolution in metallic glass matrix composites, Int. J. Plast. 44 (2013) 147-160.

[121] P. Zhao, J. Li, Y. Wang. Heterogeneously randomized STZ model of metallic glasses: Softening and extreme value statistics during deformation, Int. J. Plast. 40 (2013) 1-22.

[122] Y. Liu, Y. Chen, K. Yu, H. Wang, J. Chen, X. Zhang. Stacking fault and partial dislocation dominated strengthening mechanisms in highly textured Cu/Co multilayers, Int. J. Plast. 49 (2013) 152-163.

[123] Y. Zhu, Z. Li, M. Huang, Y. Liu. Strengthening mechanisms of the nanolayered polycrystalline metallic multilayers assisted by twins, Int. J. Plast. 72 (2015) 168-184.

[124] H. Pei, S. Kuan, M. Liu, J. Huang. Tensile behavior of amorphous/nanocrystalline ZrCu/Cu multilayered films with graded interfaces, Intermetallics 31 (2012) 191-195.

[125] E.G. Fu, A. Misra, H. Wang, L. Shao, X. Zhang. Interface enabled defects reduction in helium ion irradiated Cu/V nanolayers, J. Nucl. Mater. 407 (2010) 178-188.

[126] R. Saha, W.D. Nix. Effects of the substrate on the determination of thin film mechanical properties by nanoindentation, Acta Mater. 50 (2002) 23-38.

[127] D. Raabe, S. Ohsaki, K. Hono. Mechanical alloying and amorphization in Cu–Nb–Ag in situ composite wires studied by transmission electron microscopy and atom probe tomography, Acta Mater. 57 (2009) 5254-5263.

[128] K. Yu, Y. Liu, S. Rios, H. Wang, X. Zhang. Strengthening mechanisms of Ag/Ni immiscible multilayers with fcc/fcc interface, Surf. Coat. Technol. 237 (2013) 269-275.

[129] N. Li, E.G. Fu, H. Wang, J.J. Carter, L. Shao, S.A. Maloy, A. Misra, X. Zhang. He ion irradiation damage in Fe/W nanolayer films, J. Nucl. Mater. 389 (2009) 233-238.

[130] W.D. Nix. Yielding and strain hardening of thin metal films on substrates, Scr. Mater. 39 (1998) 545-554.

[131] D. Wang, Y. Li, B.B. Sun, M.L. Sui, K. Lu, E. Ma. Bulk metallic glass formation in the binary Cu–Zr system, Appl. Phys. Lett. 84 (2004) 4029-4031.

[132] M.-B. Tang, D.-Q. Zhao, M.-X. Pan, W.-H. Wang. Binary Cu–Zr Bulk Metallic Glasses, Chinese Physics Letters 21 (2004) 901.

[133] D. Raabe, U. Hangen. Investigation of structurally less-ordered areas in the Nb filaments of a heavily cold-rolled Cu-20 wt.% Nb in situ composite, J. Mater. Res. 10 (1995) 3050-3061.

[134] D. Raabe, U. Hangen. Observation of amorphous areas in a heavily cold rolled Cu-20 wt% Nb composite, Mater. Lett. 22 (1995) 155-161.

[135] C. Schuh, A. Argon, T. Nieh, J. Wadsworth. The transition from localized to homogeneous plasticity during nanoindentation of an amorphous metal, Philos. Mag. 83 (2003) 2585-2597.

[136] J. Wang, R. Hoagland, J. Hirth, A. Misra. Atomistic modeling of the interaction of glide dislocations with “weak” interfaces, Acta Mater. 56 (2008) 5685-5693.

[137] J. Wang, R. Hoagland, J. Hirth, A. Misra. Atomistic simulations of the shear strength and sliding mechanisms of copper–niobium interfaces, Acta Mater. 56 (2008) 3109-3119.

[138] J. Wang, R. Hoagland, X. Liu, A. Misra. The influence of interface shear strength on the glide dislocation–interface interactions, Acta Mater. 59 (2011) 3164-3173.

[139] N. Jia, F. Roters, P. Eisenlohr, D. Raabe, X. Zhao. Simulation of shear banding in heterophase co-deformation: Example of plane strain compressed Cu–Ag and Cu–Nb metal matrix composites, Acta Mater. 61 (2013) 4591-4606.

[140] M.L. Lee, Y. Li, C.A. Schuh. Effect of a controlled volume fraction of dendritic phases on tensile and compressive ductility in La-based metallic glass matrix composites, Acta Mater. 52 (2004) 4121-4131.

[141] G. He, W. Löser, J. Eckert, L. Schultz. Enhanced plasticity in a Ti-based bulk metallic glass-forming alloy by in situ formation of a composite microstructure, J. Mater. Res. 17 (2002) 3015-3018.

[142] J. Wang, Q. Zhou, S. Shao, A. Misra. Strength and plasticity of nanolaminated materials, Mater. Res. Lett. 5 (2017) 1-19.

[143] M. Liu, J. Huang, H. Chou, Y. Lai, C. Lee, T. Nieh. A nanoscaled underlayer confinement approach for achieving extraordinarily plastic amorphous thin film, Scr. Mater. 61 (2009) 840-843.

[144] J. Ye, J. Lu, Y. Yang, P. Liaw. Extraction of bulk metallic-glass yield strengths using tapered micropillars in micro-compression experiments, Intermetallics 18 (2010) 385-393.

[145] A. Bharathula, S.-W. Lee, W.J. Wright, K.M. Flores. Compression testing of metallic glass at small length scales: Effects on deformation mode and stability, Acta Mater. 58 (2010) 5789-5796.

[146] R. Narasimhan, P. Tandaiya, I. Singh, R. Narayan, U. Ramamurty. Fracture in metallic glasses: mechanics and mechanisms, Int. J. Fract. 191 (2015) 53-75.

[147] D. Matthews, V. Ocelik, P. Bronsveld, J.T.M. De Hosson. An electron microscopy appraisal of tensile fracture in metallic glasses, Acta Mater. 56 (2008) 1762-1773.

[148] C. Gilbert, V. Schroeder, R. Ritchie. Mechanisms for fracture and fatigue-crack propagation in a bulk metallic glass, Metall. Mater. Trans. A 30 (1999) 1739-1753.

[149] F. Spaepen. On the fracture morphology of metallic glasses, Acta Metall. 23 (1975) 615-620.

[150] J. Xu, U. Ramamurty, E. Ma. The fracture toughness of bulk metallic glasses, JOM 62 (2010) 10-18.

[151] J. Lewandowski*, W. Wang, A. Greer. Intrinsic plasticity or brittleness of metallic glasses, Philos. Mag. Lett. 85 (2005) 77-87.

[152] S. Wagner, S.P. Lacour, J. Jones, I.H. Pai-hui, J.C. Sturm, T. Li, Z. Suo. Electronic skin: architecture and components, Physica E: Low Dimens Syst Nanostruct 25 (2004) 326-334.

[153] J.A. Rogers, Z. Bao, K. Baldwin, A. Dodabalapur, B. Crone, V. Raju, V. Kuck, H. Katz, K. Amundson, J. Ewing. Paper-like electronic displays: Large-area rubber-stamped plastic sheets of electronics and microencapsulated electrophoretic inks, Proc. Natl. Acad. Sci. 98 (2001) 4835-4840.

[154] G. Zhang, Y. Liu, B. Zhang. Effect of annealing close to T g on notch fracture toughness of Pd-based thin-film metallic glass for MEMS applications, Scr. Mater. 54 (2006) 897-901.

[155] N. Kaushik, P. Sharma, S. Ahadian, A. Khademhosseini, M. Takahashi, A. Makino, S. Tanaka, M. Esashi. Metallic glass thin films for potential biomedical applications, J. Biomed. Mater. Res., Part B 102 (2014) 1544-1552.

[156] F. Macionczyk, W. Brückner. Tensile testing of AlCu thin films on polyimide foils, J. Appl. Phys. 86 (1999) 4922-4929.

[157] Y. Denis, F. Spaepen. The yield strength of thin copper films on Kapton, J. Appl. Phys. 95 (2004) 2991-2997.

[158] C.A. Pampillo. Flow and fracture in amorphous alloys, J. Mater. Sci. 10 (1975) 1194-1227.

[159] G. Wang, D. Zhao, H. Bai, M. Pan, A. Xia, B. Han, X. Xi, Y. Wu, W. Wang. Nanoscale periodic morphologies on the fracture surface of brittle metallic glasses, Phys. Rev. Lett. 98 (2007) 235501.

[160] Z. Fan, S. Xue, J. Wang, K.Y. Yu, H. Wang, X. Zhang. Unusual size dependent strengthening mechanisms of Cu/amorphous CuNb multilayers, Acta Mater. 120 (2016) 327-336.

[161] W.D. Nix, H. Gao. Indentation size effects in crystalline materials: a law for strain gradient plasticity, J. Mech. Phys. Solids 46 (1998) 411-425.

[162] C. Brandl, T. Germann, A. Misra. Structure and shear deformation of metallic crystalline–amorphous interfaces, Acta Mater. 61 (2013) 3600-3611.

[163] L. Tian, Z.-W. Shan, E. Ma. Ductile necking behavior of nanoscale metallic glasses under uniaxial tension at room temperature, Acta Mater. 61 (2013) 4823-4830.

[164] J.Y. Zhang, Y. Liu, J. Chen, Y. Chen, G. Liu, X. Zhang, J. Sun. Mechanical properties of crystalline Cu/Zr and crystal–amorphous Cu/Cu–Zr multilayers, Mater. Sci. Eng., A 552 (2012) 392-398.

[165] R. Schwaiger, B. Moser, M. Dao, N. Chollacoop, S. Suresh. Some critical experiments on the strain-rate sensitivity of nanocrystalline nickel, Acta materialia 51 (2003) 5159-5172.

[166] J. Chen, L. Lu, K. Lu. Hardness and strain rate sensitivity of nanocrystalline Cu, Scr. Mater. 54 (2006) 1913-1918.

[167] Y. Shen, L. Lu, M. Dao, S. Suresh. Strain rate sensitivity of Cu with nanoscale twins, Scr. Mater. 55 (2006) 319-322.

[168] T. Nieh, C. Schuh, J. Wadsworth, Y. Li. Strain rate-dependent deformation in bulk metallic glasses, Intermetallics 10 (2002) 1177-1182.

[169] Y. Liu, J. Hay, H. Wang, X. Zhang. A new method for reliable determination of strain-rate sensitivity of low-dimensional metallic materials by using nanoindentation, Scr. Mater. 77 (2014) 5-8.

[170] G. Pharr, W. Oliver, F. Brotzen. On the generality of the relationship among contact stiffness, contact area, and elastic modulus during indentation, J. Mater. Res. 7 (1992) 613-617.

[171] I.N. Sneddon. The relation between load and penetration in the axisymmetric Boussinesq problem for a punch of arbitrary profile, Int. J. Eng. Sci. 3 (1965) 47-57.

[172] T. Page, G. Pharr, J. Hay, W. Oliver, B. Lucas, E. Herbert, L. Riester. Nanoindentation Characterisation of Coated Systems: P: S 2-A New Approach Using the Continuous Stiffness Technique. MRS Proceedings, vol. 522: Cambridge Univ Press, 1998. p.53.

[173] D. Joslin, W. Oliver. A new method for analyzing data from continuous depth-sensing microindentation tests, J. Mater. Res. 5 (1990) 123-126.

[174] J. Lian, C. Gu, Q. Jiang, Z. Jiang. Strain rate sensitivity of face-centered-cubic nanocrystalline materials based on dislocation deformation, J. Appl. Phys. 99 (2006) 076103.

[175] M. Ishida, H. Takeda, D. Watanabe, K. Amiya, N. Nishiyama, K. Kita, Y. Saotome, A. Inoue. Fillability and imprintability of high-strength Ni-based bulk metallic glass prepared by the precision die-casting technique, Mater. Trans. 45 (2004) 1239-1244.

[176] M. Ishida, H. Takeda, N. Nishiyama, K. Kita, Y. Shimizu, Y. Saotome, A. Inoue. Wear resistivity of super-precision microgear made of Ni-based metallic glass, Mater. Sci. Eng., A 449 (2007) 149-154.

[177] P.H. Tsai, Y.Z. Lin, J.B. Li, S.R. Jian, J.S.C. Jang, C. Li, J.P. Chu, J.C. Huang. Sharpness improvement of surgical blade by means of ZrCuAlAgSi metallic glass and metallic glass thin film coating, Intermetallics 31 (2012) 127-131.

[178] P.-T. Chiang, G.-J. Chen, S.-R. Jian, Y.-H. Shih, J.S.-C. Jang, C.-H. Lai. Surface antimicrobial effects of Zr 61 Al 7.5 Ni 10 Cu 17.5 Si 4 thin film metallic glasses on escherichia coli, staphylococcus aureus, pseudomonas aeruginosa, acinetobacter baumannii and candida albicans, Fooyin Journal of Health Sciences 2 (2010) 12-20.

[179] Y. Huang, Y.L. Chiu, J. Shen, Y. Sun, J.J. Chen. Mechanical performance of metallic glasses during nanoscratch tests, Intermetallics 18 (2010) 1056-1061.

[180] A. Leyland, A. Matthews. On the significance of the H/E ratio in wear control: a nanocomposite coating approach to optimised tribological behaviour, Wear 246 (2000) 1-11.

[181] A. Hodge, T. Nieh. Evaluating abrasive wear of amorphous alloys using nanoscratch technique, Intermetallics 12 (2004) 741-748.

[182] S. Yoon, J. Kim, B.D. Kim, C. Lee. Tribological behavior of B 4 C reinforced Fe-base bulk metallic glass composite coating, Surf. Coat. Technol. 205 (2010) 1962-1968.

[183] T. Gloriant. Microhardness and abrasive wear resistance of metallic glasses and nanostructured composite materials, J. Non-Cryst. Solids 316 (2003) 96-103.

[184] J. Wang, B. Choi, T. Nieh, C. Liu. Nano-scratch behavior of a bulk Zr–10Al–5Ti–17.9 Cu–14.6 Ni amorphous alloy, J. Mater. Res. 15 (2000) 913-922.

[185] T. Gloriant, A. Greer. Al-based nanocrystalline composites by rapid solidification of Al-Ni-Sm alloys, Nanostruct. Mater. 10 (1998) 389-396.

[186] B.-T. Jang, S.-H. Yi, S.-S. Kim. Tribological behavior of Fe-based bulk metallic glass, Journal of Mechanical Science and Technology 24 (2010) 89-92.

[187] U. Sudarsan, N. Chandran, K. Chattopadhyay. On the wear mechanism of iron and nickel based transition metal-metalloid metallic glasses, Acta Metall. 35 (1987) 1463-1473.

[188] S. Wen, R. Zong, F. Zeng, Y. Gao, F. Pan. Investigation of the wear behaviors of Ag/Cu multilayers by nanoscratch, Wear 265 (2008) 1808-1813.

[189] S. Wen, R. Zong, F. Zeng, S. Guo, F. Pan. Nanoindentation and nanoscratch behaviors of Ag/Ni multilayers, Appl. Surf. Sci. 255 (2009) 4558-4562.

[190] A. Haseeb, J.-P. Celis, J. Roos. Fretting wear of metallic multilayer films, Thin Solid Films 444 (2003) 199-207.

[191] B. Bhushan, B. Gupta, M.H. Azarian. Nanoindentation, microscratch, friction and wear studies of coatings for contact recording applications, Wear 181 (1995) 743-758.

[192] B. Gupta, B. Bhushan. Mechanical and tribological properties of hard carbon coatings for magnetic recording heads, Wear 190 (1995) 110-122.

[193] A. Rosenfield. A shear instability model of sliding wear, Wear 116 (1987) 319-328.